Fakultät für Elektrotechnik und Informationstechnik

Lehrstuhl für Messsystem- und Sensortechnik

Dual Transverse Electro-Optic Modulator in Optical Interferometric Systems

Shengjia Wang

Vollständiger Abdruck der von der Fakultät für
Elektrotechnik und Informationstechnik
der Technischen Universität München
zur Erlangung des akademischen Grades eines

Doktor-Ingenieurs

genehmigten Dissertation.

Vorsitzender: Prof. Dr.-Ing. Andreas Jossen
Prüfer der Dissertation: 1. Prof. Dr.-Ing. habil. Dr. h.c. Alexander W. Koch
2. Prof. Félix José Salazar Bloise, Ph.D.

Abstract

Optical interferometric systems are commonly used tools for the investigation of optical waves. It gives the possibility of detecting optical waves in an indirect scheme, because no counter is available to directly register the fast oscillations in the level of optical frequencies. Phase-shifting technique further renders the optical interferometric system quantitative, in which the phase of the optical wave is detected precisely. A reliable and proper phase modulator is more than a guarantee for a successful investigation, but also determines the features of the system. The motivation of the present study is the demand in a versatile phase modulator which is compatible with distinct optical interferometric systems.

A novel phase modulator is thus proposed, which is based on the dual transverse electro-optic effect. A revised electro-optic coefficient is taken into consideration to run the proposed phase modulator within the frame rate of most commercial array detectors. Two sinusoidal electric fields are applied to the electro-optic crystal in orthogonal directions with a phase delay of $\pi/2$. The proposed phase modulator has the following features: 1) simultaneous and local modulation for both interfering waves; 2) installation in the main path prior to the beam split; 3) linearly time-varying phase shift; 4) easy operation; and 5) no mechanical motion unit. Thanks to these inherent features, the proposed phase modulator is capable of being applied in diverse interferometric systems.

The feasibility and functionality of the proposed phase modulator are demonstrated by an implementation which is based on a Michelson interferometer. A sinusoidal variation in the interference intensity is observed, which gives the proof of the linearly time-varying phase shift. In terms of its compatibility, the proposed phase modulator is coupled into three typical representatives of interferometric systems, respectively, namely an interferometer, a holography system, and a differential microscope. Firstly, in the temporal electronic speckle pattern interferometry (ESPI) system, the proposed phase modulator provides the temporal frequency carrier, from which the in-plane rotation is evaluated. Real-time measurements for dynamic targets are achieved, which reflects the superiority of the proposed phase modulator. Secondly, in the phase-shifting in-line holography

system, the proposed phase modulator is used for the retrieval of the optical field at the hologram plane. The retrieved field is free of the twin image and the non-diffraction component. Lensless imaging is accomplished by the back propagation of the retrieved optical field. Thirdly, a Nomarski differential interference contrast (DIC) microscope is proposed, which is based on the phase modulator. Quantitative phase contrast imaging is realized by a novel phase shift scheme which is termed as joint spatio-temporal phase modulation. The joint modulation is provided by the proposed phase modulator and the differential prism. Transparent samples, e.g., a single-mode fiber and the forewing of a honey bee, are quantitatively visualized without dyeing.

The physical principle, mathematical derivation, and experimental verification are demonstrated in detail. Regarding the further developments of the proposed phase modulator, much work and study remain to be done. Among others, two potential aspects are discussed, namely the high frequency applications and the cascade usage of multiple modulators in a single system.

Contents

Chapter 1

Introduction

Phase, according to its etymology, originates from the Greek word *phasis*. The stem *pha-* means "to shine", which gives an interpretation of phase as "appearance" [1]. Historically, phase was used to refer, in particular, to the lunar phase or phase of the moon [2]. Nowadays, the physical society has developed the term phase into two abstract meanings. One represents a property of waves, which indicates the absolute/relative position of a point on a waveform cycle in space-time [3]. Considering the waves with an identical frequency, they are said to be in phase if they have the same phase, whereas to be out of phase otherwise. The term phase is also used to describe the states of matter. The four classic phases of matter are solid, liquid, gaseous, and plasma phases. When a phase of matter alters into another, the matter is said to undergo a phase change or a phase transition [4]. In this thesis, the term phase is restricted to the property of electromagnetic (EM) waves unless otherwise indicated.

EM radiations exhibit a transverse wave feature, which indicates the oscillations of the electric and the magnetic fields are perpendicular to the direction of the wave propagation. In vacuum, despite of their distinct frequencies or wavelengths, all EM waves travel at the speed of light with an approximation of 3×10^8 m/s. The wavelength, speed, and frequency of EM waves are related to one another [5], denoted by

$$\lambda = c/f, \tag{1.1}$$

where λ, c, and f represent the wavelength, the speed of light, and the frequency, respectively. In the order of descending wavelength, the EM spectrum consists of radio waves, microwaves, infrared, visible light, ultraviolet, X-rays, and gamma rays. The behavior of an EM wave depends on its frequency and further determines its usage and application. For example, visible light, the most familiar group of the EM spectrum, is used for pho-

tography and illumination, because such a portion of spectrum is visible to human eyes and shows colors as well.

In the field of optics, the portion of the EM spectrum that is of interest is commonly termed as light, which includes infrared, visible, and ultraviolet lights. However, optics was recognized as an individual discipline for a long time until Maxwell concluded from his crowned equations that light itself is also an EM wave [6]. Since light joined the EM spectrum family, most optical phenomena can be described by the EM laws, which promotes the development of optical science and technology. In return, the electromagnetism also benefits from the convenience in the observation of optical phenomena. The applications of optics in the written history dates back to the ancient Greece, when Thales (640 - 546 B.C.) estimated the height of the Pyramid by its shadow under sunlight [7]. Not surprisingly, the evolution of light sources accelerates the study of optical science and broadens its applications as well. Throughout the history of science, the knowledge of optics always finds a tremendous growth when there is a fundamental upgrade of the light source. For example, in ancient times, the study of optics was based on the observation of natural phenomena from sunlight. Geometrical optics, which mainly deals with reflections and refractions, was developed under the help of candles [8]. Physical optics had to wait until the gas-discharge lamps [9] came into being, which provides a passable monochromatic light for a successful study of interference, diffraction, and polarization. Modern optics was fully brought onto the stage only when continuous-wave (CW) lasers [10] first became commercially available.

Following the aforementioned evolution history, it is quite fair to say the enhancements of light sources take place normally in two aspects. One is the power density of the output radiation, which is expressed as intensity in the detection. The other is the EM spectrum bandwidth of the output power density, which is termed as monochromaticity. Generally speaking, the increasing intensity is driven by the study of light-matter interaction, while the improving monochromaticity is motived by the demand of a higher accuracy in the field of optical metrology. As of this writing, the stabilized laser at sub-hertz level of linewidth has been reported [11], and the commercial products stabilized at kilohertz level have been widely available with a selection of output intensities.

Under such circumstances, the present study goes into a detailed branch of optical metrology, in which wavelength is taken as a measure. The methodology for quantitatively investigating the light waves involves the coherent superposition of two waves and the phase modulation between them. The focus of this thesis lies on a newly developed phase modulator, which is based on the dual transverse electro-optic (DTEO) effect. Most optics-related theories and discussions in this thesis are based on physical optics without entering the complicated quantum optics, which is to say the light is treated as wave.

1.1 Scientific Problem Statements

Before long, since the birth of laser in the early 1960s, the study of optical metrology was brought into a new era. Indeed, before laser was invented, quite a lot of studies had touched a few fundamental nature of light, such as Thomas Young's double slit interferometer in 1803 [12, 13]. The underlying potential of laser, compared with other light sources by then, provides an illumination with excellent monochromaticity and coherence. Aside from the promotion in the study of light itself, such a superior illumination enables an application of light, in which the wavelength/frequency of the quasi-monochromatic light is taken as a measure in the field of metrology. The accuracy and reliability of measurements in the generalized background is greatly improved, because the measure itself, namely the wavelength, is determined by the stimulated emission. For one thing, the wavelength is precise enough to improve the accuracy to the micron-nanometer level. For another, the monochromaticity and the stability of the wavelength are guaranteed by the stimulated emission. However, a wavelength of a micron-nanometer order brings around difficulties to the direct detection of the light wave. As a matter of fact, the optical frequencies are in an order of hundreds of terahertz (terahertz=10^{12} Hz), resulting in a reality that no counter is available to register so fast oscillations.

Fortunately, the behavior of waves is different from that of solid bodies. Two waves can go through each other, which means they can be in the same place at the same time. This gives a potential to investigate the optical frequencies indirectly. By superposing two waves, it is relatively easy to inquire the difference between them. In the case of two close frequencies, the resultant intensity varies at a far more lower rate, which is readily recorded by photodetectors. A special but practical implementation of the waves superposition involves two waves with an identical frequency, or more precisely, coherence, which lays the fundamental of interferometry.

In the study of interferometry, one of the crucial issues is to interpret the intensity patterns, termed as interferogram, of the coherent superposition. At the very beginning, the interferograms are analyzed manually by counting the interferometric fringe orders [14]. Later on, with the bloom of the digital image processing technique, the labor works are replaced by computer [15]. Plenty of algorithms are developed to track the interferometric fringes, resulting in certain degree of automation. Due to its simple implementation, today the intensity-based method still occupies a good portion of the analysis tasks, especially under the scenario that only a qualitative result is on request.

The advent of phase-shifting technique [16] gives another approach to the illustration of interferograms under a different framework. Compared with the fringe-tracking methods, phase-shifting techniques do not rely on finding the fringe centers, rather, it records a set

of interferograms with varying phase difference between the two interfering waves. There are many advantages of phase-shifting techniques, including 1) a higher accuracy, 2) an improved resolution, 3) automation, 4) real-time analysis, and 5) an analytical solution to the phase of the probe wave [17]. However, all of these merits depend on a single precondition, that is the introduced phase difference.

The varying phase difference between the two interfering waves is normally called phase shift. The accompanied device, which is used to generate the phase shift, is known as phase shifter, or put it more general, phase modulator. It is safe to say that the performance of an applying phase-shifting technique relies highly upon a phase modulator [18], although algorithms also have an impact. An ideal phase modulator brings the technique to its best efficiency, whereas an under-qualified phase modulation results in a failure of the investigation. Hence, it is crucial to develop or design a reliable phase shifter or a phase modulation method. Based on distinct physical principles, a number of phase modulators have been developed for the applications in specific scenarios, which is to say that most of the phase modulators are dedicated to a certain task. For example, the widely used piezo-electric transducer [19] can be hardly applied in a common-path configuration, in which the two interfering waves propagate essentially along the same light path. In such a case, Zeeman lasers [20, 21] succeed in introducing a feasible phase shift, but it fails in a time-related full-field investigation, because the frequency difference is in an order of megahertz, which is beyond the sampling rate of most array detectors. Although the instances illustrated above have not revealed the full view of the problem, they are indeed a representative of the unsolved issues. Consequently, the demand of a versatile phase modulator motivates the study in this thesis.

1.2   Objective

The objective of this thesis is deduced from a detailed definition of the aforementioned "versatile" in the sense of optical engineering. Within the scope of the present study, which deals with optical interferometric systems, the features of a versatile phase modulator are specified in the following aspects:

1. No mechanical motion unit. Mechanical movements, such as slide, translation, rotation, or extension, are very likely to introduce an error source in an optical system. Besides, the mechanical motion based method or device limits itself to static or quasi-static investigations, due to the mechanical inertia.

2. A proper and adjustable operating frequency. The operating frequency represents the rate of the phase change between the two interfering waves. A proper operating frequency considers the frequency requirements from both dynamic measurements

and the array detectors. An adjustable operating frequency gives the flexibility to satisfy the changing demand of the measurements.

3. A simultaneous and local modulation for both interfering waves. It is in desire that a single modulator shifts the phases of both interfering waves in the same time and at the same place. In other words, the phases of the interfering waves are modulated before the beam splitting. This renders the phase modulator versatile, because the phase modulation is carried out without being bothered by the followed-up light path arrangement or optical configuration.

Though some of the existing phase modulators possess one or two features listed above, throughout the study of this thesis, there are few reported modulators that cover all the three features. Therefore, the objective of this thesis is to design, develop and study a phase modulator which operates without any mechanical motion units, has a proper and adjustable operating frequency, and modulates the interfering waves locally and simultaneously.

1.3 Thesis Organization

This thesis consists of seven chapters. Chapter 1 presents a general background of the study, which starts from a brief history of optics. The scientific problem, to which this thesis is facing, is clarified, and the objective of this study is deduced from the facing problem. Chapter 2 is on literature review of the state of the art phase-shifting techniques. Meanwhile, the fundamentals of phase-shifting techniques, as well as the techniques related to interferometric systems, are introduced. In Chapter 3, as a solution to the aforementioned problem, a new phase modulator is described in terms of the theoretical principle, physical features, and practical implementation. Preliminary experiments are presented to verify the feasibility and functionality of the proposed phase modulator. From Chapter 4 to Chapter 6, the proposed phase modulator is coupled in three individual optical interferometric techniques, namely interferometry, holography, and differential phase contrast microscopy. At the end, Chapter 7 summaries the study in this thesis and draws the conclusions. As outlooks and prospects, some potential studies for further related investigations are proposed in this chapter as well.

Chapter 2

Fundamentals and State of the Art

In optical interferometric systems, phase-shifting techniques establish an approach to quantitative phase measurement. The phase to be measured is obtained from a set of phase-shifted interferograms, in which the data processing is normally known as phase retrieval [22]. Distinct phase retrieval algorithms, as well as phase shifters or modulators, are developed with diverse features to satisfy different requirements [23]. For clarity and efficiency, the phase to be measured is called target phase hereafter. In an optical interferometric system, the target phase is generally induced from the variation in optical path length (OPL), which is specified by the length of the light path and the refractive index. For a better generality, the concrete physical quantity that contributes to the target phase is dropped in this chapter, which means the demonstration and discussion are not related to a specific system. In the following, the fundamentals of phase retrieval are first introduced, which also includes the commonly used algorithms. Then, the state of the art in phase-shifting technique is reviewed to give a general picture of the field.

2.1 Fundamentals of Phase Retrieval

Before entering the technical details, some assumptions are made about the propagation medium. The medium is assumed to be linear, isotropic, homogeneous, nondispersive, and nonmagnetic. In such a manner, the scalar theory [24] is applied to describe the EM waves in a sufficient accuracy without deducing the technical parts from Maxwell's equations [25]. Besides, the wavefront is used in the description, which makes the illustration independent of the specific system. A monochromatic wave, which carries the object phase, is called object wave. The wavefront of the object wave is described in scalar theory by

$$\widetilde{U}_{obj}\left(\boldsymbol{\rho},t\right) = A_{obj}\left(\boldsymbol{\rho}\right) \cdot \exp\left\{-j\left[\omega_0 t + \phi_{obj}\left(\boldsymbol{\rho}\right)\right]\right\}, \qquad (2.1)$$

where $\widetilde{U}_{obj}$ stands for the complex amplitude (phasor) of the investigated wave, $\boldsymbol{\rho}$ is the position vector defining the observation plane, t represents the time, A_{obj} denotes the magnitude, j is the imaginary unit, ω_0 is the optical frequency of the wave, and ϕ_{obj} represents the object phase. Considering the sampling rate of most detectors, the intrinsic angular frequency, ω_0, of the optical wave is too high to be recorded.

For a successful investigation of the wavefront denoted by Equation (2.1), another wave, which is mutually coherent with the object wave, is considered. Generally, this auxiliary wave is termed as reference wave which normally appears as an ideal plane wave, or certain well-defined wave, emitted from the same source. It is noted that in certain circumstance, a modified object wave is also capable to act as the reference wave. In terms of the phase shift, it is possible to introduce a feasible phase shift in the reference wave, the object wave, or both waves. In the following illustration, a phase-shifted reference wave is assumed, which is emitted from the same source as the object wave. The wavefront of this reference wave is denoted by

$$\widetilde{U}_{ref}\left(\boldsymbol{\rho},t\right) = A_{ref}\left(\boldsymbol{\rho}\right) \cdot \exp\left\{-j\left[\omega_0 t + \phi_{ref}\left(\boldsymbol{\rho}\right) - \varphi_{sft}\left(t\right)\right]\right\}, \tag{2.2}$$

where ϕ_{ref} represents the phase distribution of the reference wave, φ_{sft} is the introduced phase shift in the reference wave. The coherent superposition of the object and the reference wavefronts gives rise to a resultant complex amplitude. The intensity distribution of the resultant complex amplitude is known as interferogram which can be detected by cameras. Mathematically, the interferogram is described by

$$\begin{aligned} I\left(\boldsymbol{\rho},t\right) &= \left[\widetilde{U}_{obj}\left(\boldsymbol{\rho},t\right) + \widetilde{U}_{ref}\left(\boldsymbol{\rho},t\right)\right] \cdot \left[\widetilde{U}_{obj}\left(\boldsymbol{\rho},t\right) + \widetilde{U}_{ref}\left(\boldsymbol{\rho},t\right)\right]^* \\ &= I_0\left(\boldsymbol{\rho}\right) \cdot \left\{1 + \gamma\left(\boldsymbol{\rho}\right) \cdot \cos\left[\phi_{obj}\left(\boldsymbol{\rho}\right) - \phi_{ref}\left(\boldsymbol{\rho}\right) + \varphi_{sft}\left(t\right)\right]\right\}, \end{aligned} \tag{2.3}$$

with the background intensity

$$I_0\left(\boldsymbol{\rho}\right) = A_{obj}^2\left(\boldsymbol{\rho}\right) + A_{ref}^2\left(\boldsymbol{\rho}\right), \tag{2.4}$$

and the visibility

$$\gamma\left(\boldsymbol{\rho}\right) = \frac{2 A_{obj}\left(\boldsymbol{\rho}\right) A_{ref}\left(\boldsymbol{\rho}\right)}{A_{obj}^2\left(\boldsymbol{\rho}\right) + A_{ref}^2\left(\boldsymbol{\rho}\right)}. \tag{2.5}$$

The descriptions above assume that the phases, ϕ_{obj} and ϕ_{ref}, are time-independent for an ease of illustration. For dynamic phases, certain phase-shifting techniques and algorithms are available to retrieve a time-dependent phase, which will be discussed later.

In Equation (2.3), the phase difference, $\phi_{obj} - \phi_{ref}$, is retrieved later by the phase-shifting technique. The physical meaning of the target phase is determined by the applied optical

configuration. For example, if the reference phase is set to zero, then the phase difference directly equals to the object phase. Considering that in Equation (2.3), the intensity, $I(\boldsymbol{\rho},t)$, is a function of the phase shift, $\varphi_{sft}(t)$, the one-dimensional (1-D) illustration of the intensity-phase shift function is shown in Figure 2.1.
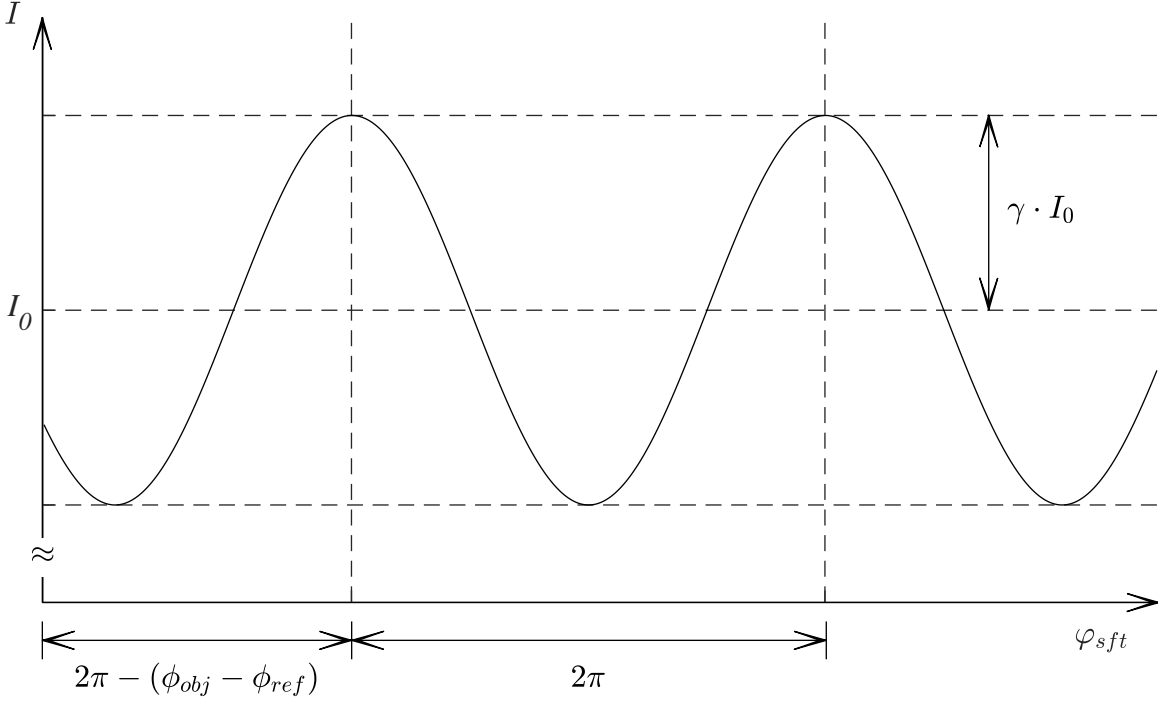

Figure 2.1: 1-D plot of the phase shift-intensity function.

Figure 2.1 shows a cosine curve of the intensity evolution at a probe point, resulting from a linearly varying phase shift. Three quantities are readily identified in the cosine curve, namely 1) the direct current (DC) offset is the background intensity, I_0, 2) the peak amplitude and the DC offset determine the visibility, γ, and 3) the point of intersection, for the vertical axis ($\varphi_{sft} = 0$) and the cosine curve, locates the target phase, ϕ_{tar}. It is worth noting that the target phase is obtained by locating the position of the peaks, valleys, or the equilibriums, rather than considering the intensity [26]. This fact implies the superiority of the phase-shifting technique, because normally the interferogram described by Equations (2.3)-(2.5) suffers from the intensity fluctuation.

Algorithms for retrieving the target phase from the phase-shifted interferograms generally fall into two categories [27], namely the discrete phase-shifting method and the time sequence method. The discrete phase-shifting method retrieves the target phase from a specific number of interferograms with a particular phase shift between them, whereas the time sequence method involves the analysis of a set of continuously captured interfer-

ograms with a linear varying phase shift in time sequence. In Subsections 2.1.1 and 2.1.2, the aforementioned two methods are introduced, respectively. A summary and a general overview of the phase retrieval techniques are given in Subsection 2.1.3.

2.1.1   Discrete Phase-Shifting Method

The discrete phase-shifting method is based on the fact that there are three unknowns in Equation (2.3), namely the DC offset, the visibility, and the target phase. In implementations, the number of the involved phase-shifted interferograms and the phase shift between them vary from algorithm to algorithm. For a minimum, it requires at least three individual phase-shifted interferograms to establish three mutually independent equations for a success in solving the unknowns [28]. In terms of the intensity-phase shift function shown in Figure 2.1, the requirement stated above indicates that a complete depiction of the cosine function demands a minimum of three individual points with well-defined phase shifts. In the following, the three-frame algorithm is first introduced as a basic algorithm, and then a general consideration is discussed, which gives an overview of the discrete phase-shifting method.

Being a theoretical basis, the three-frame algorithm is introduced [29]. The phase shift between adjacent interferograms is identical, noted by α. The three recorded intensities are described by

$$I_i\left(\boldsymbol{\rho},t_i\right) = I_0\left(\boldsymbol{\rho}\right) \cdot \left\{1 + \gamma\left(\boldsymbol{\rho}\right) \cdot \cos\left[\phi_{tar}\left(\boldsymbol{\rho}\right) + \varphi_{sft}\left(t_i\right)\right]\right\}, \; i = 1,2,3, \tag{2.6}$$

where $\phi_{tar} = \phi_{obj} - \phi_{ref}$ represents the phase difference between the wavefronts of the object and the reference waves, and

$$\varphi_{sft}\left(t_i\right) = \begin{cases} -\alpha & ,i = 1 \\ 0 & ,i = 2 \\ \alpha & ,i = 3 \end{cases}. \tag{2.7}$$

By applying the trigonometric identities to Equations (2.6) and (2.7) [26, 29], the target phase is evaluated by

$$\phi_{tar}\left(\boldsymbol{\rho}\right) = \arctan\left[\frac{1 - \cos\alpha}{\sin\alpha} \cdot \frac{I_1\left(\boldsymbol{\rho}\right) - I_3\left(\boldsymbol{\rho}\right)}{2I_2\left(\boldsymbol{\rho}\right) - I_1\left(\boldsymbol{\rho}\right) - I_3\left(\boldsymbol{\rho}\right)}\right], \tag{2.8}$$

and the background intensity and the visibility of the interferograms are calculated respectively by

$$I_0\left(\boldsymbol{\rho}\right) = \frac{I_1\left(\boldsymbol{\rho}\right) + I_3\left(\boldsymbol{\rho}\right) - 2I_2\left(\boldsymbol{\rho}\right) \cdot \cos\alpha}{2\left(1 - \cos\alpha\right)}, \tag{2.9}$$

and

$$\gamma\left(\boldsymbol{\rho}\right) = \frac{\left\{\left(1 - \cos\alpha\right)^2 \left[I_1\left(\boldsymbol{\rho}\right) - I_3\left(\boldsymbol{\rho}\right)\right]^2 + \sin^2\alpha \left[2I_2\left(\boldsymbol{\rho}\right) - I_1\left(\boldsymbol{\rho}\right) - I_3\left(\boldsymbol{\rho}\right)\right]^2\right\}^{1/2}}{\left[I_1\left(\boldsymbol{\rho}\right) + I_3\left(\boldsymbol{\rho}\right) - 2I_2\left(\boldsymbol{\rho}\right)\cdot\cos\alpha\right]\sin\alpha}. \quad (2.10)$$

It is important to note that there are two schemes of altering the phase and capturing the interferograms. One is the phase-stepping scheme [30], in which the phase is shifted step by step. During each capturing, the phase is stable. The other is the integrating bucket scheme [31, 32], which relies on a time-varying phase shift. The interferograms are captured while the phase is shifting. Figure 2.2 gives a detailed illustration about these two schemes.

Figure 2.2: Phase-stepping and integrating bucket.
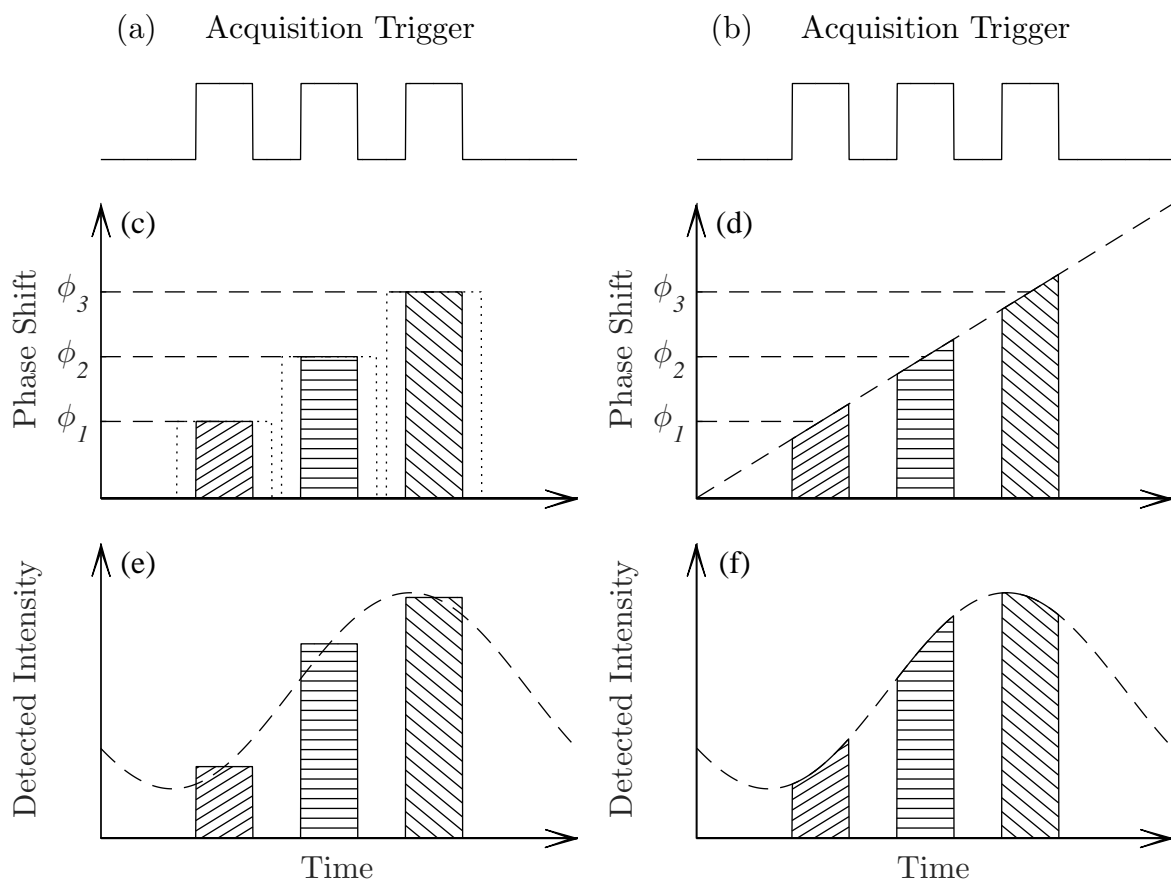
The three-frame algorithm is taken as an example in Figure 2.2. As the name indicated, three interferometric intensities are collected at different phase shifts. The phase shifts are shown as ϕ_1, ϕ_2, and ϕ_3. It is obvious that in the phase-stepping scheme [Figure 2.2(c)], the phase is shifted exactly by the announced amount, whereas in the integrating bucket

scheme [Figure 2.2(d)], the labeled quantities are only the nominal value of the phase shift. To demonstrate the integrating bucket scheme, the phase is assumed to change by an amount of Δ during each acquisition. The intensity is then given by [33]

$$
\begin{aligned}
I_i\left(\boldsymbol{\rho},t_i,\Delta\right) =& \frac{1}{\Delta} \int_{\phi_i-\Delta/2}^{\phi_i+\Delta/2} I_0\left(\boldsymbol{\rho}\right)\cdot\left\{1+\gamma\left(\boldsymbol{\rho}\right)\cdot\cos\left[\phi_{tar}\left(\boldsymbol{\rho}\right)+\phi_i\left(t_i\right)\right]\right\}\mathrm{d}\phi_i \\
=& I_0\left(\boldsymbol{\rho}\right)\cdot\left\{1+\gamma\left(\boldsymbol{\rho}\right)\cdot\left(\operatorname{sinc}\frac{\Delta}{2}\right)\cdot\cos\left[\phi_{tar}\left(\boldsymbol{\rho}\right)+\phi_i\left(t_i\right)\right]\right\},
\end{aligned}
\tag{2.11}
$$

with $\operatorname{sinc}\frac{\Delta}{2} = \left(\sin\frac{\Delta}{2}\right)/\frac{\Delta}{2}$ and $i = 1,2,3$ being the counts of the phase shift. Recalling Equation (2.6), which describes the phase-shifted interferograms in the phase-stepping scheme, the interferograms captured by the integrating bucket scheme show a reduction in the visibility. The integration of the intensity with a time-varying phase shift is regarded as an average to the interferogram over time. In the case of that $\Delta = 2\pi$, the visibility in Equation (2.11) goes to zero, which indicates that there is no observable phase shift any longer. At another condition that $\Delta \to 0$, the two schemes are then equivalent. Hence, the discrete phase-shifting method is feasible for both schemes to retrieve the target phase as long as the integrating bucket scheme gives rise to a sufficient visibility. Compared with the phase-stepping scheme, the integrating bucket scheme provides another possibility of phase retrieval. It is shown in Subsection 2.1.2 that by combining the integrating bucket scheme with the time sequence method, dynamic measurements of the target phase are accomplished. Hereafter, for convenience, the sinc function is assumed to be unit, so that the phase-stepping and the integrating bucket schemes share an identical description.

For a general analysis of the discrete phase-shifting method, a least-squares solution of N phase-shifted interferograms is considered [33]. The principle lays on the fact that the intensity of the interferograms varies in a sinusoidal manner under the function of a known phase shift. Equation 2.3 is then rewritten by

$$
I_i\left(\boldsymbol{\rho},i\right) = a_0\left(\boldsymbol{\rho}\right) + a_1\left(\boldsymbol{\rho}\right)\cdot\cos\varphi_i + a_2\left(\boldsymbol{\rho}\right)\cdot\sin\varphi_i,
\tag{2.12}
$$

where

$$
a_0\left(\boldsymbol{\rho}\right) = I_0\left(\boldsymbol{\rho}\right),
\tag{2.13a}
$$

$$
a_1\left(\boldsymbol{\rho}\right) = I_0\left(\boldsymbol{\rho}\right)\gamma\left(\boldsymbol{\rho}\right)\cdot\cos\left[\phi_{tar}\left(\boldsymbol{\rho}\right)\right],
\tag{2.13b}
$$

$$
a_2\left(\boldsymbol{\rho}\right) = -I_0\left(\boldsymbol{\rho}\right)\gamma\left(\boldsymbol{\rho}\right)\cdot\sin\left[\phi_{tar}\left(\boldsymbol{\rho}\right)\right],
\tag{2.13c}
$$

and $\varphi_i = \varphi_{sft}\left(t_i\right)$ represents the phase shift. Equation (2.12) yields an issue, the task of which is to seek the optimum solution for the three unknowns in a least-squares sense. The approach is formulated by minimizing the following objective function [26, 34] (or

called cost function in mathematics):

$$E^2\left(\boldsymbol{\rho}\right) = \sum_{i=1}^{N} \left[I_i\left(\boldsymbol{\rho},i\right) - a_0\left(\boldsymbol{\rho}\right) - a_1\left(\boldsymbol{\rho}\right) \cdot \cos\varphi_i - a_2\left(\boldsymbol{\rho}\right) \cdot \sin\varphi_i\right]. \qquad (2.14)$$

The cost function is minimized by nulling its partial derivatives with respect to each of the three parameters, namely a_0, a_1, and a_2, respectively, given by

$$\begin{bmatrix} N & \sum_{i=1}^{N}\cos\varphi_i & \sum_{i=1}^{N}\sin\varphi_i \\ \sum_{i=1}^{N}\cos\varphi_i & \sum_{i=1}^{N}\cos^2\varphi_i & \sum_{i=1}^{N}\cos\varphi_i\sin\varphi_i \\ \sum_{i=1}^{N}\sin\varphi_i & \sum_{i=1}^{N}\cos\varphi_i\sin\varphi_i & \sum_{i=1}^{N}\sin^2\varphi_i \end{bmatrix} \begin{bmatrix} a_0 \\ a_1 \\ a_2 \end{bmatrix} = \begin{bmatrix} \sum_{i=1}^{N}I_i \\ \sum_{i=1}^{N}I_i\cos\varphi_i \\ \sum_{i=1}^{N}I_i\sin\varphi_i \end{bmatrix}. \qquad (2.15)$$

After the three parameters are determined by solving the linear system of equations in Equation (2.15), the target phase is calculated by

$$\phi_{tar}\left(\boldsymbol{\rho}\right) = \arctan\left[-\frac{a_2\left(\boldsymbol{\rho}\right)}{a_1\left(\boldsymbol{\rho}\right)}\right]. \qquad (2.16)$$

In the general illustration of the discrete phase shift above, it is demanded that the phase is shifted to at least three individual positions over a single period of the sinusoidal function. In the implementations, certain precondition or restrict to the phase shift simplifies the calculation greatly, e.g., an evenly spaced phase shift. A most common example is the four-frame algorithm [35], in which the phase shifts are set to

$$\varphi_i = \left(i-1\right)\frac{\pi}{2}. \qquad (2.17)$$

Considering this special case, only the diagonal elements in the first matrix of Equation (2.15) are non-zero. This fact leads to a straightforward solution of the target phase, denoted by

$$\phi_{tar}\left(\boldsymbol{\rho}\right) = \arctan\left[\frac{I_2\left(\boldsymbol{\rho}\right) - I_4\left(\boldsymbol{\rho}\right)}{I_3\left(\boldsymbol{\rho}\right) - I_1\left(\boldsymbol{\rho}\right)}\right]. \qquad (2.18)$$

The aforementioned three-frame algorithm [28] is also accessible by investigating Equation (2.15). Special attention is required upon the basis behind. The solutions of either the three- or four-frame algorithms are derived analytically without the consideration of the least-squares method. In other words, the target phase is retrieved from its physical property instead of a least-squares fitting. However, in terms of the mathematical descriptions, the least-squares solutions are equivalent to the analytical solutions.

The least-squares solution to the target phase lays a basis for a family of algorithms, which normally called N-frame algorithms. These algorithms are various in the phase shift arrangement, including the amount and the number of the shift. Considering the evenly spaced phase-shift arrangement, algorithms with different number (N) of frames possess their respective unique performance in suppressing the measurement noises and errors. Dedicated algorithms are developed to accomplish certain specific requirements. For example, the Carré algorithm [36, 37] only requires a constant phase shift between each frame without knowing the exact amount of the phase shift. The averaging algorithms [38, 39] and the Hariharan algorithm [40] aim to reduce the linear phase shift error, but by using different schemes. The 2+1 algorithm [41–43] gives a rise in the time resolution of a time-varying target phase.

In fact, regarding the number of frames, there is no theoretical limitation in developing algorithms which use the discrete phase-shifting method. However, for a good number of frames, another approach to the target phase is ready to be considered. That is the time sequence method. In Subsection 2.1.2, the principle, the advantages, as well as the disadvantages of the time sequence method are illustrated.

2.1.2   Time Sequence Method

A linearly time-varying phase shift is normally configured for the time sequence method, and the integrating bucket scheme is applied to record the interferograms [see Figure 2.2(b), (d), and (f)]. The sampling interval and the integrating (exposure) time are both the same from frame to frame.

This analysis routine for a large number of frames is based on the least-squares solution, which is described by Bruning *et al.* in 1974 [16]. Under such a phase-shifting configuration, the collected interferograms are first analyzed by the generalized least-squares method. As illustrated in the previous subsection, an evenly spaced phase shift over a full period leads to a simplified solution to the generalized least-squares method. The linear phase shift is denoted by $\varphi_i = i2\pi p/n$ with i being the ordinal number of the frames. The integer n denotes the number of frames within one single period of the sinusoidal intensity variation. The other integer p represents the number of periods over which $N = np$ frames are collected. Equation (2.15) is then readily simplified as

$$
\begin{bmatrix} np & 0 & 0 \\ 0 & \dfrac{np}{2} & 0 \\ 0 & 0 & \dfrac{np}{2} \end{bmatrix} \begin{bmatrix} a_0(\boldsymbol{\rho}) \\ a_1(\boldsymbol{\rho}) \\ a_2(\boldsymbol{\rho}) \end{bmatrix} = \begin{bmatrix} \sum\limits_{i=1}^{np} I_i(\boldsymbol{\rho}) \\ \sum\limits_{i=1}^{np} I_i(\boldsymbol{\rho}) \cos \varphi_i \\ \sum\limits_{i=1}^{np} I_i(\boldsymbol{\rho}) \sin \varphi_i \end{bmatrix} . \tag{2.19}
$$

By solving Equation (2.19) and using the well-known arctangent function in Equation (2.16), the target phase is retrieved by

$$\phi_{tar}(\boldsymbol{\rho}) = \arctan\left[-\frac{\sum\limits_{i=1}^{np} I_i(\boldsymbol{\rho})\sin\varphi_i}{\sum\limits_{i=1}^{np} I_i(\boldsymbol{\rho})\cos\varphi_i}\right]. \tag{2.20}$$

Provided that the sinusoidal intensity variation is sufficiently sampled, a selection of well-established tools are readily to be used for the retrieval of the target phase. Among others, Fourier analysis is one of the most familiar and commonly used methods. Hence, in this subsection, the time sequence method is demonstrated by the Fourier analysis approach.

Rather than investigating individual intensities, the Fourier analysis approach emphasizes the study of the relations among them, namely the frequencies. Though the Fourier fringe method is proposed by M. Takeda *et al.* [44] for the analysis of the spatial phase shift, it is compatible to describe the temporal phase shift, because they share the same fundamental. An alternative expression for Equation (2.3) is denoted by

$$\begin{aligned} I(\boldsymbol{\rho},t) =& I_0(\boldsymbol{\rho}) + I_0(\boldsymbol{\rho})\gamma(\boldsymbol{\rho})\cdot\cos\left[\phi_{tar}(\boldsymbol{\rho}) + \varphi_{sft}(t)\right] \\ =& a(\boldsymbol{\rho}) + c(\boldsymbol{\rho})\exp\left[j\varphi_{sft}(t)\right] + c^*(\boldsymbol{\rho})\exp\left[-j\varphi_{sft}(t)\right], \end{aligned} \tag{2.21}$$

where

$$a(\boldsymbol{\rho}) = I_0(\boldsymbol{\rho}), \tag{2.22a}$$

$$c(\boldsymbol{\rho}) = \frac{1}{2}I_0(\boldsymbol{\rho})\gamma(\boldsymbol{\rho})\exp\left[j\phi_{tar}(\boldsymbol{\rho})\right]. \tag{2.22b}$$

In Equation (2.21), Euler's formula is applied to the cosine function and the raised asterisk represents the complex conjugation. The linearly time-varying phase shift, φ_{sft}, is specified by

$$\varphi_{sft}(t) = \omega_{sft}\cdot t, \tag{2.23}$$

with ω_{sft} being the angular frequency of the phase shift in radians per second (rad/s). For an ease of illustration, continuous mathematics is adopted in the following deductions, though the sampling is discrete in both space and time. With respect to the time axis, Fourier transform is applied to Equation (2.21). A series of intensities in time sequence is then converted to frequency domain, denoted by

$$\mathscr{F}\left[I(\boldsymbol{\rho},t)\right](\boldsymbol{\rho},f_t) = A(\boldsymbol{\rho},f_t) + C(\boldsymbol{\rho},f_t - f_{sft}) + C^*(\boldsymbol{\rho},f_t + f_{sft}), \tag{2.24}$$

where $\mathscr{F}\left[\,\cdot\,\right]$ stands for the Fourier transform operation, f_t denotes the variable in the

Fourier frequency domain, capital letters, A and C, represent the Fourier spectrum of the corresponding items in Equation (2.21), and f_{sft} is the frequency of the sinusoidal varying intensity determined by $f_{sft} = \omega_{sft}/2\pi$. It is necessary to give a brief illustration to Equations (2.21) and (2.24). Firstly, the position vector, $\boldsymbol{\rho}$, is only used to indicate the probe point, namely where the intensity is observed. The position vector itself is not involved in the current deduction. Secondly, if an ideal condition is assumed, then the background intensity, $a(\boldsymbol{\rho})$, is a constant. Consequently, its Fourier spectrum, $A(\boldsymbol{\rho},f_t)$ appears as the DC component. Thirdly, considering the item, $c(\boldsymbol{\rho})$, which relates to the target phase, its Fourier spectrum has an obvious frequency shift toward the higher frequency by a value of f_{sft}, which results from the applied phase-shift configuration. At last, the Fourier spectral components, $C(\boldsymbol{\rho},f_t - f_{sft})$ and $C^*(\boldsymbol{\rho},f_t + f_{sft})$, are mutually conjugated. As a result, the three components, $A(\boldsymbol{\rho},f_t)$, $C(\boldsymbol{\rho},f_t - f_{sft})$, and $C^*(\boldsymbol{\rho},f_t + f_{sft})$, have a trimodal distribution in the Fourier frequency domain, as shown in Figure 2.3(a).
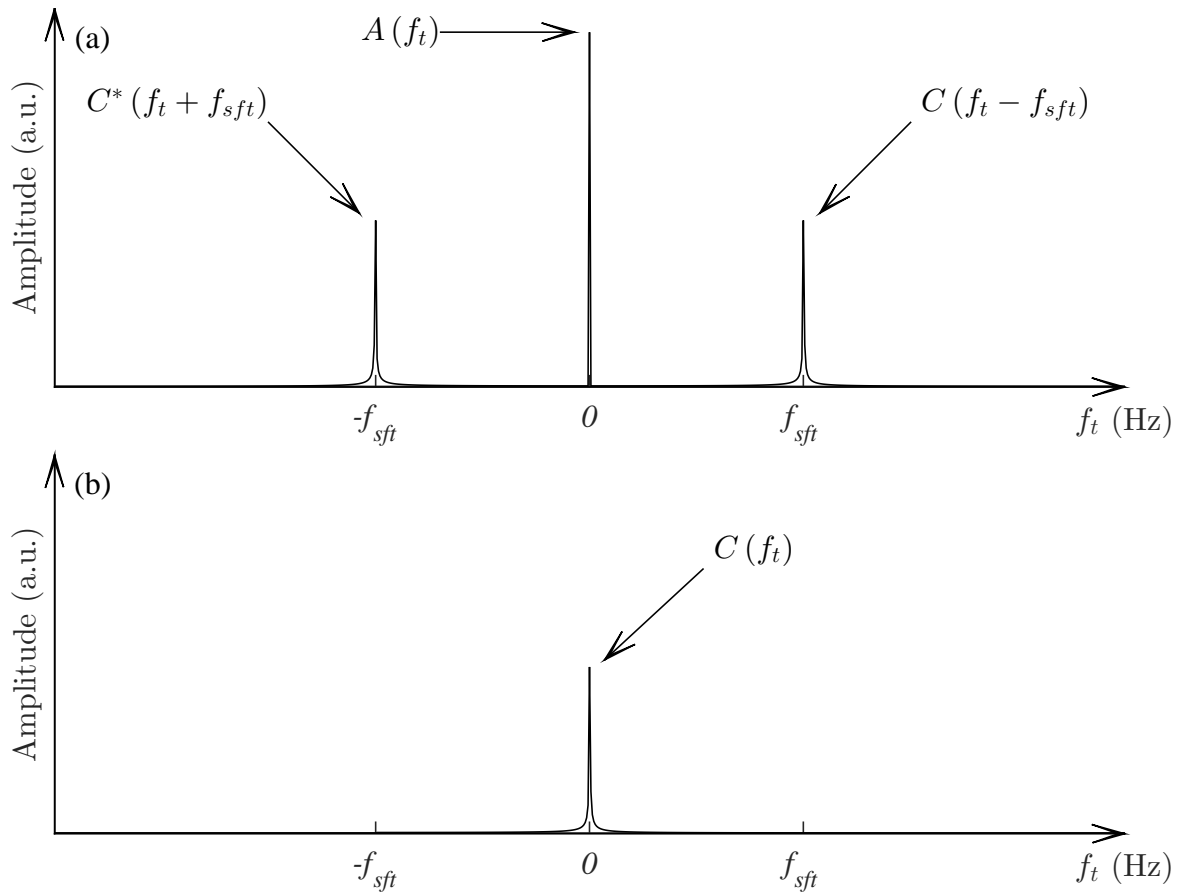

Figure 2.3: Fourier spectrum of a series intensities in time sequence.

It is noted that, in the current illustration, there is neither spectrum broadening nor

frequency shift regarding the spectral component, $C\left(f_t - f_{sft}\right)$. The reason is that the discussions are still restricted to ideal conditions and the target phase is assumed to be time-independent. Thus, to figure out the target phase, the +1 order of the side lobe, which refers to $C\left(f_t - f_{sft}\right)$ and the neighborhood frequencies, is isolated by a frequency filter. Afterwards, the isolated +1 order of the side lobe is translated by f_{sft} towards the origin [see Figure 2.3(b)]. The complex function in Equation (2.22b) is computed by conducting an inverse Fourier transform to the modified frequency spectrum, denoted by

$$c\left(\boldsymbol{\rho}\right) = \mathscr{F}^{-1}\left[C\left(\boldsymbol{\rho}, f_t\right)\right], \tag{2.25}$$

where $\mathscr{F}^{-1}\left[\,\cdot\,\right]$ stands for the inverse Fourier transform operation. At last, the target phase is calculated by

$$\phi_{tar}\left(\boldsymbol{\rho}\right) = \arctan\left\{\frac{\mathrm{Im}\left[c\left(\boldsymbol{\rho}\right)\right]}{\mathrm{Re}\left[c\left(\boldsymbol{\rho}\right)\right]}\right\}, \tag{2.26}$$

with $\mathrm{Re}\left[\,\cdot\,\right]$ and $\mathrm{Im}\left[\,\cdot\,\right]$ being the operations of getting the real and the imaginary parts, respectively. When the amplitude is requested as well, both the amplitude and the target phase are accessible by taking the logarithm of the complex function, given by

$$\log\left[c\left(\boldsymbol{\rho}\right)\right] = \log\left[\left(1/2\right) I_0\left(\boldsymbol{\rho}\right) \gamma\left(\boldsymbol{\rho}\right)\right] + j \cdot \phi_{tar}\left(\boldsymbol{\rho}\right), \tag{2.27}$$

where the real part contains the amplitude and the imaginary parts is the target phase. In all the notations above, there is no time parameter in the target phase, because it is time-independent. However, as a matter of fact, the time sequence method retrieves the phase at each individual sampling point along the time axis. As a result, although the target phase is time-independent, the time sequence method gives a series of target phase with an identical value in time sequence.

Next, the temporal feature of the time sequence is demonstrated by considering a time-dependent object wave, denoted by

$$\widetilde{U}_{obj}\left(\boldsymbol{\rho}, t\right) = A_{obj}\left(\boldsymbol{\rho}\right) \cdot \exp\left\{-j\left[\omega t + \phi_{obj}\left(\boldsymbol{\rho}, t\right)\right]\right\}. \tag{2.28}$$

In Equation (2.28), a time parameter is found in the object phase, ϕ_{obj}. Consequently, Equation (2.21) is rewritten by considering the time parameter, which is given by

$$I\left(\boldsymbol{\rho}, t\right) = a\left(\boldsymbol{\rho}\right) + c\left(\boldsymbol{\rho}, t\right) \exp\left[j\varphi_{sft}\left(t\right)\right] + c^*\left(\boldsymbol{\rho}, t\right) \exp\left[-j\varphi_{sft}\left(t\right)\right], \tag{2.29}$$

where $c\left(\boldsymbol{\rho}, t\right)$ has a similar expression as it does in Equation (2.22b), but now all the

notations are time-dependent, denoted by

$$c\left(\boldsymbol{\rho},t\right) = \frac{1}{2}I_0\left(\boldsymbol{\rho}\right)\gamma\left(\boldsymbol{\rho}\right)\exp\left[j\phi_{tar}\left(\boldsymbol{\rho},t\right)\right]. \tag{2.30}$$

In this time-dependent demonstration, the Fourier transform of the series of intensities in time sequence is still able to be described by Equation (2.22), which indicates that the frequency spectrum stays unchanged in general. However, the details of the trimodal distribution are changed due to the time-dependent wavefront, as shown in Figure 2.4.
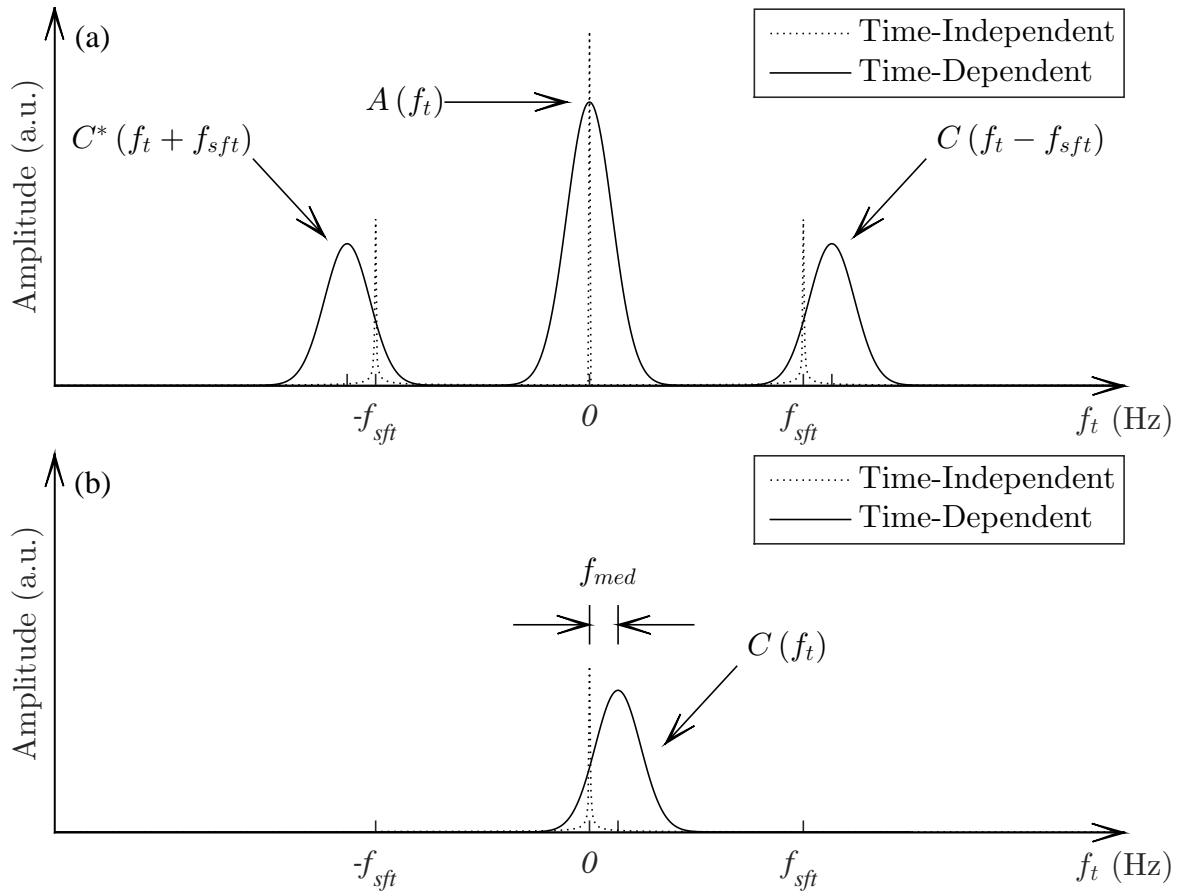

Figure 2.4: Fourier spectrum of a time-dependent measurement.

Spectrum broadening, as well as frequency shift, is observed in the Fourier spectrum. The broadening in the DC component, $A\left(f_t\right)$, is normally considered as a result of the low frequency noise in the surroundings. Regarding the conjugated side lobes, $C\left(f_t - f_{sft}\right)$ and $C^*\left(f_t + f_{sft}\right)$, the spectrum broadening and the frequency shift come from the time-dependent phase of the object wave. Specifically, a non-linear target phase results in a signal with harmonics in multiple orders, which further broadens the conjugated side lobes in the Fourier domain. Meanwhile, the peaks of the side lobes are shifted by f_{med},

which is the median frequency of the time-dependent target phase [45], denoted by

$$f_{med}\left(\boldsymbol{\rho}\right) = \mathscr{M}\left[\frac{1}{2\pi} \cdot \frac{\partial\phi_{tar}\left(\boldsymbol{\rho},t\right)}{\partial t}\right], \tag{2.31}$$

where $\mathscr{M}\left[\,\cdot\,\right]$ stands for the median (middle number) of the given data set. In Equation (2.31), the given data set is the instant frequency of the target phase. To retrieve this time-dependent target phase, the isolation, translation, and inverse transformation are applied to the desired side lobe in a similar manner introduced above. In the implementation, it is necessary to consider two parameters for a successful target phase retrieval, namely the window width of the frequency filter and the frequency capacity of the operating configuration. The concerned parameters are denoted by

$$W_{filter}\left.\right|_{\min} = \frac{1}{2\pi} \cdot \left.\frac{\partial\phi_{tar}\left(\boldsymbol{\rho},t\right)}{\partial t}\right|_{\max} - \frac{1}{2\pi} \cdot \left.\frac{\partial\phi_{tar}\left(\boldsymbol{\rho},t\right)}{\partial t}\right|_{\min}, \tag{2.32}$$

and

$$f_{sft} \geq \left\|\frac{1}{2\pi} \cdot \frac{\partial\phi_{tar}\left(\boldsymbol{\rho},t\right)}{\partial t}\right\|_{\max}. \tag{2.33}$$

Equation (2.32) determines the narrowest window width of the frequency filter, which indicates that the filter is expected to cover the full range of the instant frequency of the target phase. Equation (2.33) shows that the maximum absolute value of the instant frequency is required to be no greater than the phase shift induced frequency. Generally, in terms of signal processing, the time sequence method with a linearly time-varying phase shift is regarded as a heterodyne technique [46], in which the phase shift induced frequency serves as a temporal carrier frequency. Hence, the two preconditions stated above actually come from the heterodyne technique. By fulfilling these preconditions and through a similar procedure which has been demonstrated in the time-independent case, a time series of the time-dependent target phase is retrieved successfully.

2.1.3 Summary

In this section, the phase retrieval algorithms are summarized. The demonstration focuses on the basic principle instead of specific implementations. The presented categories are a general classification of the phase retrieval techniques. Within the phase-shifting framework, there are many other algorithms and techniques, e.g., the 3+1 frames method [47] for the discrete phase-shifting method, and the Wavelet transform [48], as well as the Hilbert transform [49], for the time sequence method. Dedicated phase-shifting arrangements enable specific techniques. For example, the phase lock detection technique involves a continuous phase shift in a linear variation. Each of the phase retrieval techniques has

its unique features and preferred implementation.

The phase shift arrangements discussed above are all time-varying phase shifts, regardless of the fact that it is discrete or in sequence. From a mathematical view, if the phase is shifted along the spatial axis instead of the temporal axis, another approach emerges, namely the spatial phase-shifting technique [50–52]. Generally, by exchanging the temporal axis with the spatial axis, most of the temporal phase retrieval algorithms are effective in the spatial phase-shifting arrangements. A superior feature of the spatial phase-shifting technique is its real-time performance, but at a cost of a reduced spatial resolution.

Regarding practical implementations, no matter in lab or at site, an adequate analysis of the measurement requirements and conditions is a pre-step by considering the noise distribution, the time and space resolutions, the optical configuration compatibility, etc. Thus, a proper selection or a specific development of the phase-shifting technique is achieved.

2.2   State of the Art in Phase-Shift Technique

The previous section gives an overview of the mathematical description to the phase retrieval algorithms which are based on the phase-shifting technique. All the phase shifts are assumed to be ideal without considering the issue of how the phase is shifted. A successful phase retrieval requires not only a suitable algorithm, but also a reliable phase-shifting device or method. More importantly, the physical performance of the phase-shifting technique is mostly determined by the phase modulator, because an inappropriate behavior of the phase shift results in an increasing uncertainty or even brings the retrieval algorithms out of function. Meanwhile, certain specific phase retrieval algorithms rely strongly on a dedicated phase-shifting device or method. Therefore, a detailed treatment of the existing phase-shifting techniques and methods is presented in this section.

Referring to the mathematical description of an interferogram [see Equation (2.3)], it is customary to consider a phase shift in the cosine function from two generalized aspects, i.e., the optical path length (OPL) and the optical frequency. A successful phase shift involves altering the optical path difference (OPD) or introducing an additional frequency difference between the two interfering waves. Hence, for the phase-shifting devices and methods, the following demonstration is split into two subsections according to the origins of the phase shift.

2.2.1   Optical Path Length Based Phase Shift

The definition of optical path length (OPL) is the product of the geometric path length of the wave propagation and its corresponding refractive index. Essentially, the OPL

characterizes the time of flight for an optical wave. Considering a given OPL, the time of flight is identical for waves with the same wavelength. The optical path difference (OPD) describes the difference between the OPLs. In terms of phase, an OPD indicates a phase difference between the two interfering waves [53], denoted by

$$\Delta\varphi = \frac{2\pi}{\lambda} \underbrace{\left(n_{obj}L_{obj} - n_{ref}L_{ref}\right)}_{\text{OPD}}. \tag{2.34}$$

It is obvious that a phase shift is introduced in the interference by altering the geometric path length or the distribution of the refractive index in one or both waves.

Piezo-Electric Transducer   The most commonly used method for introducing a time-varying phase shift is based on the piezo-electric transducer (PZT) [54–56]. The PZT is a device that has a length change response to the externally applied voltage. It is possible to carry out the demanded motion within a wavelength by a careful control of the applied voltage. Both of the discrete and the continuous phase shifts are able to be introduced. Normally, the reference mirror is attached to a PZT which translates the mirror along the axial direction, as shown in Figure 2.5.
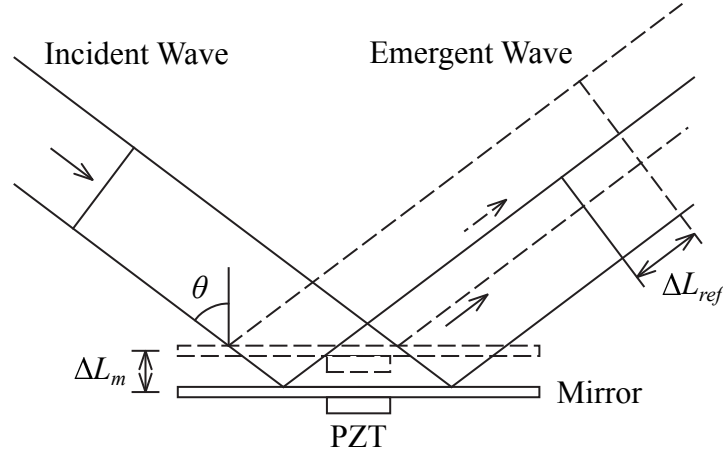

Figure 2.5: Phase shift induced by a PZT-driven reference mirror.

In order to give a general illustration, the incident wave in Figure 2.5 is set oblique at an angle of θ with respect to the mirror normal. The incident wave is regarded as a plane wave, and the lateral displacement of the emergent wave is ignored. Assuming that the PZT has a normal expansion of ΔL_m, the difference of the geometric path length is denoted by

$$\Delta L_{ref} = 2\Delta L_m \cdot \cos\theta. \tag{2.35}$$

Consequently, the phase shift is given by

$$\varphi_{sft} = \underbrace{\frac{2\pi}{\lambda}\left(n_{obj}L_{obj} - n_{ref}L_{ref}\right)}_{\Delta\varphi_a} - \underbrace{\frac{2\pi}{\lambda}\left[n_{obj}L_{obj} - n_{ref}\left(L_{ref} - \Delta L_{ref}\right)\right]}_{\Delta\varphi_b}$$

$$= \frac{2\pi}{\lambda}n_{ref} \cdot 2\Delta L_m \cos\theta, \tag{2.36}$$

where $\Delta\varphi_a$ and $\Delta\varphi_b$ stand for the phase difference between the two interfering waves, before and after the phase shift, respectively. By applying a distinct voltage, the expansion of the PZT is changed, and, further, the time-varying phase shift is introduced.

Besides, it is also capable to introduce a desired phase shift by a radially expanding PZT, which is coupled with a highly birefringent (HiBi) fiber [57–59], as shown in Figure 2.6.
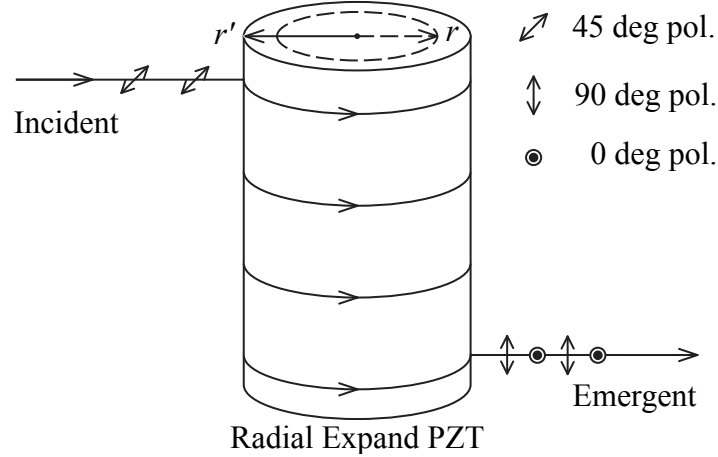

Figure 2.6: Phase shift induced by a stretched HiBi fiber which is driven by a radially expanding PZT.

A HiBi fiber with a given length is wrapped around a cylindrical PZT at a specific number of turns. A half-wave plate (HWP) (not shown in the figure) is readily used to align the incident polarization at 45 deg with respect to the fiber birefringence axis. Thus, inside the HiBi fiber, the incident wave is split equally into the two orthogonally polarized modes (eigenmodes), which are polarized at 0 deg and 90 deg, respectively. The two modes are spatially separable by the optical polarization element (e.g., a Wollaston prism) upon request, but a conventional use of the PZT-HiBi phase shifter is in the common-path configuration, in which no significant separation or only lateral shear is required. Considering a radial expansion of the PZT, a variation of the strain is found in the wrapped HiBi fiber. The varying strain induces distinct behaviors of the refractive indices for respective modes. Recalling Equation (2.34), when the two refractive indices, n_{obj} and n_{ref}, change in different manners, the phase difference between the two interfering

waves is altered, which expresses as a phase shift in the PZT-HiBi fiber-based phase shifter. In practical implementations, the PZT-HiBi phase shifter requires a calibration to draw a look-up table. It is hardly to summarize a simple equation, because the mathematical relation between the applied voltage and the phase shift depends strongly on how the fiber is wrapped by considering the radius of the PZT, the length of the HiBi fiber, and the number of turns.

Tilted Glass Plate   Tilted glass plate (plane-parallel plate) [60] is an alternative option of introducing a phase shift in one of the interfering waves, as shown in Figure 2.7.
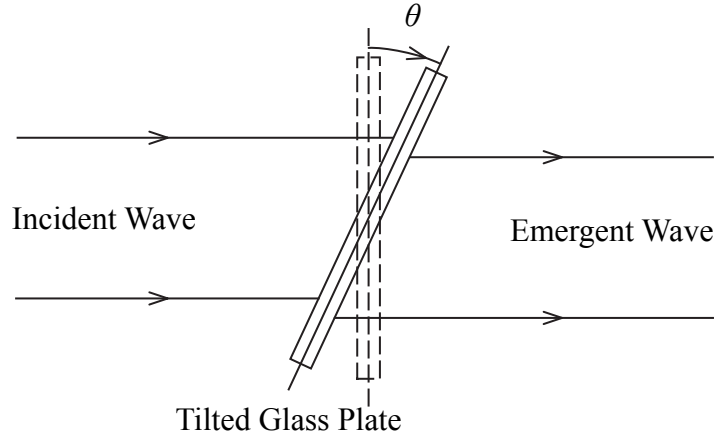

Figure 2.7: Phase shift induced by a tilted glass plate.

Considering the incident wave is the reference plane wave, a normal incidence onto the glass plate is assumed as the initial state of the configuration (dashed line in Figure 2.7). To introduce the phase shift, the glass plate is tilted by an angle of θ. The phase shift is then given by [60]

$$\varphi_{sft} = \underbrace{\frac{2\pi}{\lambda} \left\{ \frac{d}{\cos\theta_r} n_g + \left[d - \frac{d}{\cos\theta_r} \cos\left(\theta - \theta_r\right) \right] n_0 \right\}}_{\text{tilted}} - \underbrace{\frac{2\pi}{\lambda} \left(dn_g \right)}_{\text{initial}}$$

$$= \frac{2\pi}{\lambda} \left\{ \left(\frac{1}{\cos\theta_r} - 1 \right) dn_g + \left[1 - \frac{\cos\left(\theta - \theta_r\right)}{\cos\theta_r} dn_0 \right] \right\}, \tag{2.37}$$

where d stands for the thickness of the glass plate, n_0 and n_g are the refractive indices of the air and the glass, respectively, θ_r is the refractive angle inside the glass plate. According to Snell's law, the refractive angle, θ_r, is denoted by

$$\theta_r = \arcsin\left(\frac{n_0}{n_g} \sin\theta \right). \tag{2.38}$$

Equation (2.37) shows that a varying phase shift is introduced by tilting the glass plate to a different angle. The essence of the tilted glass plate method is the redistribution of the refractive index in space. In implementations, to give a reliable phase shift, the incident beam is required to be collimated, and the glass plate is expected to be in high and homogeneous optical quality.

2.2.2   Optical Frequency Based Phase Shift

Rather than modifying the optical path length (OPL), it is also feasible to induce a time-varying phase shift by introducing a detectable frequency in one or both interfering waves. Referring to Equation (2.3), the introduced frequency is expressed as an individual item in the cosine function. The optical frequency based phase shift has a widely range of application. Especially, it is preferred in the time sequence phase retrieval method, because a linearly time-varying phase shift is readily introduced by the optical frequency method. The mathematical description of an introduced linearly time-varying phase shift is shown in Subsection 2.1.2. In the following, the demonstration focuses on the hardware.

Sliding Grating   Diffraction gratings are optical components with spatially periodic structure. The incident wave is spatially modulated and diffracted into several different orders. When a diffraction grating is translated vertically with respect to the propagation of the incident wave, a Doppler shift is introduced in the diffracted waves, as shown in Figure 2.8.
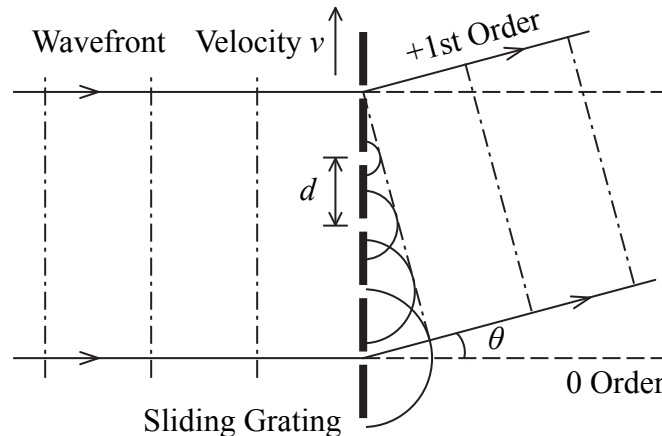

Figure 2.8: Phase shift induced by a sliding diffraction grating.

Assuming that the grating period is d (grating constant $= 1/d$) and the sliding velocity is v, the angular frequency shift in terms of phase is denoted by [61, 62]

$$\Delta\omega = 2\pi m v/d, \tag{2.39}$$

where m is the diffraction order. Equation (2.39) shows that the angular frequency shift depends on the order of diffraction, so the final resultant phase shift is related to the selection of the order. For example, when the two interfering waves are the +1st and the 0 orders of diffraction, the linearly time-varying phase shift is

$$\varphi_{sft}(t) = (\Delta\omega \mid_{m=1} - \Delta\omega \mid_{m=0}) t = 2\pi mvt/d. \tag{2.40}$$

If the ± 1 orders of diffraction are selected as the interfering waves, then the phase shift becomes to

$$\varphi_{sft}(t) = (\Delta\omega \mid_{m=1} - \Delta\omega \mid_{m=-1}) t = 4\pi mvt/d. \tag{2.41}$$

Higher orders are seldom adopted due to the limited diffraction efficiency. One of the interesting features in the sliding grating method is that the introduced frequency shift is independent from the operating wavelength. According to the grating equation, the wavelength, on the other hand, determines the diffraction angles, denoted by

$$d(\sin\theta_i - \sin\theta_m) = m\lambda, \tag{2.42}$$

where θ_i and θ_m are the angles of incidence and diffraction, respectively. For a normal incidence as shown in Figure 2.8, the angles are specified as $\theta_i = 0$ and $\theta_m = \theta$, respectively.

Acousto-Optic Modulator An acousto-optic modulator (AOM), also known as a Bragg cell, is an optical device which is based on the acousto-optic effect [63–65]. A ultrasonic grating is induced inside the acousto-optic crystal. In the application of phase shift, the AOM usually runs under the Bragg condition, as shown in Figure 2.9.
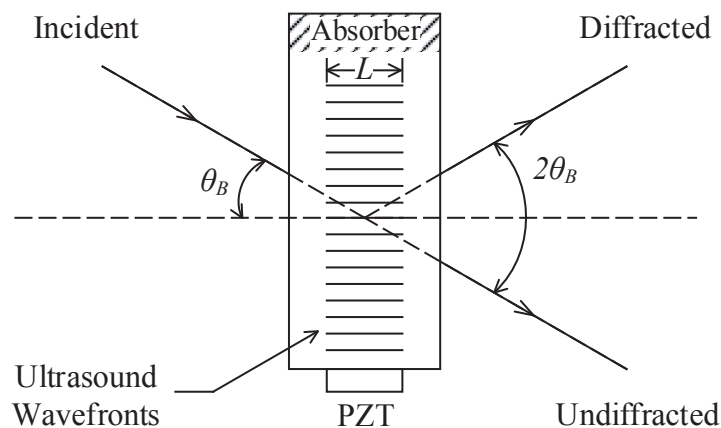

Figure 2.9: Phase shift induced by an AOM.

A radio frequency (RF) signal is fed to the PZT which is in contact with the acousto-optic crystal. As a result, a traveling acoustic field is established inside the crystal by the RF modulation at a frequency of f_{RF}. The acoustic wave propagates at the speed of sound, denoted by v_s. Consequently, the acoustic wavelength is calculated by [66]

$$\Lambda = 2\pi v_s / f_{RF}. \tag{2.43}$$

By using the acoustic wavelength, Λ, the aforementioned Bragg condition is stated by a particular incidence angle, denoted by

$$\sin\theta_B = \lambda/2\Lambda. \tag{2.44}$$

The particular angle, θ_B, is known as Bragg angle. By satisfying the Bragg condition at the Bragg angle, only one diffraction order is produced at the output end, while the other orders of diffraction vanish due to the destructive interference. Analogous to the sliding grating method [see Equations (2.40) and (2.41)], the frequency shift in the diffracted wave results in a linearly time-varying phase shift, given by

$$\varphi_{sft}(t) = 2\pi v_s t/\Lambda = f_{RF} \cdot t. \tag{2.45}$$

It is obvious that the RF signal determines the phase shift rate with respect to time. Commercial AOMs with operating frequency from tens to hundreds of megahertz are widely available in the market. However, such a frequency band is normally considered too high for array detectors. For a practical implementation in optical interferometric systems, two AOMs are normally used in parallel. It means that each of the interfering waves is modulated by an individual AOM. By a precision control of the two AOMs, it is readily to set the frequency difference within kilohertz or even lower. Thus, a scanning unit is avoided which in turn enables the usage of array detectors.

Rotating Polarizing Optics   An alternative method for introducing a frequency difference is based on rotating polarizing optics [67] such as phase retarder [68, 69] and polarizer [70, 71]. Various combinations and arrangements of the rotating polarizing optics are capable to introduce the frequency difference. In this demonstration, only one example is given in which the rotating polarizing optics is configured in front of the interferometric system, as shown in Figure 2.10.

The phase modulation unit is configured outside the interferometric system, which consists of a stationary polarizer, a rotating HWP, and a 45°-oriented quarter-wave plate (QWP). When a monochromatic wave incidents into the phase modulation with an arbitrary polarization, it is then converted to a linearly polarized wave by the polarizer. Assumed
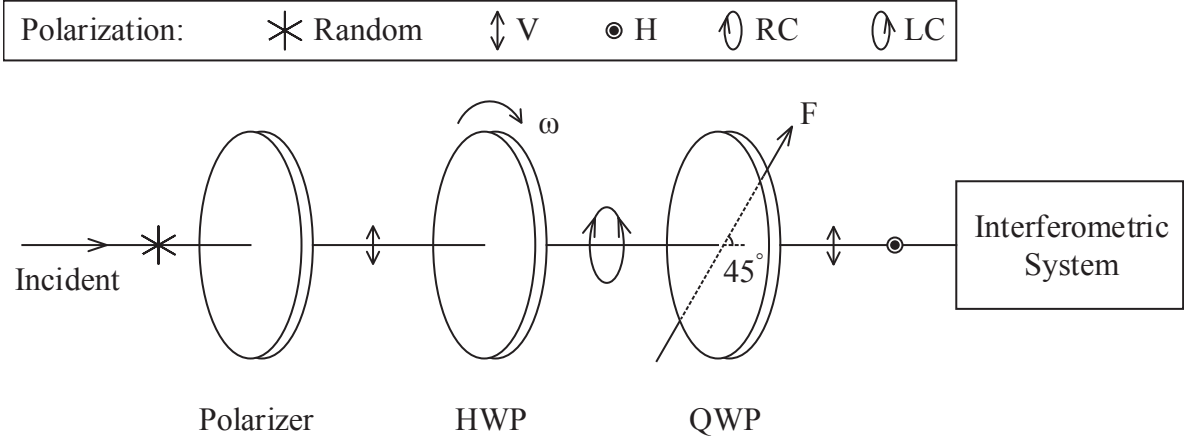
Figure 2.10: Phase shift induced by rotating optics.

for convenience, the linearly polarization is along the vertical direction, denoted by

$$V_p = \begin{bmatrix} 0 \\ 1 \end{bmatrix} \cdot \exp\left(-j\omega_0 t\right), \tag{2.46}$$

where ω_0 stands for the angular frequency of the input wave. The linearly polarized wave, V_p, passes through the rotating HWP and the 45°-oriented QWP, successively. The wave at the exit end of the phase modulation unit is calculated by

$$\begin{bmatrix} V_{hrz} \\ V_{vrt} \end{bmatrix} = \underbrace{\begin{bmatrix} 1 & j \\ j & 1 \end{bmatrix}}_{\text{QWP}} \underbrace{\begin{bmatrix} \cos 2\omega t & \sin 2\omega t \\ \sin 2\omega t & -\cos 2\omega t \end{bmatrix}}_{\text{rHWP}} V_p = \begin{bmatrix} -\exp\left(j2\omega t + \pi/2\right) \\ -\exp\left(-j2\omega t\right) \end{bmatrix} e^{-j\omega_0 t}, \tag{2.47}$$

where V_{hrz} and V_{vrt} represent the horizontal and the vertical polarization components of the emergent wave, respectively, and ω is the angular frequency of the rotating HWP. The magnitude of the wave vector is dropped in Equation (2.47) which in return only shows the phase-related items. Afterwards, the modulated wave enters the interferometric system, in which the two orthogonally polarized components, V_{hrz} and V_{vrt}, are separated by the polarizing beam splitter (not shown), e.g., the Wollaston prism. The linearly time-varying phase shift between the two components is then denoted by

$$\varphi_{sft}(t) = 4 \cdot \omega t. \tag{2.48}$$

The phase shift rate with respect to time is determined by the angular frequency of the rotating HWP. Normally, the demanded rotation is provided by a mechanical unit. As a matter of fact, the maximum of the upper limit of the angular frequency is in the order

of kilohertz. When the frequency goes up, the introduced phase shift becomes unreliable, because of the mechanical rotation.

Zeeman Laser   As its name indicated, the principle of the Zeeman laser is based on the Zeeman effect, which states that the spectral line splits into several components in the presence of a static magnetic field [20, 21]. Specifically, under the application of a longitudinal magnetic field, the spectrum of the output laser is split into two oppositely circular polarizations which are converted into orthogonal linear polarizations by a QWP [72], as shown in Figure 2.11.
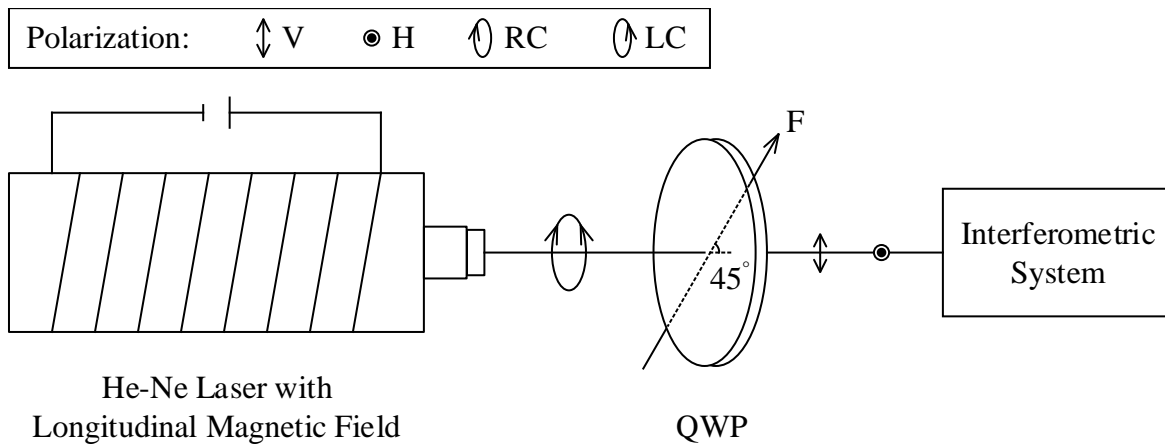

Figure 2.11: Phase shift provided by Zeeman laser.

Ideally, the spectral line of a He-Ne laser is 632.8 nm. The two spectral lines of the two split components are symmetrically distributed with respect to the 632.8 nm spectral line. According to the Zeeman effect [73, 74], the frequency difference between the two split components is

$$v_{rc} - v_{lc} = 2\Delta v = 2 \cdot \frac{g\mu_B H}{h}, \tag{2.49}$$

where $g = 1.3$ is the Landé g-factor, μ_B stands for the Bohr magneton, H represents the intensity of the applied magnetic field, and h denotes the Planck constant. Analogous to the description in the rotating polarizing optics, the conversion from circular to linear polarizations maintains the angular frequency of the corresponding waves. Consequently, the linearly time-varying phase shift is described by

$$\varphi_{sft}(t) = (v_{rc} - v_{lc}) \cdot t. \tag{2.50}$$

The typical frequency difference, which is introduced by Zeeman laser, is in the order of megahertz. So the Zeeman laser is normally used in point sensing or with scanning unit.

2.2.3 Summary

This section presents the commonly used phase-shifting devices and methods. The objective of this thesis (see Section 1.2) is drawn from the review of the representatives of the phase shifters.

Generally, the mechanical motion based phase shifters suffer from the noises resulting from translating, rotating, or expanding. Meanwhile, the maximum speed is restricted due to the inertia. Most of the acousto-optic or magneto-optic effects based phase shifters provide a phase shift in the order of megahertz, which is too fast for a camera to capture at least three images in a single cycle (see Subsection 2.1.1). Even though it is possible to capture such a fast varying interferogram in different cycles with a fixed delay, namely the stroboscope technique [75], a strong condition must be assumed that each cycle is completely the same. Regarding the location of the phase shifters, in certain interferometric systems, the phase is preferred to be shifted before entering the interferometer, because it is not necessary to consider the specific optical arrangement inside the interferometer. Not all of the phase shifters success in this task.

In terms of physical effect, the acousto-optic modulator belongs to the elasto-optic effect, and the Zeeman laser is based on the magneto-optic effect. As for the electro-optic effect based modulator, it is introduced in the following chapters, together with the proposed modulator in this thesis, to make a better comparison.

Chapter 3

Dual Transverse Electro-Optic Modulator

Recalling the scientific problem defined in Section 1.2, this chapter presents a solution to the phase-shifting issues. A polarization-controlled phase modulator is proposed to introduce a linearly time-varying phase shift in interferometric systems. The physical principle is based on the dual transverse electro-optic (DTEO) effect. The phase modulator operates under two orthogonally alternating electric fields without any mechanical motion units. The two interfering waves are phase shifted inside the phase modulator, simultaneously and locally, which means the phase modulator is capable to be applied in most polarizing interferometric systems. In terms of the operating frequency, a revised electro-optic coefficient is analyzed for a successful data collection by array detectors. The physical principle and the experimental verification of the proposed phase modulator are introduced in Sections 3.1 and 3.2, respectively.

3.1 Physical Principle

The DTEO phase modulator relies on an electro-optic crystal which has a trigonal crystal system. The unique symmetry of such a crystal system is that it has a three-fold rotation axis [76]. In terms of group theory, the trigonal crystal system is denoted by the $3m$ point group. In order to give a specific illustration, the lithium niobate (LN) (chemical formula: $LiNbO_3$), a representative crystal of the trigonal system, is selected in the analysis and experiment, but any crystal which has the same symmetry, e.g., lithium tantalate ($LiTaO_3$), succeeds in the proposed phase modulator.

3.1.1   Basics and Limitations

Generally, the electro-optic effect describes the phenomenon that the refractive index of the medium varies under the application of external electric field. The mathematics between the refractive index and the electric field is denoted by [77]

$$n = n_0 + aE + bE^2 + \cdots , \tag{3.1}$$

where E stands for the strength of the electric field, n_0 is the refractive index of the medium in the absence of the electric field ($E = 0$), a and b are the linear and the quadratic constants, respectively. Typically, the *Pockels* linear electro-optic effect is much more significant (many orders of magnitude larger) than the *Kerr* quadratic electro-optic effect. Even so, the variation in refractive index induced by the linear effect is so small that the changes are normally shown by interferometric methods. Throughout the present study, only the *Pockels* effect is considered and discussed, unless otherwise indicated.

According to the EM theory, the speed of light in the medium is [5]

$$c = c_0/n = (\mu\varepsilon)^{-1/2} \tag{3.2}$$

with

$$n^2 = \varepsilon/\varepsilon_0, \tag{3.3}$$

where c_0 stands for the speed of light in vacuum, μ and ε are the relative permeability and the relative permittivity in the medium, respectively, and ε_0 represents the vacuum permittivity. The relative permittivity is a symmetric second-order tensor which has $\varepsilon_{ij} = \varepsilon_{ji}$. In isotropic medium, the representation of the relative permittivity is a diagonal matrix in which all the diagonal elements have an identical value, namely $\varepsilon_{11} = \varepsilon_{22} = \varepsilon_{33} = \varepsilon$. The EM wave propagates in the isotropic medium at the same speed regardless of the direction. The situation becomes different in the case of an anisotropic medium. In an anisotropic medium, the refractive index is directional. As a result, the speed of light in an anisotropic medium is depended on the state of polarization and the propagation direction. This phenomenon is called birefringence. It is customary to use an index ellipsoid, termed as indicatrix, to describe the refractive index distribution according to the state of polarization and the propagation direction. In the principal axis system, the indicatrix is denoted by [78]

$$\begin{bmatrix} x \\ y \\ z \end{bmatrix}^T \begin{bmatrix} 1/n_1^2 & 0 & 0 \\ 0 & 1/n_2^2 & 0 \\ 0 & 0 & 1/n_3^2 \end{bmatrix} \begin{bmatrix} x \\ y \\ z \end{bmatrix} = 1, \tag{3.4}$$

where n_i is the refractive index along the corresponding principal axis which is known as principal refractive index. The shape and orientation of an indicatrix are determined by the symmetry of the crystal. Considering a uniaxial crystal, e.g., lithium niobate crystal, its indicatrix is an ellipsoid of revolution about the principal symmetry axis with $n_1 = n_2 = n_o$ and $n_3 = n_e$, where n_o and n_e represents the ordinary and the extraordinary refractive index, respectively. An illustration of such an indicatrix is shown in Figure 3.1.
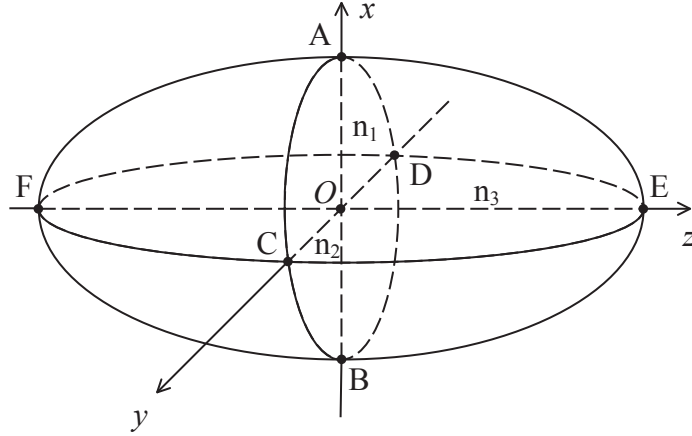

Figure 3.1: Indicatrix at the absence of an external field.

When the light propagates along the principal axis, the refractive index is readily found by investigating the indicatrix. For example, a monochromatic wave is considered propagating along the principal z-axis and linearly polarized along the x-axis. The refractive index for such a wave is found to n_1 in Figure 3.1. For a general case, the wave vector is assumed to be $\mathbf{OP} = (\cos\alpha_x, \cos\alpha_y, \cos\alpha_z)$, as shown in Figure 3.2.

The angles are defined as $\angle \mathrm{PO}x = \alpha_x$, $\angle \mathrm{PO}y = \alpha_y$, and $\angle \mathrm{PO}z = \alpha_z$. Considering a plane that contains the origin O and is perpendicular to the wave vector $\mathbf{OP}$, the intersection of this plane and the indicatrix is an ellipse in which the semi-major axis is OA and the semi minor axis is OB. The semi-major and the semi-minor axes indicate the two allowed polarization directions inside the crystal upon a propagation with the wave vector $\mathbf{OP}$, and their lengths denote the corresponding refractive indices, n_a and n_b, respectively.

Under the application of an external electric field, the shape, size, and orientation of the indicatrix are all changed, denoted by [79]

$$
\begin{bmatrix} x \\ y \\ z \end{bmatrix}^T
\begin{bmatrix} 1/n_{11}^2 & 1/n_{12}^2 & 1/n_{13}^2 \\ 1/n_{12}^2 & 1/n_{22}^2 & 1/n_{23}^2 \\ 1/n_{13}^2 & 1/n_{23}^2 & 1/n_{33}^2 \end{bmatrix}
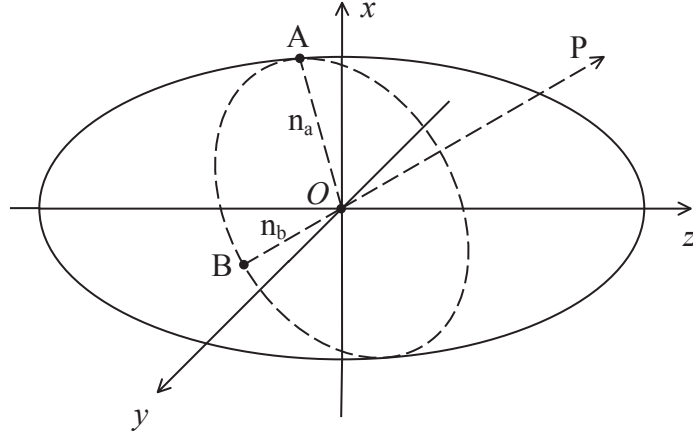\begin{bmatrix} x \\ y \\ z \end{bmatrix} = 1. \tag{3.5}
$$

Figure 3.2: Indicatrix for arbitrary propagation.

The cross terms in Equation (3.5) are induced by the external field, which indicates that the principal axes of the indicatrix are not coincident to the one without the external field. The mathematics between the refractive indices and the external electric field is

$$
\begin{cases}
\dfrac{1}{n_{11}^2} - \dfrac{1}{n_1^2} = \gamma_{11}E_x + \gamma_{12}E_y + \gamma_{13}E_z, \\[2mm]
\dfrac{1}{n_{22}^2} - \dfrac{2}{n_2^2} = \gamma_{21}E_x + \gamma_{22}E_y + \gamma_{23}E_z, \\[2mm]
\dfrac{1}{n_{33}^2} - \dfrac{1}{n_3^2} = \gamma_{31}E_x + \gamma_{32}E_y + \gamma_{33}E_z, \\[2mm]
\dfrac{1}{n_{23}^2} = \gamma_{41}E_x + \gamma_{42}E_y + \gamma_{43}E_z, \\[2mm]
\dfrac{1}{n_{13}^2} = \gamma_{51}E_x + \gamma_{52}E_y + \gamma_{53}E_z, \\[2mm]
\dfrac{1}{n_{12}^2} = \gamma_{61}E_x + \gamma_{62}E_y + \gamma_{63}E_z,
\end{cases}
\tag{3.6}
$$

where γ_{ij} $(i = 1,2,3, \cdots ,6, j = 1,2,3)$ is the electro-optic coefficient of the third-order tensor with 18 components. The number of components reduces due to certain kind of crystal symmetry. Considering the lithium niobate crystal [80], the non-zero components are $\gamma_{13} = \gamma_{23}$, $\gamma_{22} = -\gamma_{12} = -\gamma_{61}$, $\gamma_{42} = \gamma_{51}$, and γ_{33}. Equation (3.6) then becomes

$$
\begin{cases}
\dfrac{1}{n_{11}^2} = \dfrac{1}{n_o^2} - \gamma_{22}E_y + \gamma_{13}E_z, \quad & \dfrac{1}{n_{22}^2} = \dfrac{1}{n_o^2} + \gamma_{22}E_y + \gamma_{13}E_z, \\[2mm]
\dfrac{1}{n_{33}^2} = \dfrac{1}{n_e^2} + \gamma_{33}E_z, \quad & \dfrac{1}{n_{23}^2} = \gamma_{51}E_y, \\[2mm]
\dfrac{1}{n_{13}^2} = \gamma_{51}E_x, \quad & \dfrac{1}{n_{12}^2} = -\gamma_{22}E_x.
\end{cases}
\tag{3.7}
$$

Thus, the indicatrix of the lithium niobate crystal under the function of an external electric field is described by Equations (3.5) and (3.7) as

$$
\begin{bmatrix} x \\ y \\ z \end{bmatrix}^T
\begin{bmatrix}
1/n_o^2 - \gamma_{22}E_y + \gamma_{13}E_z & -\gamma_{22}E_x & \gamma_{51}E_x \\
-\gamma_{22}E_x & 1/n_o^2 + \gamma_{22}E_y + \gamma_{13}E_z & \gamma_{51}E_y \\
\gamma_{51}E_x & \gamma_{51}E_y & 1/n_e^2 + \gamma_{33}E_z
\end{bmatrix}
\begin{bmatrix} x \\ y \\ z \end{bmatrix} = 1. \quad (3.8)
$$

To show the usage of Equation (3.8), a transverse electro-optic modulation is first considered in which the wave propagates perpendicular to the applied electric field. Assuming that the wave is monochromatic and propagates along the z-axis, and the electric field only has an x-component, i.e., $E = E_x$ and $E_y = E_z = 0$. Under this assumption, the indicatrix described by Equation (3.8) degenerates into an ellipse with $z = 0$ [81], represented by

$$
\begin{bmatrix} x \\ y \end{bmatrix}^T
\begin{bmatrix}
1/n_o^2 & -\gamma_{22}E_x \\
-\gamma_{22}E_x & 1/n_o^2
\end{bmatrix}
\begin{bmatrix} x \\ y \end{bmatrix} = 1. \quad (3.9)
$$

By completing the square, Equation (3.9) is presented in the principal form, denoted by

$$
\begin{bmatrix} x' \\ y' \end{bmatrix}^T
\begin{bmatrix}
1/n_o^2 - \gamma_{22}E_x & 0 \\
0 & 1/n_o^2 + \gamma_{22}E_x
\end{bmatrix}
\begin{bmatrix} x' \\ y' \end{bmatrix} = 1, \quad (3.10)
$$

where x' and y' are the new principal axes called induced principal axes. The corresponding refractive indices are [81]

$$
\begin{aligned}
n_{x'} &= n_o \left(1 - n_o^2 \gamma_{22} E \right)^{-1/2} \approx n_o + \frac{1}{2} n_o^3 \gamma_{22} E, \\
n_{y'} &= n_o \left(1 + n_o^2 \gamma_{22} E \right)^{-1/2} \approx n_o - \frac{1}{2} n_o^3 \gamma_{22} E, \\
n_{z'} &= n_z = n_e,
\end{aligned} \quad (3.11)
$$

where the approximation is calculated by the binomial theorem. It is obvious that the induced principal z'-axis is identical to the intrinsic principal z-axis, whereas the induced principal x'- and y'-axes rotate at an angle of θ_r. To find out the rotation angle, θ_r, the principal axis transform from Equation (3.9) to (3.10) is shown in detail by a matrix notation of the ellipse, given by

$$
\begin{bmatrix} x' \\ y' \end{bmatrix}^T
\mathcal{R}^T \left(-\theta_r \right)
\begin{bmatrix}
1/n_o^2 & -\gamma_{22}E_x \\
-\gamma_{22}E_x & 1/n_o^2
\end{bmatrix}
\mathcal{R} \left(-\theta_r \right)
\begin{bmatrix} x' \\ y' \end{bmatrix} = 1 \quad (3.12)
$$

with

$$\begin{bmatrix} x^{'} \\ y^{'} \end{bmatrix} = \begin{bmatrix} \cos\theta_r & \sin\theta_r \\ -\sin\theta_r & \cos\theta_r \end{bmatrix} \begin{bmatrix} x \\ y \end{bmatrix} = \mathcal{R}\left(\theta_r\right) \begin{bmatrix} x \\ y \end{bmatrix}, \qquad (3.13)$$

where $\mathcal{R}$ represents the rotation matrix and $\left[\,\cdot\,\right]^T$ stands for the transpose operator. Equation (3.12) is then calculated as

$$\begin{bmatrix} x^{'} \\ y^{'} \end{bmatrix}^T \begin{bmatrix} 1/n_o^2 - \gamma_{22}E_x \cdot \sin 2\theta_r & -\gamma_{22}E_x \cdot \cos 2\theta_r \\ -\gamma_{22}E_x \cdot \cos 2\theta_r & 1/n_o^2 - \gamma_{22}E_x \cdot \sin 2\theta_r \end{bmatrix} \begin{bmatrix} x^{'} \\ y^{'} \end{bmatrix} = 1, \qquad (3.14)$$

where the cross term element, $-\gamma_{22}E_x \cdot \cos 2\theta_r$, is zero in the condition of a principal axis system. The rotation angle, θ_r, is determined by

$$-\gamma_{22}E_x \cdot \cos 2\theta_r = 0 \quad \Rightarrow \quad \theta_r = 45°. \qquad (3.15)$$

Figure 3.3 is a visualization of the deformation of the indicatrix from Equations (3.4) to (3.10). The drawing plane is $z = 0$, in which the rotation and the length change in the semi-major and the semi-minor axes are illustrated.
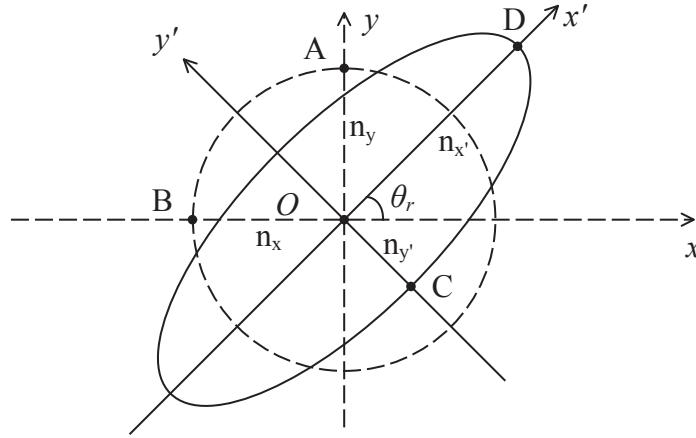

Figure 3.3: Deformed indicatrix.

Next, a monochromatic wave with a wavelength of λ is considered to demonstrate the phase delay in the transverse electro-optic effect. An orthonormal representation, which is based on the principal axes, is adopted in mathematics to describe the physical phenomenon. Inside the electro-optic material, the wave splits into two orthogonally polarized components, the polarization directions of which are aligned to the semi-major and the semi-minor axes, respectively. For the ease of illustration, the axial direction are called allowed polarization direction. Following the assumption that the wave propagates along the z-axis, and the electric field only has an x-component. The phase delay is described

by

$$\Delta\phi = \frac{2\pi}{\lambda} L \left| n_{x'} - n_{y'} \right| \approx \frac{2\pi}{\lambda} n_o^3 \gamma_{22} E_x L = \frac{2\pi}{\lambda} n_o^3 \gamma_{22} \frac{L}{d} u, \tag{3.16}$$

where L represents the geometric path length of the wave propagation in the electro-optic material, d stands for the thickness of the material along the electric field direction, and u is the applied voltage. The phase delay between the two allowed polarizations is proportional to the applied voltage, u. An important parameter of the electro-optic material is the half-wave voltage which is required to retard one allowed polarization by π in phase relative to the other. In the current demonstration, the half-wave voltage is denoted by [82]

$$u_\pi = \frac{\lambda}{2n_o^3 \gamma_{22}} \cdot \frac{d}{L}. \tag{3.17}$$

When the material is chosen, the half-wave voltage is determined by the length-thickness ratio, L/d. Although the longitudinal effect is beyond the scope of the present study, it is worth noting that the half-wave voltage is independent on the dimension of the material in that case.

As indicated previously, it is also capable to introduce a time-varying phase shift by the electro-optic effect, which is denoted by

$$\varphi_{sft}(t) = \pi \cdot \frac{u(t)}{u_\pi}, \tag{3.18}$$

where $u(t)$ is the applied voltage. Theoretically, the conventional electro-optic phase modulation is sufficient to introduce a desired phase shift between the two interfering waves by a linearly varying potential voltage. However, in practice, especially for the time-related measurement, it is not easy to generate a linear variation of the voltage which covers a large number of periods in terms of the cosine function [see Equation (2.21)]. Hence, for the phase modulation which is based on the electro-optic effect, a sinusoidally varying potential voltage is normally applied. In turn, the potential voltage of such a kind results in a time-varying intensity, in which the description involves the Bessel function, denoted by

$$I(\boldsymbol{\rho}, t) = I_0(\boldsymbol{\rho}) + I_0(\boldsymbol{\rho})\gamma(\boldsymbol{\rho}) \cdot \cos\left[\pi \cdot \frac{\beta \cdot \cos(\omega_u t)}{u_\pi}\right] \tag{3.19}$$

with

$$\cos\left[\pi \cdot \frac{\beta \cdot \cos(\omega_u t)}{u_\pi}\right] = J_0\left(\frac{\pi\beta}{u_\pi}\right) + 2\sum_{n=1}^{\infty} (-1)^n J_{2n}\left(\frac{\pi\beta}{u_\pi}\right) \cos(2n\omega_u t), \tag{3.20}$$

where J_i is the i-th Bessel function of the first kind, β and ω_u represent the amplitude

and the angular frequency of the sinusoidally varying potential voltage, respectively. As a matter of fact, the phase-shifted intensity described by Equation (3.19) brings difficulties in the phase retrieval.

3.1.2   Dual Transverse Electro-Optic Effect

In phase-shifting interferometric systems, a linearly time-varying phase shift is preferred, because the accompanied phase retrieval procedure is straightforward. In fact, the electro-optic phase/intensity modulators have already been studied for long. A number of commercial products are available, which are based on the physical principle, as introduced in Subsection 3.1.1. However, the aforesaid driving issue in conventional electro-optic modulators is considered as a barrier regarding the introduction of a linearly time-varying phase shift. As a result, it is not so common to apply an electro-optic modulator in phase-shifting applications.

In this section, being different from the conventional electro-optic phase modulation described above, a dual transverse electro-optic (DTEO) phase modulation is introduced and shown in Figure 3.4. As its name indicated, the DTEO modulation is defined by the
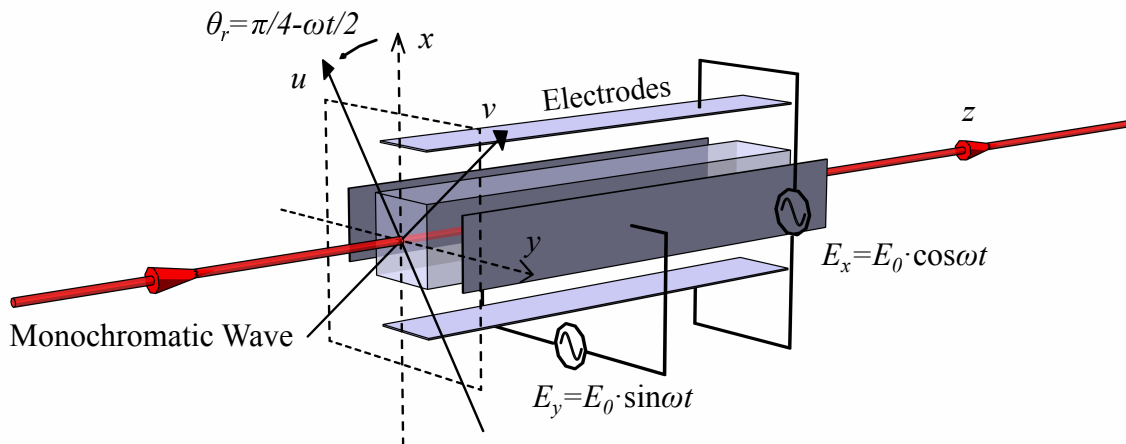

Figure 3.4: Configuration of dual transverse electro-optic effect.

configuration in which the electro-optic material operates in the transverse mode with two orthogonal electric fields. The orthogonality between the two electric fields expresses in both the space and the time domains. Considering a cubic bulk of crystal, in the space domain, the orientations of the two electric fields are perpendicular to each other. As shown in Figure 3.4, each rectangular surface of the crystal is provided with an electrode. The vertical and the horizontal electrode pairs generate the two mutually perpendicular electric fields. Note that Figure 3.4 is drawn in an exploded view. In practical implementations, the electrodes are attached to corresponding rectangular surfaces. In the time

domain, the expression of orthogonality is a $\pi/2$ phase delay between the two electric fields. The applied electric fields are denoted mathematically by

$$\begin{bmatrix} E_x \\ E_y \\ E_z \end{bmatrix} = E_0 \begin{bmatrix} \cos \omega t \\ \sin \omega t \\ 0 \end{bmatrix}, \quad (3.21)$$

where the z-directional electric field, E_z, is shown for a complete description of the electric field, even though $E_z = 0$; E_0 represents the amplitude, ω is the angular frequency, and t denotes the time parameter. The electric fields are applied to an electro-optic material. Assuming that the intrinsic principal axes of the material are aligned to the electric fields, E_x, E_y, and E_z, respectively, the indicatrix of the operating material is then calculated by substituting Equation (3.21) into Equations (3.5) and (3.6), denoted by

$$\begin{bmatrix} x \\ y \\ z \end{bmatrix}^T \begin{bmatrix} \frac{1}{n_x^2} + \gamma_{11}E_x + \gamma_{12}E_y & \gamma_{61}E_x + \gamma_{62}E_y & \gamma_{51}E_x + \gamma_{52}E_y \\ \gamma_{61}E_x + \gamma_{62}E_y & \frac{1}{n_y^2} + \gamma_{21}E_x + \gamma_{22}E_y & \gamma_{41}E_x + \gamma_{42}E_y \\ \gamma_{51}E_x + \gamma_{52}E_y & \gamma_{41}E_x + \gamma_{42}E_y & \frac{1}{n_z^2} + \gamma_{31}E_x + \gamma_{32}E_y \end{bmatrix} \begin{bmatrix} x \\ y \\ z \end{bmatrix} = 1, \quad (3.22)$$

where n_x, n_y, and n_z are the intrinsic principal refractive indices in the absence of the electric fields. Because the electro-optic material in the present study is the lithium niobate crystal, the symmetry of the crystal is directly considered for an ease of demonstration without a cumbersome discussion of the general case. Specifically, a z-cut lithium niobate crystal is oriented so that the three-fold axis of the crystal aligns to the z-axis. Recalling the crystal symmetry of point group $3m$, the useful electro-optic properties of the lithium niobate crystal are listed as

$$n_x = n_y = n_o,\ n_z = n_e,\ \boldsymbol{\gamma} = \begin{bmatrix} 0 & -\gamma_{22} & \gamma_{13} \\ 0 & \gamma_{22} & \gamma_{13} \\ 0 & 0 & \gamma_{33} \\ 0 & \gamma_{51} & 0 \\ \gamma_{51} & 0 & 0 \\ -\gamma_{22} & 0 & 0 \end{bmatrix}, \quad (3.23)$$

where $\boldsymbol{\gamma}$ is the 6×3 electro-optic tensor. By taking the symmetry of the operating crystal (Equation 3.23) into Equation (3.22), it yields

$$\begin{bmatrix} x \\ y \\ z \end{bmatrix}^T \begin{bmatrix} 1/n_o^2 - \gamma_{22}E_y & -\gamma_{22}E_x & \gamma_{51}E_x \\ -\gamma_{22}E_x & 1/n_o^2 + \gamma_{22}E_y & \gamma_{51}E_y \\ \gamma_{51}E_x & \gamma_{51}E_y & 1/n_e^2 \end{bmatrix} \begin{bmatrix} x \\ y \\ z \end{bmatrix} = 1. \quad (3.24)$$

Recalling Figure 3.4, in the transverse operating mode, the wave propagates inside the crystal along the z-axis. The change in the refractive index is governed by the intersection of the plane, $z = 0$, and the indicatrix denoted by Equation (3.24). The intersection is an ellipse which is a degeneration of the indicatrix at $z = 0$ [83], denoted by

$$\begin{bmatrix} x \\ y \end{bmatrix}^T \begin{bmatrix} 1/n_o^2 - \gamma_{22}E_y & -\gamma_{22}E_x \\ -\gamma_{22}E_x & 1/n_o^2 + \gamma_{22}E_y \end{bmatrix} \begin{bmatrix} x \\ y \end{bmatrix} = 1. \tag{3.25}$$

In order to show the induced refractive indices clearly, a rotation to the coordinate system is applied to rewrite Equation (3.25) in a principal form. Note that such a rotation does not change the physical phenomenon. The rotation of the coordinates is denoted by

$$\begin{bmatrix} u \\ v \end{bmatrix} = \begin{bmatrix} \cos\theta_r & \sin\theta_r \\ -\sin\theta_r & \cos\theta_r \end{bmatrix} \begin{bmatrix} x \\ y \end{bmatrix} = \mathcal{R}\left(\theta_r\right) \begin{bmatrix} x \\ y \end{bmatrix}, \tag{3.26}$$

where u and v are the coordinates in the principal axis system. Substituting u and v in Equation (3.25) yields

$$\begin{bmatrix} u \\ v \end{bmatrix}^T \begin{bmatrix} 1/n_u^2 & \text{cross term} \\ \text{cross term} & 1/n_v^2 \end{bmatrix} \begin{bmatrix} u \\ v \end{bmatrix} = 1, \tag{3.27}$$

where n_u and n_v are the refractive indices along the principal axes, respectively, and

$$1/n_u^2 = 1/n_o^2 - \gamma_{22}E_x \sin 2\theta_r - \gamma_{22}E_y \cos 2\theta_r, \tag{3.28a}$$

$$1/n_v^2 = 1/n_o^2 + \gamma_{22}E_x \sin 2\theta_r + \gamma_{22}E_y \cos 2\theta_r, \tag{3.28b}$$

$$\text{cross term} = -\gamma_{22}E_x \cos 2\theta_r + \gamma_{22}E_y \sin 2\theta_r. \tag{3.28c}$$

Obviously, in the principal axis system, the cross term is zero, so the rotation angle, θ_r, is thus related to the applied electric fields [see Equation (3.21)], denoted by

$$-\gamma_{22}E_x \cos 2\theta_r + \gamma_{22}E_y \sin 2\theta_r = 0 \quad \Rightarrow \quad \theta_r = \frac{\pi}{4} - \frac{\omega t}{2}, \tag{3.29}$$

where ω is the angular frequency of the applied electric fields defined in Equation (3.21). It is beneficial to give an insight into Equation (3.29), from which two points are drawn:

1. The rotation of the coordinate is time-dependent, and the angular frequency of the rotation is determined by the electric field, denoted by $\omega/2$.

2. The minus sign indicates that the rotation of the coordinate is in the opposite sense to that of the resultant electric field.

Though the ellipse rotates, the lengths of its semi-major and semi-minor axes stay unchanged. Or put it another way, the ellipse, which is used to describe the refractive index, maintains its shape but rotates around its center. In a dynamic view, the difference between the two principal refractive indices is constant in time. Here, the dynamic view has a meaning of a rotating reference coordinate system. By considering the longitudinal length of the operating crystal, namely along the direction of wave propagation (z-direction in Figure 3.4), the phase delay between the two principal axes is readily described by [83]

$$\Delta\varphi = \frac{2\pi L|n_u - n_v|}{\lambda} = \frac{2\sqrt{2}\pi L n_o}{\lambda}\sqrt{\frac{1 - \sin\beta}{\sin^2\beta}}, \tag{3.30}$$

where L is the longitudinal length of the crystal, λ is the operating wavelength, n_u and n_v are the principal refractive indices in the dynamic view [see Equation (3.28)], and

$$\beta = \arccos(n_o^2\gamma_{22}E_0). \tag{3.31}$$

Considering the phase delay between the two rotating principal axes, the effect of the operating crystal on the wave is established by the Jones matrix as

$$T_{crystal} = \mathcal{R}\left(\theta_r\right) \begin{bmatrix} \exp\left(j\frac{\Delta\varphi}{2}\right) & 0 \\ 0 & \exp\left(-j\frac{\Delta\varphi}{2}\right) \end{bmatrix} \mathcal{R}\left(-\theta_r\right). \tag{3.32}$$

Substituting the rotation matrix, $\mathcal{R}$, and the angle of rotation, θ_r, in Equation (3.32), the effect of the operating crystal is finally denoted by

$$T_{crystal} = \begin{bmatrix} \cos\left(\frac{\Delta\varphi}{2}\right) + j\sin\left(\frac{\Delta\varphi}{2}\right)\sin\left(\omega t\right) & j\sin\left(\frac{\Delta\varphi}{2}\right)\cos\left(\omega t\right) \\ j\sin\left(\frac{\Delta\varphi}{2}\right)\cos\left(\omega t\right) & \cos\left(\frac{\Delta\varphi}{2}\right) - j\sin\left(\frac{\Delta\varphi}{2}\right)\sin\left(\omega t\right) \end{bmatrix}. \tag{3.33}$$

By far, the behavior of a specific electro-optic material is described, in which the three-fold rotational symmetry is required. The two driving electric fields are mutually orthogonal in both time and space. It is equivalent to a rotating field applied in the plane perpendicular to the three-fold axis. The wave propagates along the three-fold axis, but it is noted that the transit time for the wave goes through the material is ignored in the discussion.

Next, the mathematics is deduced which describes the phase modulation by means of the DTEO effect, as shown in Figure 3.5. A linearly polarized input wave is assumed which has an arbitrary polarization angle, denoted by

$$V_0 = A \begin{bmatrix} \cos\alpha \\ \sin\alpha \end{bmatrix} \cdot \exp\left(-j\omega_0 t\right), \tag{3.34}$$
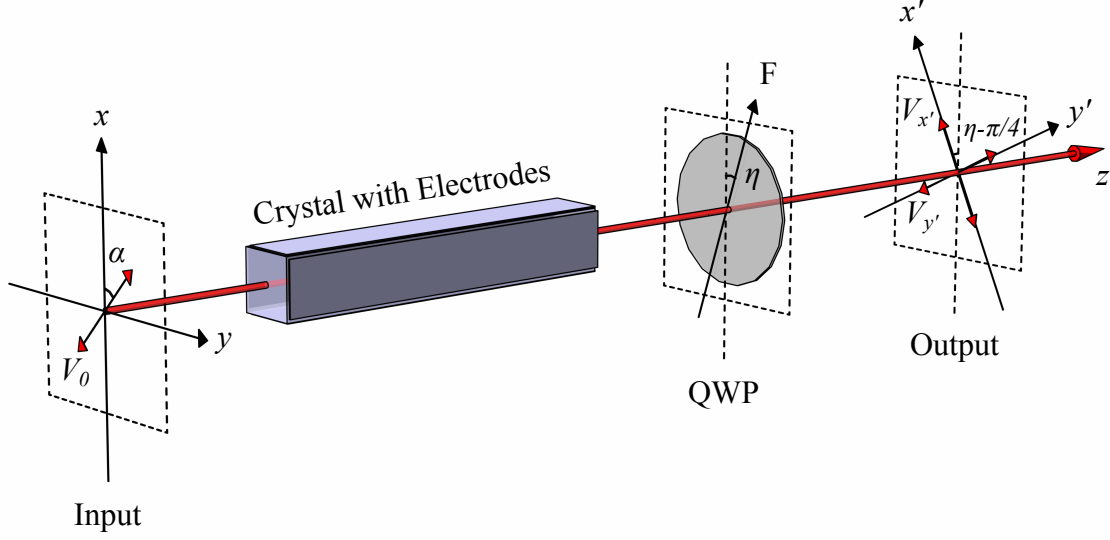
Figure 3.5: Principle and configuration of the DTEO phase modulator.

where A is the amplitude, α stands for the polarization angle (arbitrary) of the input wave with respect to the x-axis and ω_0 represents the angular frequency of the input wave. The wave is directed into the powered-up crystal. The DTEO modulation to the input wave is denoted by

$$V_{crystal} = T_{crystal} \cdot V_0, \tag{3.35}$$

where $V_{crystal}$ stands for the wave immediately after the crystal. By a proper split, Equation (3.35) is calculated as

$$
\begin{aligned}
V_{crystal} = & \frac{A}{2}\sin\left(\frac{\Delta\varphi}{2}\right)\Bigg\{\underbrace{\begin{bmatrix} 1 \\ j \end{bmatrix}\exp[-j\,(\omega_0 t-\omega t-\alpha)]}_{\text{right circular pol.}}+\underbrace{\begin{bmatrix} 1 \\ -j \end{bmatrix}\exp[-j\,(\omega_0 t+\omega t+\alpha-\pi)]}_{\text{left circular pol.}}\Bigg\} \\
& + \underbrace{A\cos\left(\frac{\Delta\varphi}{2}\right)\begin{bmatrix} \cos\alpha \\ \sin\alpha \end{bmatrix}\exp\left(-j\omega_0 t\right)}_{\text{linear pol.}},
\end{aligned}
\tag{3.36}
$$

where an identity is used for the split, denoted by

$$
\begin{bmatrix} \cos\chi \\ \sin\chi \end{bmatrix} = \frac{1}{2}\left\{\begin{bmatrix} 1 \\ j \end{bmatrix}\exp\left(-j\chi\right) + \begin{bmatrix} 1 \\ -j \end{bmatrix}\exp\left(j\chi\right)\right\}. \tag{3.37}
$$

As indicated in Equation (3.36), the modulated wave possesses three components, namely two orthogonal circular polarizations with a frequency difference and a linear polarization which is identical to the input wave. The linearly time-varying phase shift is found between the orthogonal polarizations. By a careful selection of the operating parameters, the linear polarization in Equation (3.36) vanishes, which is done by considering the half-wave voltage of the operating crystal. The half-wave voltage refers to the voltage required for inducing a phase change of π for the light going through the crystal. Specifically, when the half-wave voltage, u_π, is applied, the electric field strength is denoted by $E_0 = u_\pi/d$, where d represents the distance between the electrode pair, namely the side length of the square section of the crystal. As a result, the phase delay, $\Delta\varphi$, between the two principal axes is π, and further, the wave immediately after the crystal is denoted by

$$V_{crystal}\mid_{u_\pi} = \underbrace{\frac{A}{2}\begin{bmatrix} 1 \\ j \end{bmatrix}\exp\left[-j\left(\omega_0 t - \omega t - \alpha\right)\right]}_{\text{right circular pol.}} + \underbrace{\frac{A}{2}\begin{bmatrix} 1 \\ -j \end{bmatrix}\exp\left[-j\left(\omega_0 t + \omega t + \alpha - \pi\right)\right]}_{\text{left circular pol.}}. \quad (3.38)$$

For the convenience of further applications, a QWP is used to convert the two circular polarizations into linear ones. The conversion is done by directing the modulated beam [see Equation (3.38)] passes through the QWP, the fast axis of which is oriented at an arbitrary angle, η, with respect to the x-axis. The output is calculated as

$$\begin{bmatrix} V_{y'} \\ V_{x'} \end{bmatrix} = \mathcal{R}(\eta - \frac{\pi}{4}) \cdot \underbrace{\frac{\sqrt{2}}{2}\begin{bmatrix} 1 + j\cos 2\eta & j\sin 2\eta \\ j\sin 2\eta & 1 - j\cos 2\eta \end{bmatrix}}_{\text{QWP}} \cdot V_{crystal}\mid_{u_\pi}$$

$$= \frac{\sqrt{2}A}{2}\begin{bmatrix} \exp\left[-j\left(\omega_0 t + \omega t + \alpha + \eta - \frac{5\pi}{4}\right)\right] \\ \exp\left[-j\left(\omega_0 t - \omega t - \alpha - \eta - \frac{\pi}{4}\right)\right] \end{bmatrix}, \quad (3.39)$$

where the coordinate is rotated by an angle of $\eta - \pi/4$, represented by $\mathcal{R}(\eta - \frac{\pi}{4})$, $V_{x'}$ and $V_{y'}$ are the two components along the axes in the rotated coordinate, respectively. Note that the coordinate transformation does not influence the physical features of the modulation, but changes the mathematical representation into an easy-reading form. Under the application of a polarizer which is oriented at ψ with respect to the x-axis, the two interfering waves are denoted by

$$\widetilde{U}_1(t) = \frac{\sqrt{2}A \cdot \sin\psi}{2} \cdot \exp\left[-j\left(\omega_0 t + \omega t + \alpha + \eta - \frac{5\pi}{4}\right)\right], \quad (3.40a)$$

$$\widetilde{U}_2(t) = \frac{\sqrt{2}A \cdot \cos\psi}{2} \cdot \exp\left[-j\left(\omega_0 t - \omega t - \alpha - \eta - \frac{\pi}{4}\right)\right]. \quad (3.40b)$$

In Equation (3.40), the spatial coordinates are dropped for clarity, because here the phase is only discussed and modulated along the time. Consequently, the linearly time-varying phase shift between the interfering waves is given by

$$\varphi_{sft}(t) = 2\omega t + 2\alpha + 2\eta - \pi, \tag{3.41}$$

where the time-dependent item is only related to the angular frequency, ω, of the applied electric fields. A linearly time-varying phase shift is then brought around by such a scheme. The phase shift is carried by two orthogonally linear polarizations which gives flexibility for further applications in interferometric systems, because such a phase shift scheme does not rely on the followed-up optical configurations.

In the description above, the orientations of the input polarization (α), the QWP (η), and the polarizer (ψ) are all arbitrary. The purpose is to demonstrate that the present phase modulator is insensitive to orientation errors. This feature results from the circular symmetry of modulation. There is no preferred direction in the phase modulator. The time-varying interferometric intensity of a general form resulting from the two waves in Equation (3.40) is calculated by

$$I(t) = \left[\widetilde{U}_1(t) + \widetilde{U}_2(t)\right] \cdot \left[\widetilde{U}_1(t) + \widetilde{U}_2(t)\right]^* = \frac{A^2}{2} + \frac{A^2}{2}\sin 2\psi \cos(2\omega t + 2\alpha + 2\eta - \pi). \tag{3.42}$$

It is apparent that the orientations do not determine the time-varying phase shift. Once an interferometric system is built up, the parameters, α, η, ψ, are fixed and the phase item, $2\alpha + 2\eta - \pi$, is regarded as the initial phase in the system. In fact, the initial phase is determined by the choice of the describing coordinates. The time-varying phase shift is only related to the applied electric fields. On the other hand, the orientation, ψ, of the polarizer has a substantive impact on the interference, but it only determines the visibility of the interferometric pattern. Therefore, the proposed phase shifter is immune to the orientation errors of the optical components and insensitive to the input polarization direction.

The parameters of a particular configuration are summarized which give a good efficiency to the phase modulator, listed as follows:

1. The operating electro-optic material is a cubic bulk of crystal with a three-fold rotational symmetry. The intersection, which is perpendicular to the three-fold axis, is a square.

2. In the transverse operation mode, the wave propagates along the three-fold axis. The resultant electric field is constant in strength, while rotating in the square section around the three-fold axis.

3. The two orthogonal electric fields are driven by the half-wave voltage, which is determined by the length-thickness ratio and the electro-optic property of the crystal in use, as well as the operating wavelength.

4. The QWP is 45° oriented with respect to the x-axis.

Recalling Equations (3.33) and the Jones matrix of the QWP [84], the phase modulator under such a configuration is denoted by

$$T_{PM} = T_{QWP} \mid_{45°} \cdot T_{crystal} \mid_{u_\pi} = \frac{\sqrt{2}}{2} \begin{bmatrix} -\cos\omega t + j\sin\omega t & j\cos\omega t + \sin\omega t \\ j\cos\omega t - \sin\omega t & -\cos\omega t - j\sin\omega t \end{bmatrix}. \quad (3.43)$$

3.2 Experimental Verification

After the description of the physical principle in the DTEO phase modulator, this section demonstrates the feasibility of the modulator by a series of experiments. Some practical issues regarding the implementations are shown and discussed. Particularly, a revised electro-optics coefficient is considered to run the modulator in an operating frequency which satisfies the frame rate of commercial array detectors.

3.2.1 Revised Electro-Optic Coefficient

This subsection first clarifies the difference between the electro-optic effect and the *Pockels* effect, because sometimes the concepts are confusable. Then, a proper choice of the electro-optic coefficient is presented. The electro-optic effect discussed above is all about the refractive index variation resulting directly from the applied electric field, which is known as the primary effect. Being rigorous, there is actually another contributory factor besides the primary effect, namely the secondary effect [78]. The secondary effect takes its function by an indirect impact on the refractive index. The observed phenomenon from an electro-optic effect is the sum of the primary and the secondary effects. Figure 3.6 shows a full description of the origins which lead to a variation in the refractive index under the application of an external electric field.

It is found that there are two routes linking the applied electric field and the variation in the refractive index. The applied electric field gives rise to the changes in both the strain and the refractive index of the crystal. The direct primary effect shows the pure influence on the refractive index from the applied electric field. Such an influence strictly defines the *Pockels* effect, whereas the electro-optic covers both the *Pockels* effect and the secondary effect. Considering the secondary effect, the field-induced strain further alters the refractive index through the photo-elastic effect. For the purpose of clarity, it is
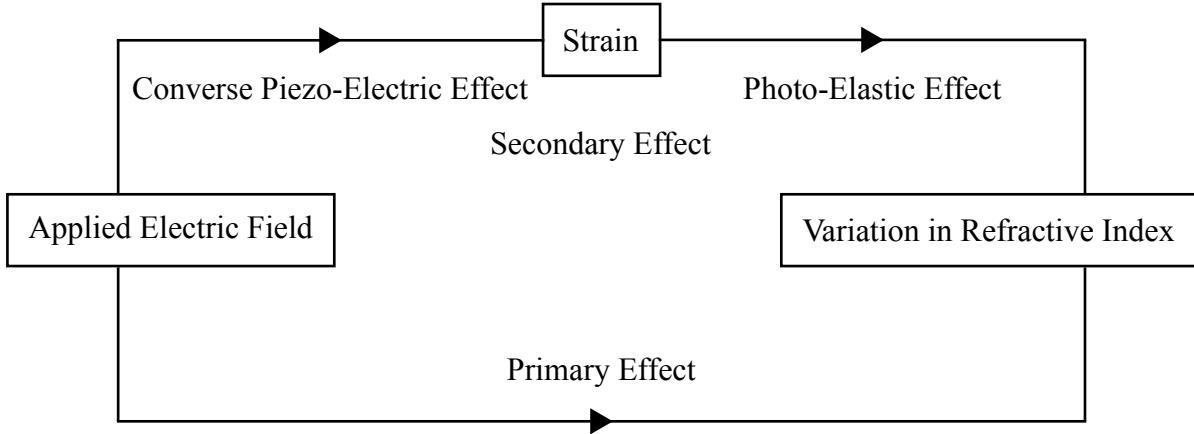
Figure 3.6: Primary and secondary effects from external field to refractive index.

customary to denote the electro-optic coefficient by the *Pockels* effect. The contribution from the secondary effect to the refractive index is normally announced separately when considered.

For a high frequency practice (normally above 1 kHz), the secondary effect is conventionally dropped when describing the field-induced refractive index, because, compared to the primary effect, the consequential variation in the refractive index is not sufficiently significant. The reason is that, at high frequencies, the inertia of the crystal prevents it from being strained macroscopically. However, this is not the case when the crystal undergoes a static or slowly varying field. At low frequencies, the secondary effect has a competitive magnitude in the observed phenomenon with respect to the primary effect. When the secondary effect is taken into account, the effective electro-optic effect is calculated by [79]

$$\Delta \frac{1}{n_i^2} = \sum_{j=1}^{3} \sum_{k=1}^{6} p_{ik} d_{jk} E_j + \sum_{j=1}^{3} r_{ij} E_j, \tag{3.44}$$

where i runs from 1 to 6 (in contracted notation), p is the elasto-optic coefficient, d is the piezo-electric coefficient, r is the *Pockels* electro-optic coefficient. The effective electro-optic coefficient is then denoted by

$$\gamma_{ij} = \sum_{k=1}^{6} p_{ik} d_{jk} + r_{ij}. \tag{3.45}$$

At high frequencies the first term on the right-hand side of Equation 3.44 is zero. However, at low frequencies the elasto-optic effects contribute additionally to the changes of the refractive indices. In the present study, all the electro-optic coefficient refers to the effective one, which includes the contribution from the secondary effect, because the phase

modulator aims to be coupled with array detectors.

3.2.2 Experiments and Results

To verify its feasibility, the DTEO modulator is configured in an experimental setup. The laser beam leaving the DTEO modulator is directed into a Michelson interferometer, as shown in Figure 3.7. Before the linearly polarized laser beam enters the phase modulator,
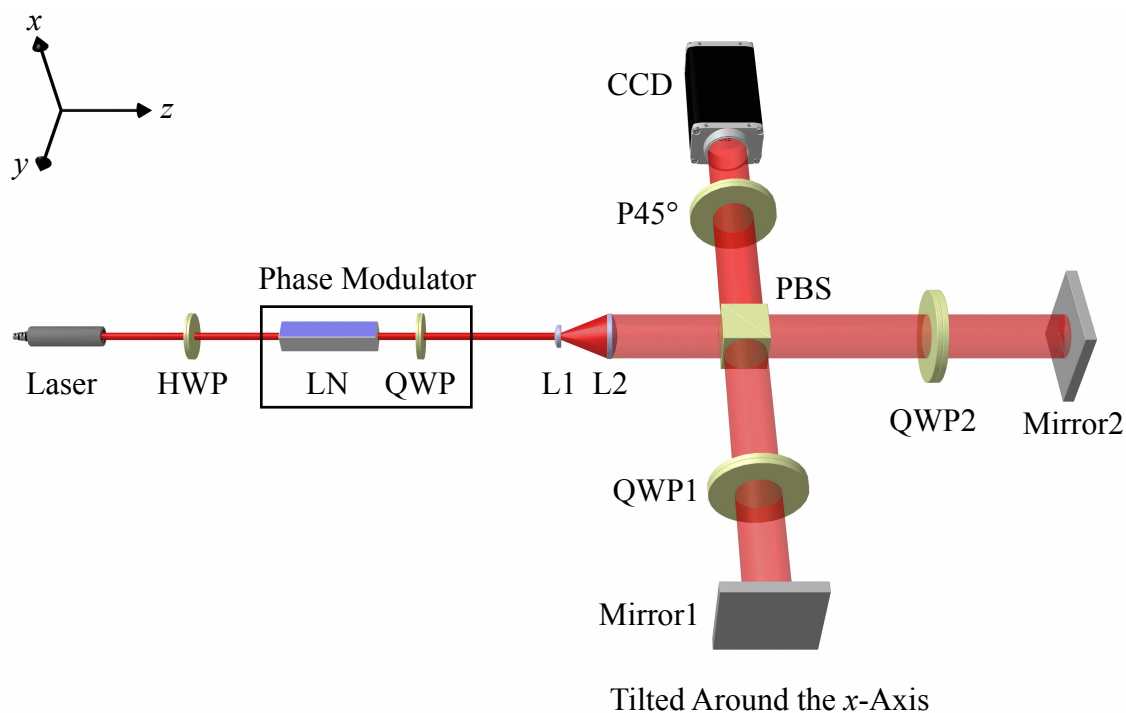

Figure 3.7: Experimental configuration of the optical setup. Mirror1 is tilted around the x-axis to form a vertical distribution of the interferometric fringes at the CCD plane.

the HWP orients the polarization, assumed for convenience, along the x-axis. The laser beam is then modified by the DTEO phase modulator. Lenses L1 and L2 are configured as a Keplerian telescope, which is used to collimate the modulated laser beam. Thanks to the orthogonality of the two modulated components [$V_{x'}$ and $V_{y'}$ in Equation (3.39)], a polarizing beam splitter (PBS) is readily exploited to split the two components spatially and direct them into corresponding interferometric arms. Ideally, there is only a single optical frequency in one arm, but this is not always true in practical implementations. The reason is that 1) the degree of polarization (DOP) can hardly achieve 100% in the real world, and 2) the misalignments also result in a frequency mix in a single arm. Hence, to increase the frequency purity in each arm, the best practice is to orient the fast axis of the QWP at 45° with respect to the optic axis of the PBS, say the x-axis. Between the PBS

and each mirror, a QWP is inserted to switch the polarization in corresponding arm to its orthogonal state. Consequently, when the beams in each arm returning to the PBS, the previously transmitted beam is reflected and vice versa. A 45° oriented polarizer helps to force the x- and y-polarized beams into interference at the CCD plane. It is noted that all the polarization conversions in the present configuration do not change the time-varying phase shift between the two interfering beams, but indeed the initial phase changes along with the conversion, which does not influence the time-varying phase shift.

The experimental setup is configured as shown in Figure 3.7, and all systematic settings, as well as parameters of the devices in operation, are listed below:

- Source: Helium-Neon laser, Carl Zeiss Jena HNA 188-2

    - Power: 50 mW;

    - Wavelength: 632.8 nm;

    - Polarization extinction ratio: 1000:1;

- Electro-optic material: LN crystal

    - Intrinsic refractive index: $n_0 = 2.2863$ @ 632.8 nm;

    - Effective electro-optic coefficient: $\gamma_{22} = 7 \times 10^{-12}$ m/V, < 1kHz;

    - Dimension: 5 $(d) \times 5$ $(d) \times 30$ (L) mm^3;

    - Orientation: z-cut, three-fold axis // 30 mm direction;

    - Electrode: four electrodes cover the four rectangular surfaces, respectively;

- Power supply: two channels for one pair of opposite electrodes each

    - Output waveform: sinusoid;

    - Phase delay between channels: $\pi/2$;

    - Angular frequency: $\omega = 34\pi$ rad/s;

    - Amplitude: half-wave voltage $u_\pi = d \cdot E_0$=349 V;

- Optics:

    - Wave plates: polymer true zero-order retarders;

    - Lenses: L1 and L2 with focal lengths of 5 mm and 40 mm, respectively;

- Array detector: CCD camera, Basler piA640-210gm

    - Frame rate: 136 fps;

- Region of interest: 384 px × 512 px;

- Pixel size: 7.4 μm × 7.4 μm;

- Pixel bit depth: 8 bits;

The acquisition time is eight seconds. Considering the operating frame rate of the camera, a set of 1088 frames is recorded during the experiment in time sequence. Figure 3.8 shows four interferograms with an identical time interval between successive frames. The
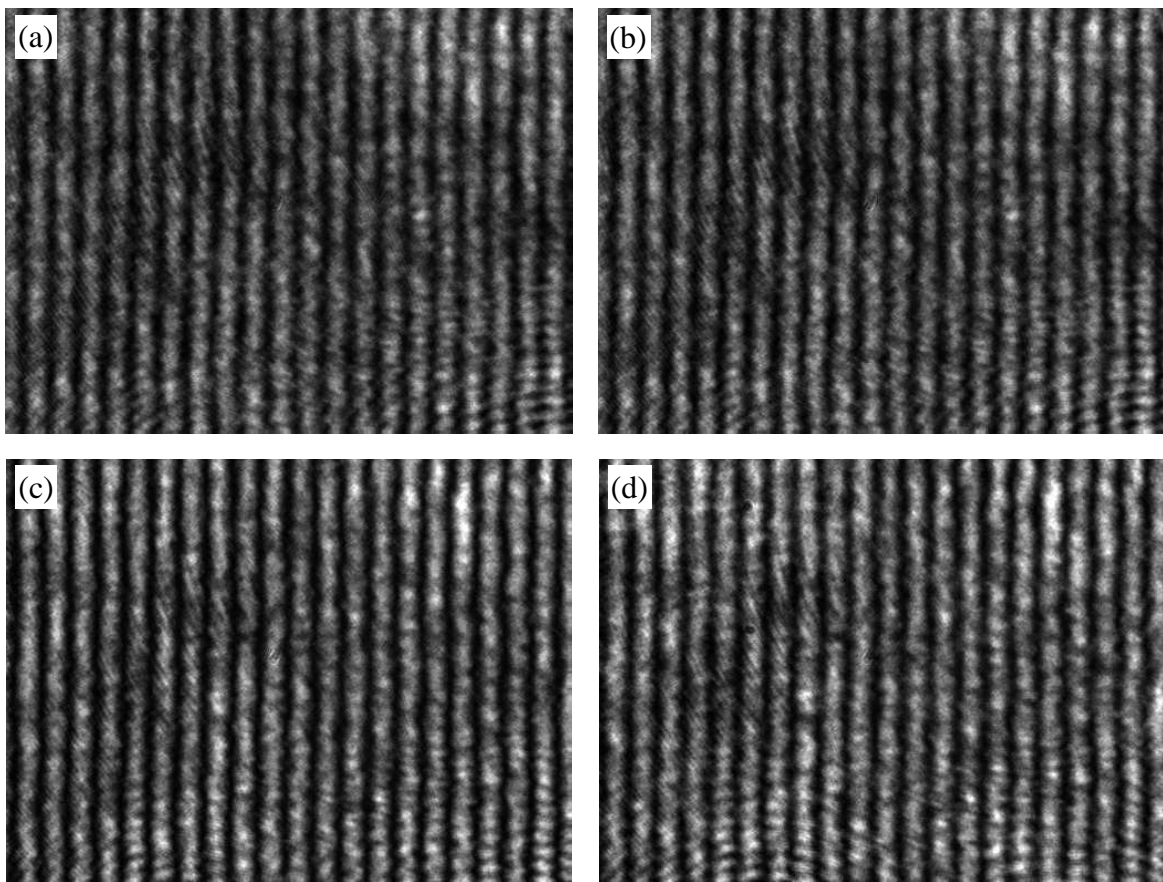

Figure 3.8: Four captured interferograms. From (a) to (d), the frame indices of the interferograms are 7, 8, 9, and 10, respectively.

vertically oriented fringes are the expression of the interference between the two mutually tilted wavefronts. A fringe movement is observed, which results from the shifting phase in the two interferometric arms. Without losing generality, each of the captured interferograms is represented by the gray levels in its 192nd row of pixels for further analysis, as shown in Figure 3.9.
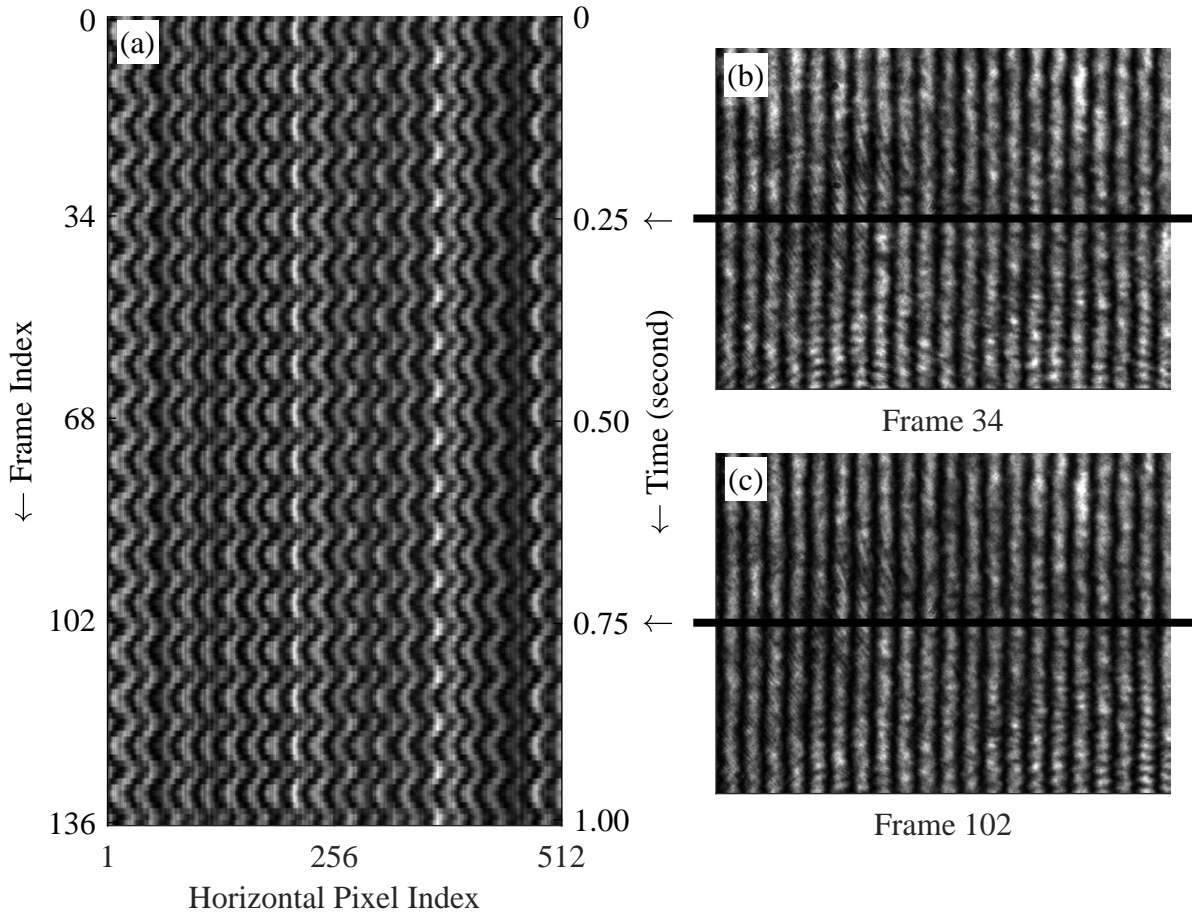
Figure 3.9: Temporal intensity evolution history.

Figure 3.9(a) shows the temporal evolution history of the interferometric intensity, in which the 192nd row of pixels in each frame is extracted and stacked together from the top to the bottom in time sequence. For example, the rows of pixels, which are marked by the black solid lines, in Frames 34 and 102 [see Figure 3.9(b) and (c)] are extracted and placed in Figure 3.9(a) at the points in time, 0.25 s and 0.75 s, respectively. It is noted that Figure 3.9(a) only involves the data collected within one second for efficiency. A periodic intensity evolution is observed over time, which indicates the linearly time-varying phase shift.

To give a quantitative investigation of the phase shift, the temporal frequency of the intensity evolution history is examined. The pixel located at (137,424) is selected as an example. The temporal intensity evolution history of the selected pixel is presented in Figure 3.10(a), and its corresponding temporal frequency is shown in Figure 3.10(b). Once again, for a detailed illustration, Figure 3.10(a) only covers the first 136 sampling points in time sequence, which corresponds to an acquisition time of one second. The
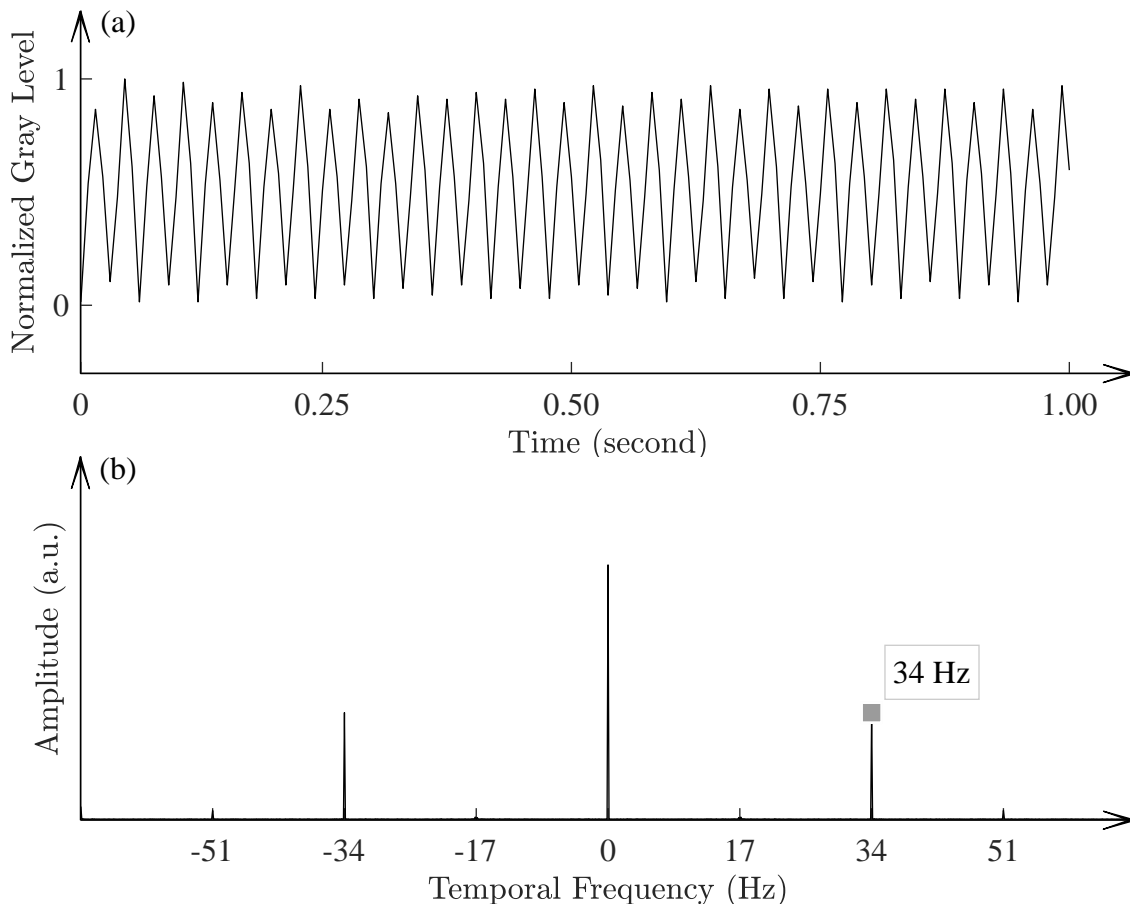
Figure 3.10: Investigation of the temporal intensity at a single pixel. (a) Intensity along time and (b) Fourier spectrum of (a).

temporal frequency shown in Figure 3.10(b) accounts for all the 1088 sampling points. As shown in the temporal frequency spectrum, the DC component is contributed from the background intensity. The labeled frequency, which is located exactly at 34 Hz, confirms the linearly time varying phase shift.

It is worth noting that besides the DC and the 34 Hz components, there is occasionally a non-dominating component which occupies the frequency of 17 Hz [too small to be noticed in Figure 3.10(b)]. This component results from the manufacturing error in the DTEO modulator. Specifically, referring to Equation (3.36), when the driving voltage is not perfectly equal to the half-wave voltage of the operating crystal, a linear polarization appears with an identical optical frequency to the input wave. The QWP converts the linear polarization into a circular polarization. The 17 Hz component is a result of the interference between the said circular polarization of the original frequency and the up/down shifted frequencies. In implementations, the non-dominating 17 Hz component, as well as other noise, is readily removed by the frequency domain filtering.

In the experimental setup, the laser beam is expected to pass through the center of the square cross section of the powered-up crystal. Inside the crystal, the electric field is uniform along the center line in the three-fold axis direction. In the off-axis area, there is a cross talk between the x- and y- components of the electric field. Certain distortion is found in the resultant field and the distortion reaches its maximum at the edge of the crystal. A spatial filter or a pinhole give rise to an enhanced quality of the phase shift by eliminating the undesired portion of beam.

3.3   Summary

This chapter presents the dual transverse electro-optic (DTEO) phase modulator. The description starts from the basics of conventional electro-optic modulator, and its difficulty of introducing a linearly time-varying phase shift is identified. In such a background, the physical principle of the DTEO phase modulator is demonstrated in detail. The functionality of the DTEO phase modulator relies on the three-fold rotational symmetry of an electro-optic crystal. An useful physical property of the DTEO effect is concluded, which lays the fundamental of the DTEO phase modulator. The property is that the principal axes of the operating crystal is rotating along time, but the phase delay between the principal axes is constant. The phase delay is deduced in terms of the applied voltage. The half-wave voltage is indicated by finding the phase delay of π. The Jones matrix of the DTEO phase modulator is presented in the general and a preferred configurations, respectively [see Equations (3.33) and (3.43)].

The feasibility of the DTEO phase modulator is verified in an experimental setup. The lithium niobate crystal is selected as the operating material, because it possesses the $3m$ point group symmetry. The Michelson interferometer is used to have the experimental demonstration, in which the DTEO phase modulator is configured before the beam splitting. The difference between the electro-optic effect and the *Pockels* effect is clarified to have a proper choice of the electro-optic coefficient. By investigating the temporal intensity evolution history of the interferograms, as well as its corresponding temporal frequency spectrum, the feasibility and functionality of the DTEO phase modulator is confirmed.

Chapter 4

Temporal ESPI Based on DTEO Modulator

Electronic speckle pattern interferometry (ESPI) is an important member in the family of interferometric systems. It is customary to consider the electronic speckle pattern interferometry (ESPI) as a successor of the conventional speckle interferometry in which the interference pattern is recorded by exposing a photosensitive film. To visualize the speckle interference, which is generated by conventional speckle interferometers, a post-treatment is normally involved, namely the film development. The film development brings difficulties to the quantitative analysis of the interference and reduces the time resolution of the measurement greatly. In the year 1970, Leendertz [85] brought a television camera to a conventional speckle interferometer, which now has gained wide acceptance to be recognized as the emergence of ESPI. In ESPI systems, the photosensitive films are replaced by electronic devices, e.g., digital cameras. For further data interpretation, it is possible to transfer the captured speckle interference pattern to a host computer, which gives various possibilities to potential applications of ESPI. In this case, the ESPI is sometimes specified as digital speckle pattern interferometry (DSPI), in which the speckle data is processed in the host computer instead of hardware.

In practice, the ESPI technique plays a vital role in the field of non-destructive testing. The crowned features of the ESPI technique include: full-field investigation, non-destructive evaluation, high accuracy, and the potential possibility of real-time measurement. A good number of literatures have been published regarding the ESPI technique [86–88]. The more promising aspect is that the technique is no longer limited in optical laboratory. Rather, quite a lot of industrial applications rely on the ESPI technique. The application area covers auto and aerospace industry, manufacturing, civil engineering, material science, biology, etc. Various ESPI systems have been developed for differ-

ent scenarios, e.g., out-of-plane/in-plane deformation measurement [89–91], shape/profile modeling [92], and surface roughness evaluation [93, 94].

In this chapter, a temporal ESPI system is proposed which is based on the DTEO phase modulator. The proposed system possess the ability of measuring the in-plane rotation in real time. The direction of rotation is obtained together with the angle quantity. The relationship between the rotation and the phase change distribution is established for a successful evaluation of the target. Thanks to the DTEO phase modulator, dynamic measurements are accomplished and the results are given in real time.

4.1   Basics in ESPI

The ESPI systems are normally used for the investigation of optically rough surfaces, the average height variation of which is larger than a quarter of the operating wavelength. Under coherent illumination, the reflection from the rough surface develops speckle patterns at the observation plane. The speckle phenomenon was a trouble for scientists and researchers in the field of holography, which makes the hologram granular [95]. Efforts have been put in suppressing speckle until it was recognized that the speckles actually carry the information about the surface under investigation. Soon after, the speckles are taken as a kind of tool in optical metrology. The associate speckle-related techniques are developed, such as speckle photography, speckle interferometry, and speckle statistics. In this section, the basics in ESPI is introduced.

4.1.1   Working Principle

A Michelson interferometer is considered to illustrate the working principle of ESPI, as shown in Figure 4.1. The coherent illumination is provided by a laser. The emission beam is collimated by the collimation lens and then enters the beam splitter. The beam scattered from the rough surface (object) is termed as the object beam and the one reflected from the mirror as the reference beam. The two beams are recombined at the beam splitter and the interference speckle pattern is imaged to the detector array. At the detector array, the imaged interference speckle pattern is called the subjective speckle pattern. For a successful access to the fringes or phase, it is necessary to control the minimum diameter of the speckles, so that the speckle pattern is fully resolved by the detector array. Considering a single speckle pattern that is formed by an imaging system, e.g., a lens, the minimum diameter of the speckles is determined by the effective numerical aperture (N.A.) of the imaging lens [96], denoted by

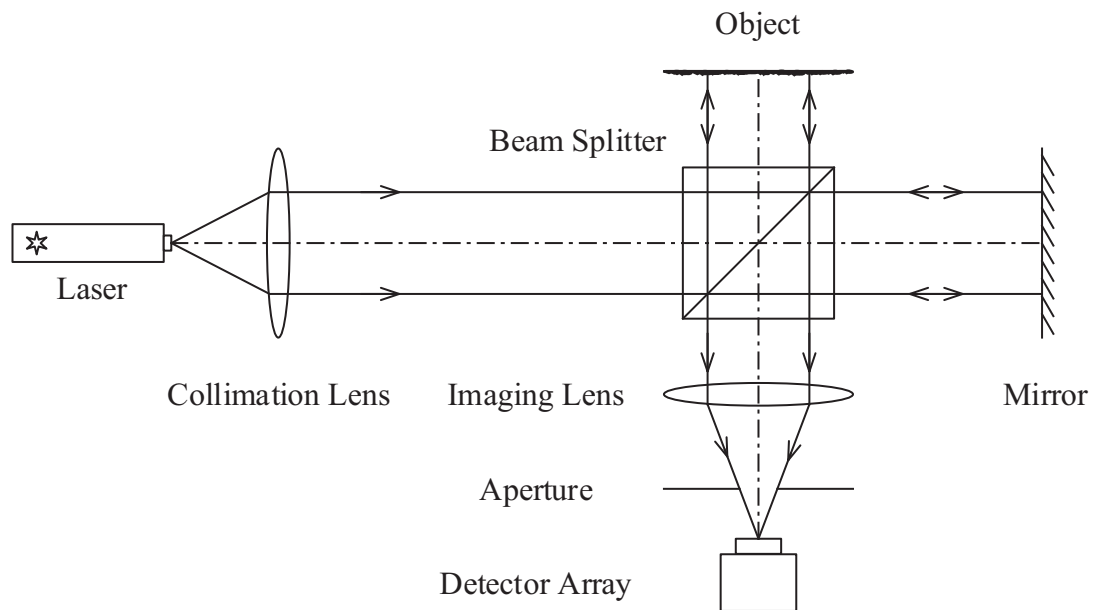$$\sigma \approx 0.6\lambda/\text{N.A.}, \tag{4.1}$$

Figure 4.1: ESPI system based on a Michelson interferometer.

where λ is the illumination wavelength. When it comes to a speckle interferometer, the speckles in the interferogram result from the coherent superposition of the speckle field and a uniform field, namely the reference field. The superposition of the reference field has an impact on the size of the individual speckles. Specifically, the minimum diameter of the speckles is doubled [96]. Hence, a simple way to control the speckle size in the speckle interferometer is realized by placing an aperture in front of the imaging lens. Through the change in the opening size of the aperture, it is straightforward to control the speckle size by the effective N.A. To measure a quantity by using ESPI systems, a basic scheme is the double exposure method [97]. An interference speckle pattern is first captured of the object in one state. Then, the object undergoes certain load or change and the other interference speckle pattern is recorded. The correlation fringes of these two speckle pattern reveals the measured quantity.

4.1.2 Correlation Fringes

Conventionally, the correlation fringes are accessible through three approaches, namely the addition, the subtraction, and the convolution methods. Each method has its own features in the presentation of the correlation fringes. To demonstrate these methods, it is helpful to mathematically denote the intensity of the interferogram:

$$I_{before}\left(\boldsymbol{\rho}\right) = A_1^2\left(\boldsymbol{\rho}\right) + A_2^2\left(\boldsymbol{\rho}\right) + 2A_1\left(\boldsymbol{\rho}\right)A_2\left(\boldsymbol{\rho}\right)\cos\left[\phi_s\left(\boldsymbol{\rho}\right)\right], \qquad (4.2)$$

where $A_{1,2}$ represents the amplitude of the reference wave and the object wave, respectively, ϕ_s stands for the phase of the interference speckle pattern. Similarly, after the object undergoes a deformation, for example, the intensity becomes

$$I_{after}\left(\boldsymbol{\rho}\right) = A_1^2\left(\boldsymbol{\rho}\right) + A_2^2\left(\boldsymbol{\rho}\right) + 2A_1\left(\boldsymbol{\rho}\right) A_2\left(\boldsymbol{\rho}\right)\cos\left[\phi_s\left(\boldsymbol{\rho}\right) + \phi\left(\boldsymbol{\rho}\right)\right],\qquad(4.3)$$

where ϕ denotes the phase change induced by the deformation.

Addition Mode   As its name indicates, the addition mode of the correlation fringes is calculated by the absolute sum of the intensities of the double exposure [98], denoted by

$$\begin{aligned}I_{cf}\left(\boldsymbol{\rho}\right) &= \left|I_{before}\left(\boldsymbol{\rho}\right) + I_{after}\left(\boldsymbol{\rho}\right)\right| \\ &=2\left(A_1^2 + A_2^2\right) + 4A_1 A_2\left|\cos\left[\phi_s\left(\boldsymbol{\rho}\right) + \frac{\phi\left(\boldsymbol{\rho}\right)}{2}\right]\cos\left[\frac{\phi\left(\boldsymbol{\rho}\right)}{2}\right]\right|,\end{aligned}\qquad(4.4)$$

where the sum-to-product identities are used for the calculation. The correlation fringes are revealed by the term $\cos\left[\phi\left(\boldsymbol{\rho}\right)/2\right]$, which shows the measured quantity, such as the displacement. It is noted that the correlation fringes are superimposed by the multiplicative noise, presented by the random-speckle granular term $\cos\left[\phi_s\left(\boldsymbol{\rho}\right) + \phi\left(\boldsymbol{\rho}\right)/2\right]$. When the correlation fringes are illustrated by the addition mode, special care is required to enhance the contrast, because the term $2\left(A_1^2 + A_2^2\right)$ gives rise to the stationary noise and reduces the visibility of the correlation fringes.

Subtraction Mode   Analogous to the addition mode, the subtraction mode of the correlation fringes is obtained by the subtraction operation of the double exposure [99]. By subtracting Equations (4.2) and (4.3) and getting the absolute value, it yields

$$\begin{aligned}I_{cf}\left(\boldsymbol{\rho}\right) &= \left|I_{before}\left(\boldsymbol{\rho}\right) - I_{after}\left(\boldsymbol{\rho}\right)\right| \\ &=4A_1 A_2\left|\sin\left[\phi_s\left(\boldsymbol{\rho}\right) + \frac{\phi\left(\boldsymbol{\rho}\right)}{2}\right]\sin\left[\frac{\phi\left(\boldsymbol{\rho}\right)}{2}\right]\right|.\end{aligned}\qquad(4.5)$$

Each item in Equation (4.5) has the same definition to Equation (4.4). A significant distinction is that the background intensity is canceled out due to the subtraction operation. Ideally, the minimum intensity of the correlation fringes is zero without being bothered by the background intensity, or the DC component. As a result, the contrast of the correlation fringes is greatly enhanced. On the other hand, the gray level of the correlation fringes obtained by the subtraction mode is limited to a narrow range. It is concluded that the subtraction mode has an enhanced contrast and a relatively low gray level of the correlation fringes. Due to the exist of the multiplicative noise, the subtraction mode also suffers from the random-speckle granular pattern. For either the addition

or the subtraction mode, a post-treatment of filtering is conventionally applied to reduce the multiplicative noise.

Convolution Mode The convolution mode is also known as the correlation mode which is based on the knowledge of the speckle statistics. A sliding window is involved to calculate the correlation coefficient within the desired area [100]. The correlation fringes are presented by the value of the correlation coefficients. The advantage of the convolution mode is that it removes the multiplicative noise in the correlation fringes. By reviewing the two previous modes, it is known that when there is no difference between the two captured speckle interference patterns, the intensity of the correlation fringes reaches its minimum. Dark fringes are presented in this case. In other words, the two intensity measures are correlated to the greatest extent at the position where dark fringes appears. On the contrary, the two measures show lowest correlation at bright fringes. Hence, it is possible to reveal the fringes by the correlation coefficients. Recalling Equations (4.2) and (4.3), the correlation coefficient is calculated by the covariance [101], denoted by

$$C\left(\boldsymbol{\rho}\right) = \frac{\left\langle \left(I_{before} - \langle I_{before}\rangle_{m\times n}\right)\left(I_{after} - \langle I_{after}\rangle_{m\times n}\right)\right\rangle_{m\times n}}{\left[\left\langle\left(I_{before} - \langle I_{before}\rangle_{m\times n}\right)^2\right\rangle_{m\times n}\right]^{1/2}\left[\left\langle\left(I_{after} - \langle I_{after}\rangle_{m\times n}\right)^2\right\rangle_{m\times n}\right]^{1/2}}, \quad (4.6)$$

where the angle brackets represent the ensemble average, $m \times n$ stands for the size of the window in pixel. It is assumed that 1) the intensity within the investigation window is constant during the loading event, and 2) the average intensities in both interferometric arms are identical. Mathematically, the assumptions are denoted by

$$\langle I_{before}\rangle = \langle I_{after}\rangle = 2\langle I_{arm}\rangle_{m\times n}, \quad (4.7)$$

where I_{arm} represents the intensity in a single arm. Another useful identity is based on the condition that the size of the investigation window is sufficiently large. Under this condition, the identity is denoted by

$$\langle \cos \phi_s\rangle_{m\times n} = \langle \cos\left(\phi_s + \phi\right)\rangle_{m\times n} = 0. \quad (4.8)$$

Substituting Equations (4.7) and (4.8) into Equation (4.6) yields

$$C\left(\boldsymbol{\rho}\right) = \frac{2\langle I_{arm}\rangle_{m\times n}^2 + 2\langle I_{arm}\rangle_{m\times n}^2 \cos\phi}{4\langle I_{arm}\rangle_{m\times n}^2} = \frac{1}{2}\left(\cos\phi + 1\right). \quad (4.9)$$

It is shown in Eq. (4.9) that when the correlation fringes are calculated by the convolution method, the distribution of the correlation coefficient directly characterizes the fringes.

More importantly, the presented fringe pattern is free of the multiplicative noise which is resulted from the speckles.

To sum up, any one of the three calculation modes is effective in extracting the correlation fringes from the randomly distributed speckle patterns. Considering the quality of the correlation fringes, the convolution mode removes the multiplicative noise and has an improved contrast at the same time. Both of the addition and the subtraction modes suffer from the multiplicative noise. Specifically, the subtraction mode cancels out the background intensity to enhance the contrast but at a cost of a narrowed gray level, whereas the correlation fringes revealed by the addition mode appears in a relatively low contrast due to the exist of the background intensity. In terms of the complexity of the algorithms, the convolution mode requires much more resources compared to the other two modes. It means that it demands longer time for the calculation to render a correlation fringe map. The convolution and the subtraction modes are frequently used in practice. When the first priority is the quality of the correlation fringe map, the convolution mode is preferred. In the case that there is a requirement of time resolution, the subtraction mode is a better choice.

4.1.3   Sensitivity Vector

The aforementioned correlation fringes are the contours of constant displacement which is projected along the sensitivity vector [102]. The optical geometry determines the sensitivity vector. Specifically, the illumination and the observation directions play an important role in the determination of the sensitivity vector [103]. The discussion in this subsection is restricted to the optically rough surface, because when it comes to specular surfaces, the analysis follows the law of reflection.

Considering a general case as shown in Figure 4.2, the point source, which is located at Point O, illuminates an optically rough target. An object point, P, on the investigating surface is selected for the demonstration. Its corresponding displaced point is marked as P$'$. The observer is placed at point S. The illumination wave vectors are denoted by $\vec{k}_1$ and $\vec{k}_3$ for P and P$'$, respectively. Correspondingly, the observation wave vectors are $\vec{k}_2$ and $\vec{k}_4$. The wave vectors are all unit vectors and the magnitude is defined by

$$|\vec{k}| = \frac{2\pi}{\lambda}. \tag{4.10}$$

The quantity of interests is the phase difference between the two paths. The individual phases of the optical path length (OPL) before and after the target displacement are
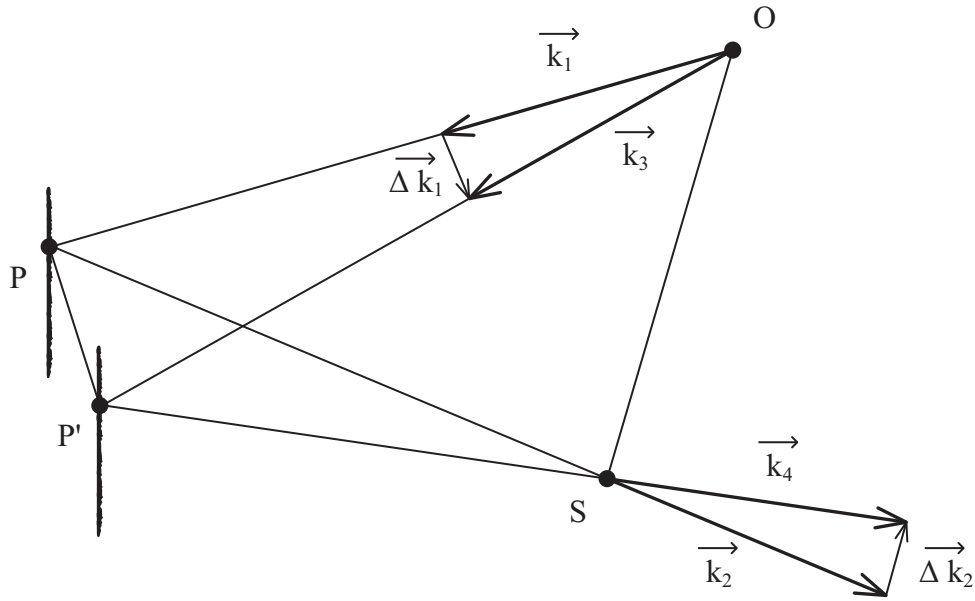
Figure 4.2: Sensitivity vector.

denoted by

$$\phi_1 = \vec{k}_1 \cdot \overrightarrow{OP} + \vec{k}_2 \cdot \left(\overrightarrow{OS} - \overrightarrow{OP} \right) + \phi_0, \tag{4.11a}$$

$$\phi_2 = \vec{k}_3 \cdot \overrightarrow{OP'} + \vec{k}_4 \cdot \left(\overrightarrow{OS} - \overrightarrow{OP'} \right) + \phi_0, \tag{4.11b}$$

where ϕ_0 stands for the initial phase. The phase difference which results from the displacement is then calculated by

$$\Delta\phi = \phi_2 - \phi_1 = \left(\vec{k}_1 - \vec{k}_2 \right) \cdot \overrightarrow{PP'} + \Delta\vec{k}_1 \cdot \overrightarrow{OP'} + \Delta\vec{k}_2 \cdot \overrightarrow{P'S}, \tag{4.12}$$

with

$$\begin{aligned} \vec{k}_3 &= \vec{k}_1 + \Delta\vec{k}_1, \\ \vec{k}_4 &= \vec{k}_2 + \Delta\vec{k}_2. \end{aligned} \tag{4.13}$$

The ESPI systems are in function until the speckles reach the decorrelation state, which in turn defines the measuring range of the displacement. In practical scenarios, to run the system in full function, the distances illustrated in Figure 4.2 have a relationship

regarding their magnitudes, denoted by

$$|\overrightarrow{OP}| \approx |\overrightarrow{OP'}| \gg |\overrightarrow{PP'}| = |\overrightarrow{OP'} - \overrightarrow{OP}|. \qquad (4.14)$$

Under such an approximation, the difference vectors, $\Delta \vec{k}_1$ and $\Delta \vec{k}_2$, are considered perpendicular to the displaced illumination vector, $\overrightarrow{OP'}$, and the displaced observation vector, $\overrightarrow{P'S}$, respectively. Considering the fact that the dot product between orthogonal vectors is zero, Equation 4.12 is reduced to

$$\Delta \phi = \left(\vec{k}_1 - \vec{k}_2 \right) \cdot \overrightarrow{PP'} = \vec{k}_s \cdot \overrightarrow{PP'}, \qquad (4.15)$$

where $\vec{k}_s$ is the sensitivity vector. Equation (4.15) shows that 1) the sensitivity vector is determined by the illumination vector and the observation vector, and 2) the measured phase at the observation point is a projection of the displacement-induced phase onto the sensitivity vector. Depending on the specific optical geometry, a distinct sensitivity vector is built for dedicated systems. Pure out-of-plane and pure in-plane sensitivities are the two typical and basic configurations for phase measurements in ESPI systems. When multiple illumination/observation vectors are given, the ESPI system is with the potential of possessing multiple sensitivity vectors [90, 104], which gives the possibility of carrying out multi-quantity simultaneous measurements in a single system.

4.2   Optical Configuration

As is demonstrated previously, phase-shifting techniques are frequently used to quantitatively determine the phase in ESPI systems. The own features of an individual phase modulator or method have a strong influence on the performance of the ESPI system. Among various aspects in system evaluation or assessment, the time resolution is sometimes a crucial parameter, especially when the real-time measurement for dynamic target is involved. In this section, the optical configuration of a temporal ESPI system is described which is based on the DTEO phase modulator. It is capable for the proposed system to carry out real-time measurement, which is designed for in-plane rotation evaluation. The rotation-induced phase is retrieved from the temporal carrier which is provided by the DTEO modulator. The mathematical model which gives the relationship between the phase change distribution and the in-plane rotation angle is deduced. At the same time, the direction of the rotation is determined as well by considering the sign of the derivative of the phase change map.

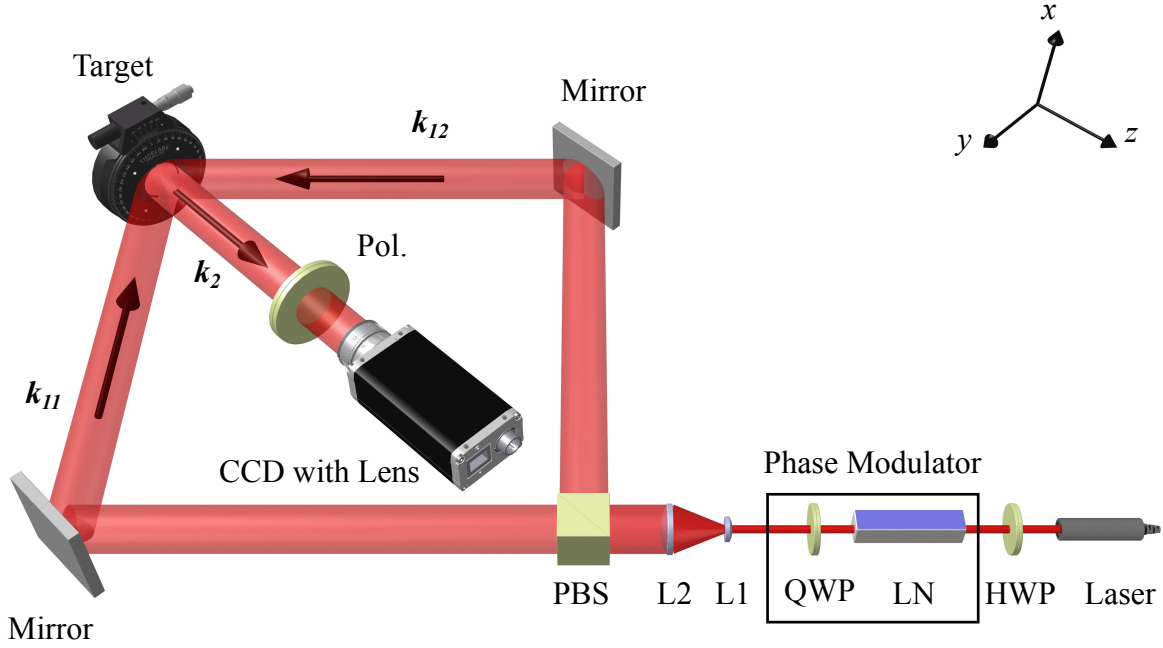Figure 4.3 illustrates the proposed temporal ESPI system. The laser beam emitted from

Figure 4.3: Optical configuration of the temporal ESPI.

the coherent source passes through the HWP and the DTEO modulator, successively. The HWP orients the input polarization to a desired direction, along the y-axis for example. In order to give a straightforward demonstration, the coordinate system is established with respect to the target surface, the positive z-axis of which points out of the surface perpendicularly. The modulated laser beam is expanded and collimated by the lens set, L1 and L2. Then a PBS is used to separate and direct the orthogonal polarizations into different interferometric arms. The two separated beams are directed by the two mirrors and illuminate the target surface symmetrically. A 45°-oriented polarizer is placed between the target surface and the camera lens. Finally, the two orthogonal polarizations interfere with each other at the image plane, in which the CCD camera is placed to capture the interferograms.

Referring to the coordinate system in Figure 4.3, the laser beam is assumed to propagate in the yz-plane ($x = 0$) and the sensitivity vector of the proposed system is described by

$$\vec{k}_s(\vec{u},\vec{v},\vec{w}) = (\vec{k}_{11} - \vec{k}_2) - (\vec{k}_{12} - \vec{k}_2) = \frac{4\pi}{\lambda} \sin\theta \cdot \vec{v}, \qquad (4.16)$$

where $\vec{u}$, $\vec{v}$, and $\vec{w}$ are the unit vectors along the x-, y-, and z-axes, respectively, θ represents the illumination angle with respect to the normal of the surface, $\vec{k}_{11,12}$ stands for

the illumination wave vector, and $\vec{k}_2$ is the observation wave vector. In the configuration, the absolute values of the illumination angle for both incident beams are identical, which means the target is illuminated by the two incident beams symmetrically. Based on the description of the sensitivity vector, the measured phase change distribution is related to the in-plane displacement, which results from the in-plane rotation, denoted by

$$\Delta\varphi(x,y) = \vec{k}_s(\vec{u},\vec{v},\vec{w}) \cdot (\Delta l_x \vec{u} + \Delta l_y \vec{v} + \Delta l_z \vec{w}) = \frac{4\pi}{\lambda} \sin\theta \cdot \Delta l_y(x,y), \qquad (4.17)$$

where Δl_x , Δl_y, and Δl_z are the corresponding axial components of the displacement vector. It is shown that, in the current configuration and discussion, the system is sensitive to the y-direction only.

Next, the relationship between the phase change distribution and the in-plane rotation is established, as depicted in Figure 4.4. For an ease of demonstration, the in-plane
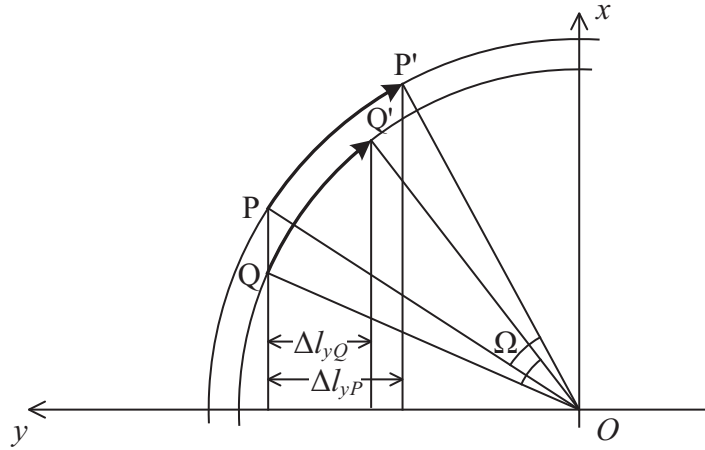

Figure 4.4: Mathematical model of the relationship between the phase change distribution and the in-plane rotation.

rotation is assumed clockwise. An arbitrary point on the surface is selected, marked by Point P, in the following discussion. The center of the in-plane rotation is labeled as the origin O of the coordinate system. When the rotation occurs with an angle of Ω, Point $P(x_1,y_1)$ moves to Point $P'(x_2,y_2)$. Analogously, another point is considered which has the same $y-$coordinate to Point P, labeled by Point $Q(x_3,y_1)$. Its corresponding displaced location is marked by $Q'(x_4,y_4)$. To specify the direction, x_1 is assumed larger than x_3 in value, denoted by $x_1 > x_3$. The elementary geometry is used to calculate the two lateral displacements for Points P and Q along the sensitivity vector. The mathematics gives

$$\begin{aligned} \Delta l_{yP} = y_2 - y_1 = y_1 \cos\Omega \mp x_1 \sin\Omega - y_1, \\ \Delta l_{yQ} = y_4 - y_1 = y_1 \cos\Omega \mp x_3 \sin\Omega - y_1, \end{aligned} \qquad (4.18)$$

where the minus-plus sign applies for the clockwise (-) and the counterclockwise (+) rotations, respectively. The directional derivative of the phase change distribution is calculated by

$$\frac{\partial \Delta l_y(x,y)}{\partial x} = \frac{\Delta l_{yP} - \Delta l_{xQ}}{x_1 - x_3} = \mp \sin \Omega. \tag{4.19}$$

Equation (4.19) is deduced under the condition of rigid body, where the rotation angle is identical across the entire surface. Particularly, the partial derivative is calculated along the direction which is perpendicular to the sensitivity vector. In the current demonstration, the calculation is conducted along the x-axis. By substituting Equations (4.17) and (4.18) into Equation (4.19), it yields

$$\Omega = \arcsin[\mp \frac{\lambda}{4\pi \sin \theta} \cdot \frac{\partial \Delta \varphi(x,y)}{\partial x}], \tag{4.20}$$

where the phase change distribution, $\Delta \varphi(x,y)$, is obtained from the temporal carrier by the Fourier transform method. The minus-plus sign applies for the clockwise and the counterclockwise rotations, respectively. Finally, Equation (4.20) connects the in-plane rotation to the measured phase change distribution.

4.3 Experiments and Results

The experiments are carried out to demonstrate the feasibility of the proposed temporal ESPI system, which in particular emphasizes the time-dependent measurement for dynamic target. The in-plane rotation of the optically rough surface is provided by a PZT. Specifically, the surface is attached to a micro-mechanical rotation stage which is driven by the PZT. The system is configured as illustrated in Figure 4.3. For an efficient demonstration, the parameters regarding the light source and the DTEO modulator are not repeated here, referring the list in Subsection 3.2.2 for information. The dedicated parameters for the temporal ESPI system are given below:

- PZT-driven mechanical rotation stage
    - Resolution: 0.1 arcsec;
    - Direction: counterclockwise viewing from the camera;
- Lenses:
    - Focal length: L1 = -6 mm; L2 = 75 mm;
- Camera lens: Nikon AF-S DX Zoom-Nikkor
    - Focal length: 17-55 mm;

- Array detector: CCD camera, Basler piA640-210gm

  - Frame rate: 272 fps;

  - Region of interest: 300 px × 300 px;

  - Pixel size: 7.4 μm × 7.4 μm;

  - Pixel bit depth: 8 bits;

  - Acquisition time: 5 seconds;

Under this configuration, 1360 frames are captured within five seconds. The captured frames are analyzed pixelwise. For an individual pixel, its intensity evolution history possesses 1360 values in length, and the phase of this investigating pixel is evaluated from intensity evolution history. Figure 4.5 gives an illustration to the intensity evolution history of the selected rows of pixels. The targeted rows of pixels is chosen as the 150th
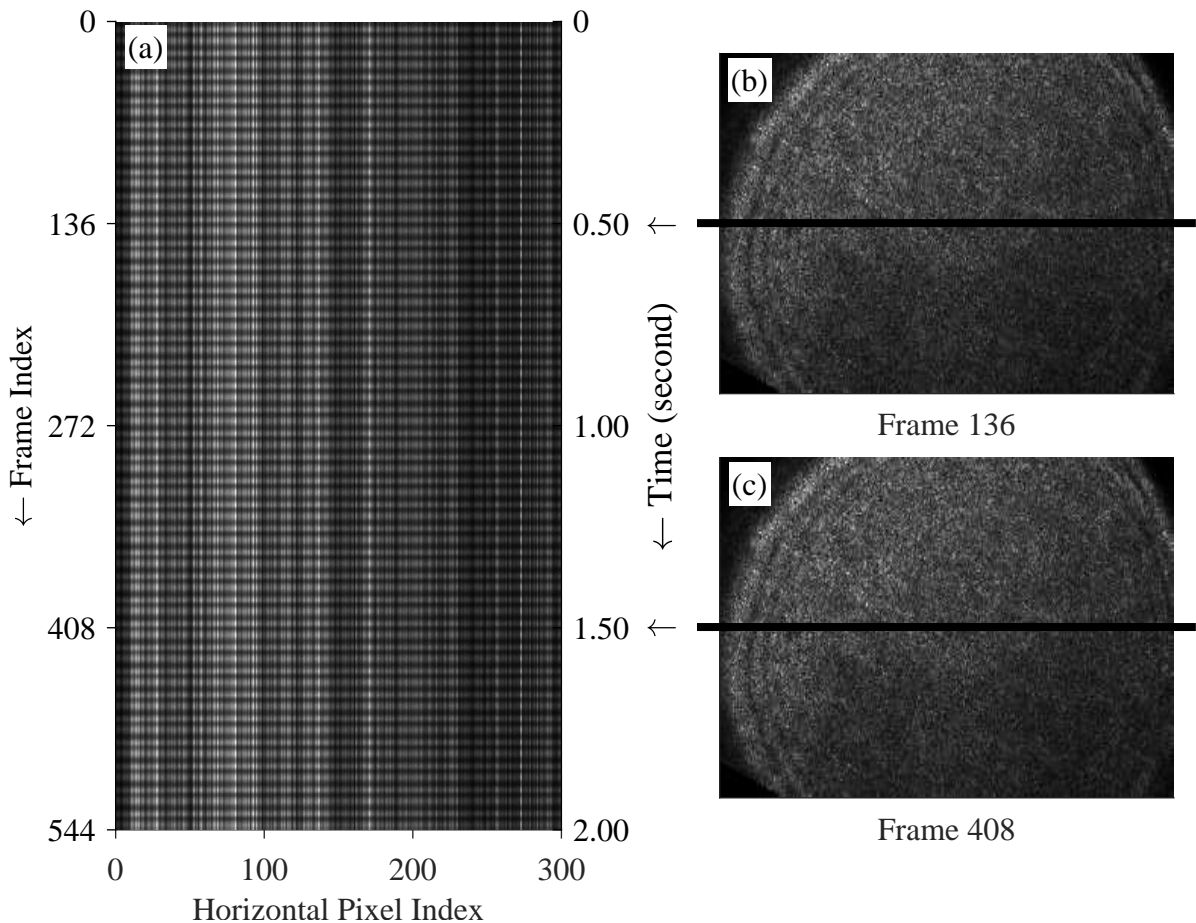
Figure 4.5: Temporal evolution history. (a) is the time sequence intensity of the 150th row of pixels in each frame. (b) and (c) are two example frames, showing where the selected rows are located.

rows in each frame, and stacked together in time sequence. That is how Figure 4.5(a) is generated. The black solid lines across the captured frames [see Figure 4.5(b) and (c)] indicate the location of the target rows of pixels. In the intensity evolution history, the periodical variation in the intensity from the top to the bottom is the proof of the temporal carrier which is introduced by the DTEO modulator. It is noted that only the first 544 frames out of the captured 1360 frames are considered in Figure 4.5(a).

To have a further examination of the intensity evolution history, the pixel which is indexed by (66,131) is selected and its 1360 measured intensities are transformed into the Fourier domain, as shown in Figure 4.6. Figure 4.6(a) illustrates the intensity captured within
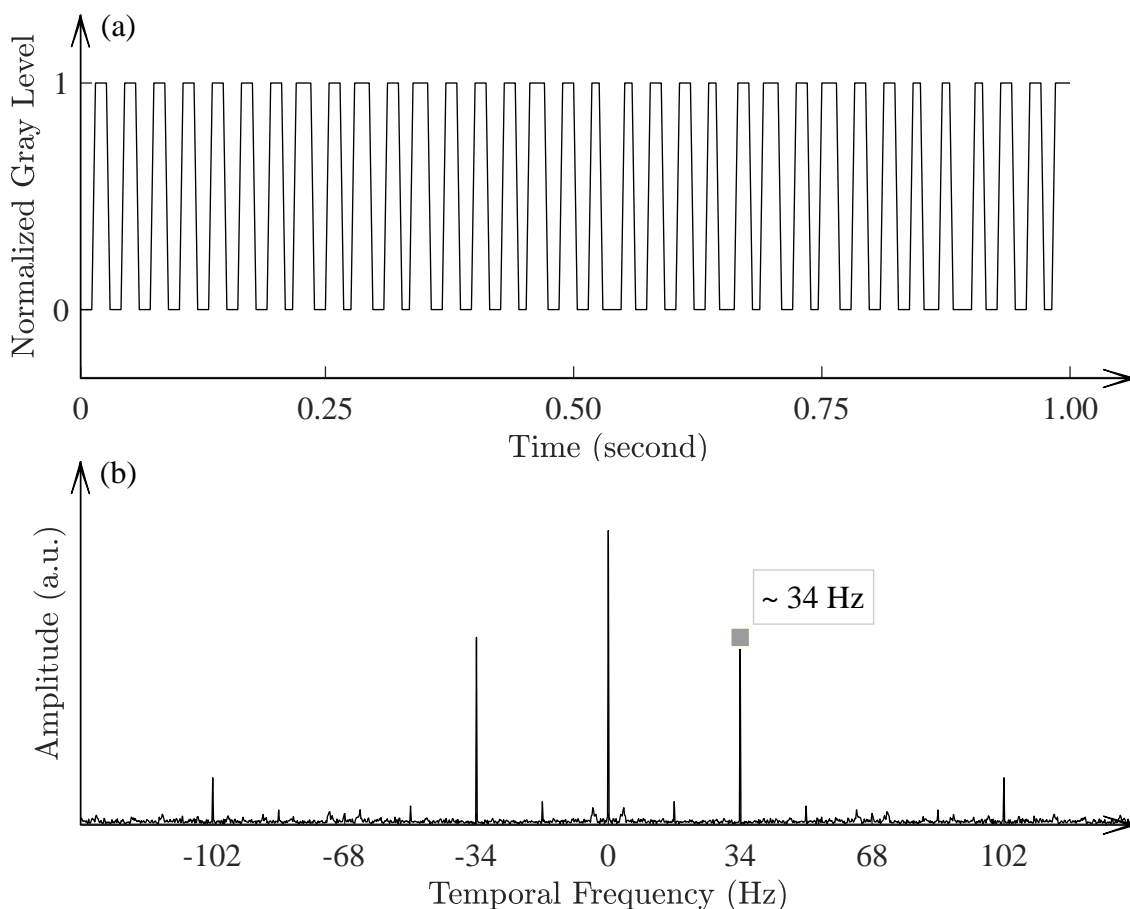
Figure 4.6: Time sequence intensity extracted from an example pixel. (a) is the intensity evolution history of the pixel within the first second. (b) is the corresponding Fourier spectrum of (a).

the first second (272 sampling points in time), whereas the entire 1360 sampling points are considered when calculating the Fourier spectrum. Theoretically, in the frequency domain, the temporal carrier undergoes certain kind of shift and broadening due to the rotation of the target. However, in Figure 4.6(b), the shift and the broadening is not so

obvious. This is because the 'speed' of the dynamic target is relatively low with respect to the temporal carrier and the frame rate of the camera.

The phase of an individual pixel is evaluated by the time sequence method introduced in Subsection 2.1.2, which is based on the Fourier transform. In the implementation, the isolated +1 order side lobe stays where it is, instead of being translated towards the origin in the Fourier spectrum. Thus, the retrieved phase contains the temporal carrier. To evaluate the pure rotation-induced phase change, the temporal carrier is removed mathematically from the direct retrieved phase [105], denoted by

$$\Delta\varphi(x,y,t) = \arctan\frac{\mathrm{Im}[c(x,y,t)]}{\mathrm{Re}[c(x,y,t)]} - 2\omega t, \qquad (4.21)$$

where $\mathrm{Im}\,[\,\cdot\,]$ and $\mathrm{Re}\,[\,\cdot\,]$ represent the real and imaginary parts, respectively, and $2\omega t$ stands for the temporal carrier. The purpose of such a replacement in data processing is to remove the step of finding out the amount of the side lobe translation, which is not generally an integer multiple of the sampling interval. A misleading determination of the amount of the side lobe translation results in an additional residual in the retrieved phase. By applying the phase retrieval algorithm to each and every pixel, the phase change distribution is obtained in both time and space, as shown in Figure 4.7. Nine examples
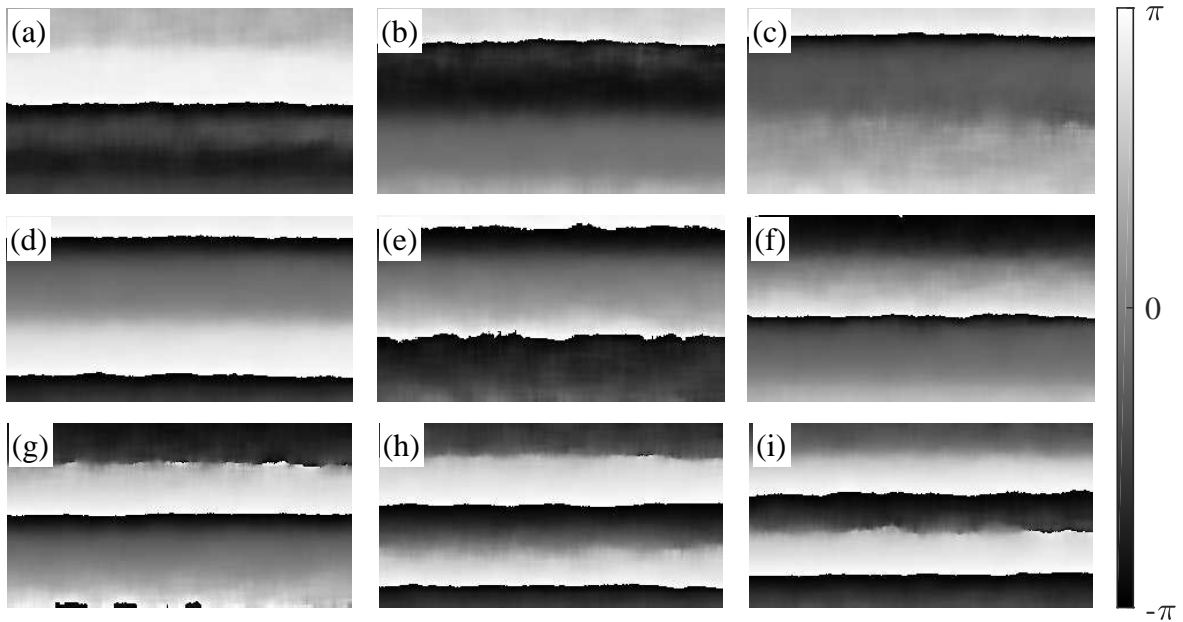

Figure 4.7: Nine examples of the phase change distributions. The illustrations are in equal time intervals from (a) to (i).

out of the 1360 retrieved phase change distributions are shown with an identical time

interval. The frame index of the first shown phase change distribution [Figure 4.7(a)] is 250, and the interval is 100 frames. In the illustration, the sine-cosine filter [105–107] is applied to remove the random noise from the phase change distribution.

It is shown that the retrieved phase maps are time-dependent, which in turn gives a demonstration to the dynamic feature of the proposed temporal ESPI system. To process further, Equations (4.19) and (4.20) are used to calculate the angle of the in-plane rotation from the retrieved phase change distributions. The evaluated angle is shown in Figure 4.8(a), in which the solid line is the evaluated angle and the dashed line is the theoretical
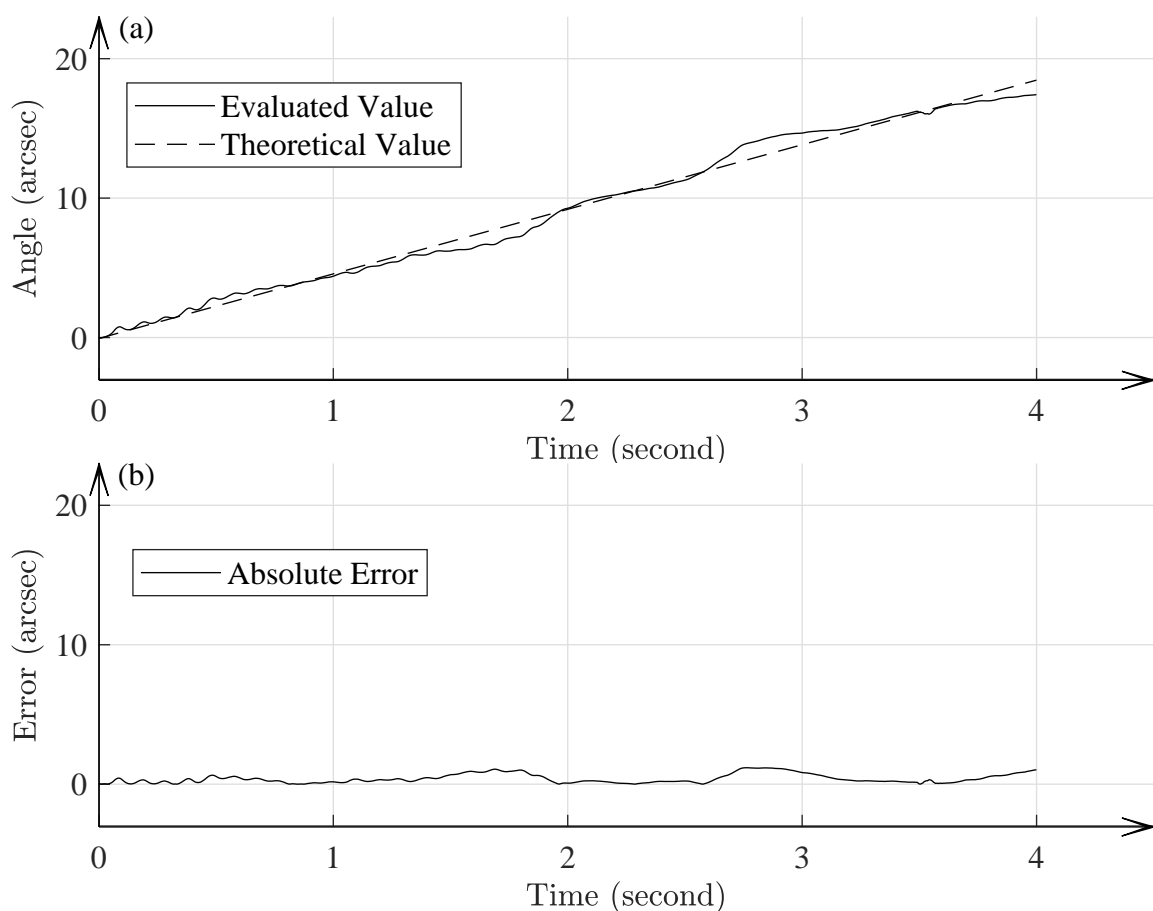

Figure 4.8: Measurement result of the in-plane rotation. (a) shows a comparison of the evaluated value and the theoretical value and (b) is the absolute error.

value. Considering the sensitivity vector of the current configuration, the partial derivative is calculated along the vertical direction. In the angle evaluation, the partial derivatives are all positive, which indicates that the target rotates continuously counterclockwise. By taking the absolute difference between the evaluated and the theoretical values, it yields the absolute errors for each sampling point in time. The mean absolute error in the current illustration is 0.39 arcsec.

4.4   Summary

This chapter presents a temporal ESPI system which is based on the DTEO phase modulator. Symmetric illumination is applied in the optical configuration. The system is dedicated to the measurement of the in-plane rotation. The rotation angles are evaluated quantitatively, and the direction of the rotation is obtained at the same time. The DTEO phase modulator provides a temporal frequency carrier in the system, from which the phase change distribution is retrieved. The mathematical model is established which describes the relationship between the phase change distribution and the rotation angle.

The feature of the temporal ESPI system is its capability of carrying out real-time measurements for dynamic targets. For achieving this, the key component is the DTEO phase modulator. The temporal frequency carrier introduced by the modulator satisfies the frame rate of most industrial cameras. Thus, the scanning unit is avoided in order to improve the time-resolution of the system. The general features, like non-destructive investigation, full-field measurement, and high accuracy, are the inherent characteristics of the ESPI systems, which are not demonstrated separately in this chapter.

In the data processing, the time-dependent phase change distribution is retrieved by the time sequence method. In order to improve the phase retrieval accuracy, the temporal carrier is removed mathematically instead of translating the isolated +1 order of the side lobe. Such an operation attempts to minimize the phase residual resulted from the leakage frequency. In another scenario, not shown in the present study, a lock-in amplifier is a promising alternative regarding the phase retrieval [108–111]. It reads out the phase change directly from the temporal carrier. However, most of the lock-in amplifiers collect the intensity by a point detector, which reduces the spatial resolution greatly. Herein, the lock-in amplifier is pointed out, because in certain applications the spatial resolution is not the first priority. In the present work, the data processing is taken as an useful tool instead of the focus of the study, so the details of the lock-in amplifier is reserved.

Chapter 5

DTEO Modulator in Holography

Holography is one of the most important branches of optical techniques. The shining feature of holography is its capability of reconstructing the optical field in both amplitude and phase, whereas for photography only the amplitude is recorded and presented. Technically, holography is considered as a combination of interference and diffraction. For a successful reveal of the object wave, two crucial procedures are involved in holography, namely the holography recording and the wavefront reconstruction. In the recording of holography, the two superposing waves form the interference. The pattern of the interference is called hologram which is then recorded by the recording media. The two superposing waves are the reference wave and the object wave, respectively. The reference wave is normally a plane wave, but sometimes a spherical wave also works with interesting behaviors. The object wave is literally the wave diffracted from the object which is illuminated coherently. To reconstruct the wavefront of the object, a replica of the aforementioned reference wave is required to illuminate the hologram. The illuminating wave is diffracted by the hologram and the wavefront of the three-dimensional (3-D) object is reconstructed in space.

The holography technique was first invented by Dennis Gabor in 1948 [112]. The novelty involves the two-step lensless imaging process, which is later known as wavefront reconstruction. For Gabor's conventional in-line configuration, the reconstruction suffers from a problem that the reconstructed image is mixed with the zero-order diffraction and the twin images. To address this issue, an off-axis configuration was proposed by Emmett Leith *et al.* [113–115]. In the off-axis configuration, the reference wave impinges the recording medium with an angle to the object wave. Thus, when reconstructing the hologram by using the tilted reference wave, the +1, 0, and -1 orders of diffraction are separated in space. Yet, holograms were still reconstructed by optical methods.

The digital holography was first proposed by Joseph W. Goodman *et al.*, in which they demonstrated the numerical reconstruction of the digitally recorded holograms [116]. Compared to the photosensitive films, the digital array detectors provide a relatively limited resolution, because the field is sampled by pixels. Moreover, the off-axis configuration undergoes a reduction in the resolution of the reconstructed image. To maintain the resolution of the digital holography and solve the superposition problem at the same time, phase-shifting digital holography was invented by Ichirou Yamaguchi *et al.* in 1997 [117], which is regarded as a significant contribution to the field. The reconstruction scheme involves the retrieval of the field at the detector plane and the numerical propagation. The retrieved field is numerically propagated from the detector plane to the plane in which the object originally is. In recent years, the phase-shifting holography grabs a great deal of attentions in academic society and industry, particularly, in the fields of biological and medical imaging, conventional physics, electrical engineering, etc.

In this chapter, a phase-shifting digital holography system is described, which is based on the DTEO phase modulator. The phase is modulated in the main path before the beam split. No mechanical movement is involved during the phase modulation. The system is configured in an in-line scheme to make full use of the spatial resolution provided by the array detector. In the meantime, the phase shift provides the access to the complex field at the detector plane. The target under investigation is reconstructed by the numerical propagation. In the following sections, the basics of the phase-shifting digital holography are first summarized, and the proposed system is described in both theory and experiments.

5.1   Basics in Digital Holography

Digital holography is generally shown as a promising technique for imaging applications. The most significant difference between conventional holography and digital holography is the recording media, or more precisely, the recording device. For conventional holography, the recording media is a photosensitive film. Post-treatment, namely the film develop, is compulsory to get the hologram. The digital holography removes the cumbersome chemical develop procedure and uses the electric devices to record the hologram digitally. Such a replacement brings around new applications and capabilities for the holography technique.

Despite its many merits which are known for years, conventional holography is generally grounded in laboratories, because of the complex steps and the strict requirement of the operation environment. Practical applications are thus restricted. Except for some special and dedicated materials, the photosensitive film is considered as a barrier for achieving

a real-time imaging in conventional holography. In digital holography, the holograms are captured by array detector, e.g., CCD cameras. The digitalized holograms are then transfered to a host computer for further processing. By using the diffraction theory, the propagation of the optical field is precisely modeled, which lays the basics for the foundation of the numerical reconstruction of the holograms in both intensity and phase. Digital holography provides quite a lot of significant advantages, e.g., the fast access to the hologram and the complete description of the optical field. More importantly, a good number of digital image processing techniques are at hand for further interpretation of the holograms.

5.1.1 Recording and Reconstruction

Leaving apart the recording unit of a holography system, this subsection gives a description to the general optical configuration of holography. In the recording of holograms, both the intensity and the phase of the optical field are recorded. The illumination wave is reflected by or goes through the object and thus becomes the object wave which carries the information of the object. According to the Huygens-Fresnel principle, the object wave is seen as the superposition of the spherical wavelet of every point on the object [53], denoted by

$$\widetilde{U}_{obj}\left(Q\right) = \sum \widetilde{u}_{n}\left(Q\right) = A_{obj}\left(Q\right) \cdot \exp\left\{-j\left[\phi_{obj}\left(Q\right)\right]\right\}, \tag{5.1}$$

where Q represents a point at the object wavefront, $\widetilde{u}_{n}$ is the individual wavelet with n being a large number. It is shown that in order to get a complete description of the object wave, both the amplitude, $A_{obj}\left(Q\right)$, and the phase, $\phi_{obj}\left(Q\right)$, are demanded to be recorded.

In holography, the optical field is recorded by the means of interference. Both the amplitude and the phase are encoded in the interference pattern. An off-axis configuration is treated as an example for the demonstration of holography, as shown in Figure 5.1. The illumination wave is split by the beam splitter and directed to the object and the mirror, respectively. The wave carries the object information is labeled as object wave [see Equation (5.1)] and the one directed to the mirror as the reference wave. The term off-axis refers to the off-set of the angle between the wave vector of the reference wave and the normal of the recording plane. Based on the describing coordinate system shown in Figure 5.1, the reference wavefront at the hologram plane is thus denoted by

$$\widetilde{U}_{ref} = A_{ref} \cdot \exp\left(j\frac{2\pi}{\lambda}\sin\theta \cdot x\right), \tag{5.2}$$
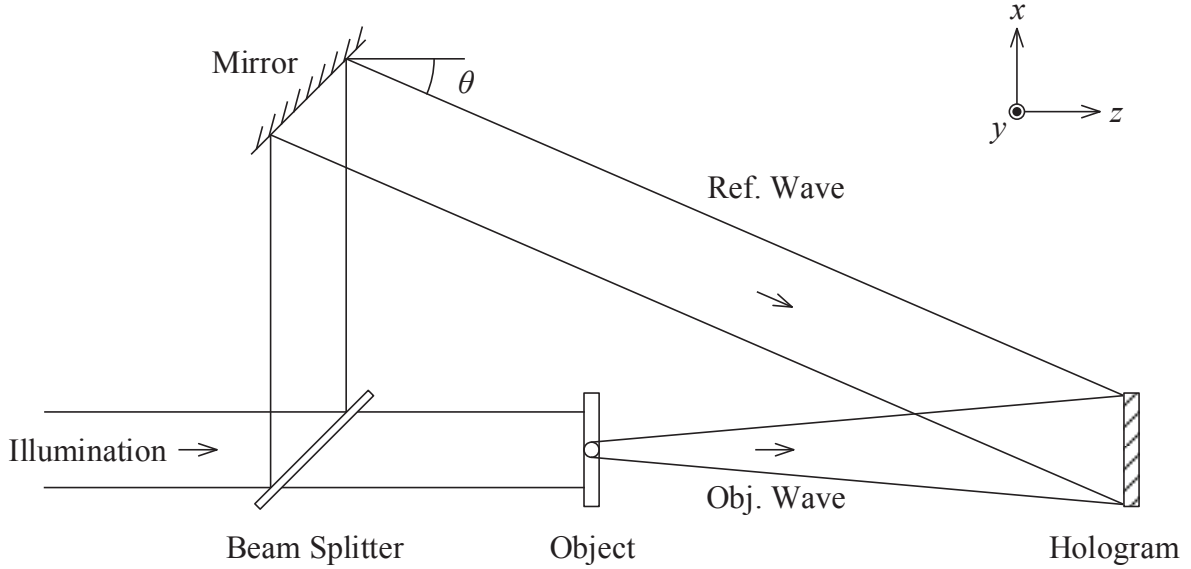
Figure 5.1: Off-axis configuration for the recording of a hologram.

where θ is the off-set angle. The interference between the object and the reference waves at the recording plane forms the hologram, mathematically denoted by

$$
\begin{aligned}
I\left(x,y\right) &= \left|\widetilde{U}_{obj}\left(x,y\right) + \widetilde{U}_{ref}\left(x,y\right)\right|^2 \\
&= A_{obj}^2 + A_{ref}^2 + \widetilde{U}_{obj}\left(x,y\right)\widetilde{U}_{ref}^*\left(x,y\right) + \widetilde{U}_{ref}\left(x,y\right)\widetilde{U}_{obj}^*\left(x,y\right).
\end{aligned}
\tag{5.3}
$$

It is worth noting that there is a periodical intensity distribution of the off-axis hologram due to the off-set angle. The spatial frequency of the periodical variation is denoted by

$$
f_{sp} = \frac{\sin\theta}{\lambda}.
\tag{5.4}
$$

The term f_{sp} is known as the spatial carrier frequency. In conventional holography, provided the off-set angle is sufficiently large, the different orders of diffraction are spatially separated in the process of reconstruction. However, in digital holography, there is a limitation regarding the maximum of the off-set angle. It is determined by the spatial sampling interval of the recording device. Or, put it another way, the maximal value is limited to fulfill the sampling theorem. The maximum off-set angle is denoted by [118]

$$
\theta_{max} \approx \frac{\lambda}{2\Delta l},
\tag{5.5}
$$

where Δl is the spatial sampling interval of the recording device.

In this current illustration, conventional holography is considered. The hologram is then recorded by a photosensitive film and the hologram is reconstructed optically. For simplicity, the amplitude transmittance of the developed film is assumed a linear function of the intensity described by Equation (5.3), denoted by

$$t\left(x,y\right) = t_0 + \beta I\left(x,y\right), \tag{5.6}$$

where t_0 stands for the initial transmittance of the film, β is a parameter related to the exposure time and the photon sensitivity of the film material. After chemical developing, the film is placed back to the same position as in the recording configuration shown in Figure 5.2. The developed film (hologram) is illuminated by the reconstruction wave which
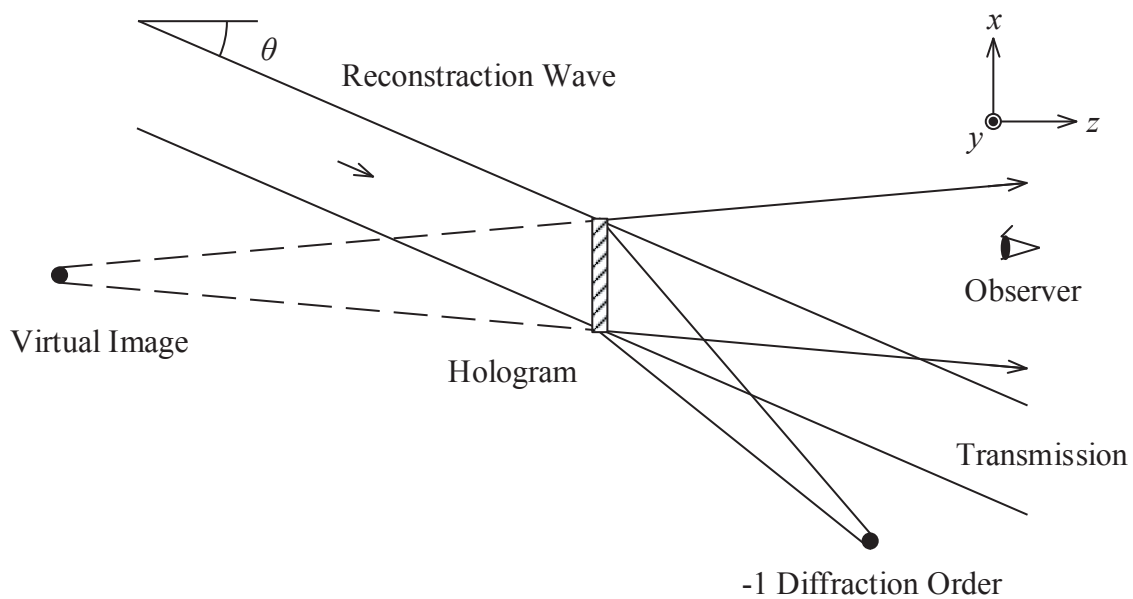
Figure 5.2: Off-axis configuration for the reconstruction of a hologram.

is a replica of the reference wave in terms of the wave vector. Through the diffraction of the hologram, the reconstruction wave becomes

$$\begin{aligned} \widetilde{U}_{ref}\left(x,y\right) \cdot t\left(x,y\right) &= \left[t_0 + \beta\left(A_{obj}^2 + A_{ref}^2\right)\right] \cdot \widetilde{U}_{ref}\left(x,y\right) \\ &\quad + \beta A_{ref}^2 \cdot \widetilde{U}_{obj}\left(x,y\right) + \beta\widetilde{U}_{ref}^2\left(x,y\right) \cdot \widetilde{U}_{obj}^*\left(x,y\right). \end{aligned} \tag{5.7}$$

The first item on the right is the construction (reference) wave multiplied by a constant. Referring to Figure 5.2, it appears as the direct transmission, the non-diffracted wave, or

the zero-diffraction order. The second item is the reconstruction of the object wavefront. In the illustration, a virtual image of the original object is observed. Physically, the second item is the +1 diffraction order. The real factor in front of the object wavefront, $\widetilde{U}_{obj}$, only has an influence on the overall brightness of the reconstructed virtual image. As for the -1 diffraction order, it is shown as the third item in Equation (5.7). A real image of the object is generated with distortion. The origin of the distortion is the spatial variation in the squared complex field, $\widetilde{U}_{ref}^2$. Under a proper selection of the off-set angle, the three diffraction orders are completely separated in space. It is noted that, in digital holography, which uses the electronic detector for the recording, the term of initial transmittance [t_0 in Equation (5.6)] is neglected. Thus, it is capable to apply Equation (5.6) to the description of both conventional and digital holography.

5.1.2 Numerical Reconstruction of Wavefront

The digital holography is nothing more than conventional holography, save that the recording media is an electronic array detector rather than a photosensitive film. Chemical developing of the film is not necessary any longer. For the reconstruction, digital holography relies on the numerical calculation instead of illuminating the hologram by a replica of the reference wave. The virtual image, as well as the real image and the non-diffraction wave, is calculated at a given plane. The results are presented on a monitor for visualization.

The fundamental of numerical reconstruction is the diffraction integral. The spatial coordinates of each concerning plane are illustrated in Figure 5.3. The hologram is captured at the hologram plane by the electronic device. Here, a precondition is assumed that a plane wave perpendicularly illuminates the target for the recording process. In the numerical reconstruction, the diffraction field at the hologram plane is first calculated and then propagates numerically to the reconstruction plane. The propagation is modeled by the Fresnel-Kirchhoff integral [119], denoted by

$$\Gamma\left(\xi',\eta'\right) = \frac{j}{\lambda} \iint I\left(x,y\right) \widetilde{U}_{ref}\left(x,y\right) \frac{\exp\left(-jk\rho'\right)}{\rho'} \mathrm{d}x\mathrm{d}y, \qquad (5.8)$$

where $I\left(x,y\right)$ is the intensity of the hologram described by Equation (5.3), $\widetilde{U}_{ref}\left(x,y\right)$ stands for the reconstruction wavefront at the hologram plane, k represents the wave number, and ρ' is the distance from a point in the hologram plane to a point in the reconstruction plane. Specifically, the distance, ρ', is calculated by

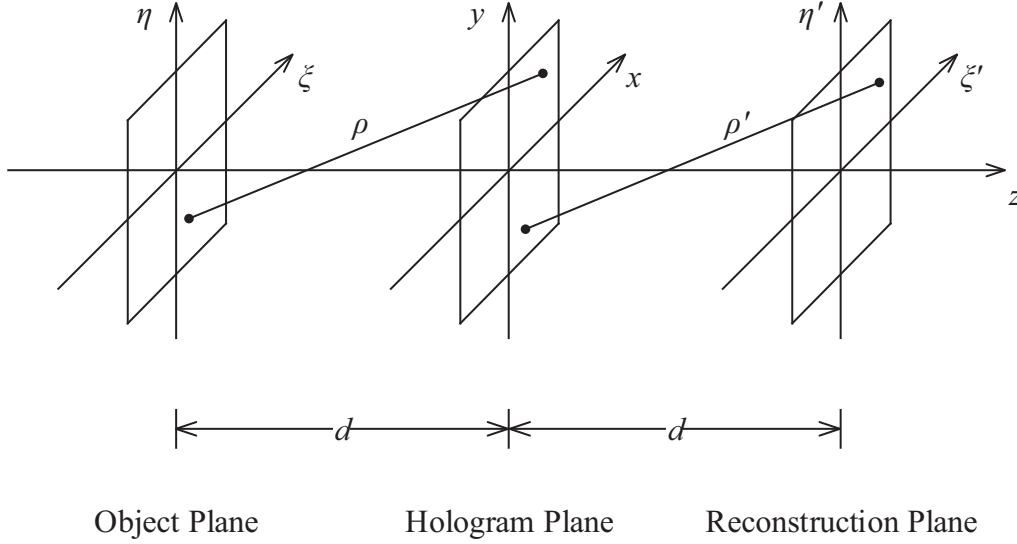$$\rho' = \sqrt{(x - \xi')^2 + (y - \eta')^2 + d^2}, \qquad (5.9)$$

Figure 5.3: Coordinate systems for the corresponding planes in numerical reconstructions.

where the paraxial approximation [120] is considered in the calculation. Equation (5.8) reconstructs the complex field of the real image [-1 order of diffraction in Figure 5.2]. In the discussion of Equation (5.7), it is shown that the real image is tangled with distortion. In order to calculate the undistorted real image, the conjugated field of $\widetilde{U}_{ref}(x,y)$ is taken into account for Equation (5.8) and the field is numerically propagated from the hologram plane to the object plane [121], denoted by

$$\Gamma(\xi,\eta) = \frac{j}{\lambda} \iint I(x,y) \widetilde{U}^*_{ref}(x,y) \frac{\exp(-jk\rho)}{\rho} \mathrm{d}x\mathrm{d}y, \qquad (5.10)$$

where the distance ρ has a similar definition shown in Equation (5.9). It is noted that the reference wave and its conjugation are equivalent, $\widetilde{U}_{ref} = \widetilde{U}^*_{ref} = A_{ref}$, because it is a plane wave with a wave vector perpendicular to the hologram plane. Hence, the real image is reconstructed numerically by Equation (5.10) at the object plane without distortion. The direct processing of the diffraction integral is time consuming and sometimes fails to get an analytical solution. Hence, for an efficient calculation of Equation (5.10), two approaches are mostly used, namely the Fresnel transform and the convolution method.

Fresnel Transform Considering practical configurations, the axial length, d, is larger than the transverse dimensions. Taylor series is used to expand the distance function,

denoted by

$$\rho = d + \frac{(\xi - x)^2}{2d} + \frac{(\eta - y)^2}{2d} - \frac{1}{8} \frac{\left[(\xi - x)^2 + (\eta - y)^2\right]^2}{d^3} + \cdots . \tag{5.11}$$

The fourth item (and the items in higher orders) are neglected upon the fact that they are small with respect to the wavelength. Thus, in the calculation of the diffraction integral, only the linear and the quadratic terms are maintained for an approximation. Equation (5.10) then becomes [121]

$$\Gamma(\xi, \eta) = \frac{j \exp(-jkd)}{\lambda d} \iint I(x,y) \, \widetilde{U}_{ref}^*(x,y) \exp\left\{-\frac{jk}{2d}\left[(\xi - x)^2 + (\eta - y)^2\right]\right\} \mathrm{d}x\mathrm{d}y. \tag{5.12}$$

In a detailed investigation of Equation (5.12), the squared functions in the exponential are expanded, denoted by

$$\begin{aligned}
\Gamma(\xi, \eta) = & \frac{j \exp(-jkd)}{\lambda d} \exp\left[-\frac{jk}{2d}\left(\xi^2 + \eta^2\right)\right] \\
& \times \iint I(x,y) \, \widetilde{U}_{ref}^*(x,y) \exp\left[-\frac{jk}{2d}\left(x^2 + y^2\right)\right] \exp\left[\frac{jk}{d}\left(x\xi + y\eta\right)\right] \mathrm{d}x\mathrm{d}y.
\end{aligned} \tag{5.13}$$

By introducing a proper definition and substitution, it is apparent that the second exponential in the integral sees a Fourier transform kernel, represented by

$$\begin{aligned}
\Gamma(u, v) = & \frac{j \exp(-jkd)}{\lambda d} \exp\left[-j\pi\lambda d\left(u^2 + v^2\right)\right] \\
& \times \iint I(x,y) \, \widetilde{U}_{ref}^*(x,y) \exp\left[-\frac{jk}{2d}\left(x^2 + y^2\right)\right] \underbrace{\exp\left[j2\pi\left(xu + yv\right)\right]}_{\text{Fourier transform kernel}} \mathrm{d}x\mathrm{d}y,
\end{aligned} \tag{5.14}$$

with

$$u = \frac{\xi}{\lambda d}, \; v = \frac{\eta}{\lambda d}. \tag{5.15}$$

Rewriting Equation (5.14) in the form of Fourier transform yields

$$\begin{aligned}
\Gamma(u, v) = & \frac{j \exp(-jkd)}{\lambda d} \exp\left[-j\pi\lambda d\left(u^2 + v^2\right)\right] \\
& \times \mathscr{F}^{-1}\left\{I(x,y) \, \widetilde{U}_{ref}^*(x,y) \exp\left[-\frac{jk}{2d}\left(x^2 + y^2\right)\right]\right\},
\end{aligned} \tag{5.16}$$

where $\mathscr{F}^{-1}[\,\cdot\,]$ stands for the inverse Fourier transform operation.

The derivation introduced above is known as the Fresnel transform, which is used for the digital reconstruction of holograms. It is readily carried out by using the Fourier

transform. In the reconstructed object wave, the intensity is given by

$$I\left(\xi,\eta\right) = \left|\Gamma\left(\xi,\eta\right)\right|^2 \tag{5.17}$$

and the phase by

$$\phi_{obj}\left(\xi,\eta\right) = \arctan\frac{\mathrm{Im}\left[\Gamma\left(\xi,\eta\right)\right]}{\mathrm{Re}\left[\Gamma\left(\xi,\eta\right)\right]}. \tag{5.18}$$

Convolution Method A different interpretation of Equation (5.10) is based on the convolution theorem. The convolution method is also known as the angular spectrum method (ASM) [122]. In Equation (5.10) the superposition integral is thus performed as

$$\Gamma\left(\xi,\eta\right) = \iint I\left(x,y\right)\widetilde{U}_{ref}^*\left(x,y\right)g\left(\xi,\eta,x,y\right)\mathrm{d}x\mathrm{d}y, \tag{5.19}$$

with the impulse response function, $g\left(\xi,\eta,x,y\right)$, being [123]

$$g\left(\xi,\eta,x,y\right) = \frac{j}{\lambda}\cdot\frac{\exp\left[-jk\sqrt{\left(x-\xi\right)^2+\left(y-\eta\right)^2+d^2}\right]}{\sqrt{\left(x-\xi\right)^2+\left(y-\eta\right)^2+d^2}}. \tag{5.20}$$

It is concluded from Equation (5.20) that the impulse response function is space-invariant, namely $g\left(\xi,\eta,x,y\right) = g\left(\xi-x,\eta-y\right)$, which further indicates that the reconstruction process is a linear system. According to the statement of the convolution theorem, the Fourier transform of the reconstructed wavefront is the pointwise product of the Fourier transforms of the diffraction field immediately behind the hologram plane and the impulse response function. The mathematics gives [124]

$$\Gamma\left(\xi,\eta\right) = \mathscr{F}^{-1}\left\{\mathscr{F}\left[I\left(x,y\right)\widetilde{U}_{ref}^*\left(x,y\right)\right]\cdot\mathscr{F}\left[g\left(\xi-x,\eta-y\right)\right]\right\}. \tag{5.21}$$

Noting that it is possible to model and calculate the Fourier transform of the impulse response function, $\mathscr{F}\left[g\left(\xi-x,\eta-y\right)\right]$, directly, so that one Fourier transform operation in the calculation of Equation (5.21) is saved. The Fourier transform of the impulse response function is analytically expressed [125] by

$$G\left(f_x,f_y\right) = \exp\left(-jkd\sqrt{1-\lambda^2 f_x^2-\lambda^2 f_y^2}\right), \tag{5.22}$$

where f_x and f_y are the spatial frequencies in the Fourier domain. Thus, the convolution method is simplified as

$$\Gamma\left(\xi,\eta\right) = \mathscr{F}^{-1}\left\{\mathscr{F}\left[I\left(x,y\right)\widetilde{U}_{ref}^*\left(x,y\right)\right]\cdot G\left(f_x,f_y\right)\right\}. \tag{5.23}$$

In the experiment section of this chapter, the convolution method is applied for the reconstruction of the object wave. The advantage is that the convolution method does not take any approximation to the calculation. The standard steps are collected as following:

1. Calculating the Fourier transform of the diffracted wavefront at the hologram plane.

2. Numerically describing the Fourier transform of the impulse response function.

3. Multiplying the Fourier transforms in Steps 1 and 2.

4. Calculating the inverse Fourier transform of the result from Step 3.

Finally, the object wave is reconstructed in terms of both phase and amplitude.

5.2   Optical Configuration

Digital holography gives the possibility of introducing a phase shift between the object and the reference waves. This is a significant difference to conventional holography. Numerical operations, such as additions, subtractions, and manipulations, are easily carried out for the captured holograms. As a result, the object field on the hologram plane is figured out by using the phase-shifting technique. The numerical propagation of the field on the hologram plane is calculated by the diffraction integral in a certain form. Thus, at the object plane, a real image (complex field) is obtained in another way around. This kind of holography is known as phase-shifting digital holography.

Actually, given that the object field on the hologram plane is known, the optical field at any plane can be calculated by the numerical diffraction. So the phase-shifting digital holography has the post-focusing or refocusing ability. As introduced in the previous section, the off-axis configuration provides a straightforward scheme to introduce a spatial phase shift between the object and the reference waves. One of the limitations of the off-axis configuration in phase-shifting digital holography is that the resolution in the reconstruction is only a fraction of that in the array detector. To make full use of the resolution of the array detector, in-line configuration is required, in which the spatial phase shift is difficult to be carried out. Hence, rather than the spatial phase shift, the temporal phase shift is introduced in the in-line configuration, which requires a reliable phase modulator.

In the proposed configuration, as shown in Figure 5.4, the DTEO phase modulator is used to introduce the temporal phase shift, or more precisely, the temporal frequency carrier. The linearly polarized wave is provided by a laser. At the output end of the laser, a HWP is used to orient the polarization along, for example, the x-axis. The coherent monochromatic wave which is prepared to enter the DTEO phase modulator is
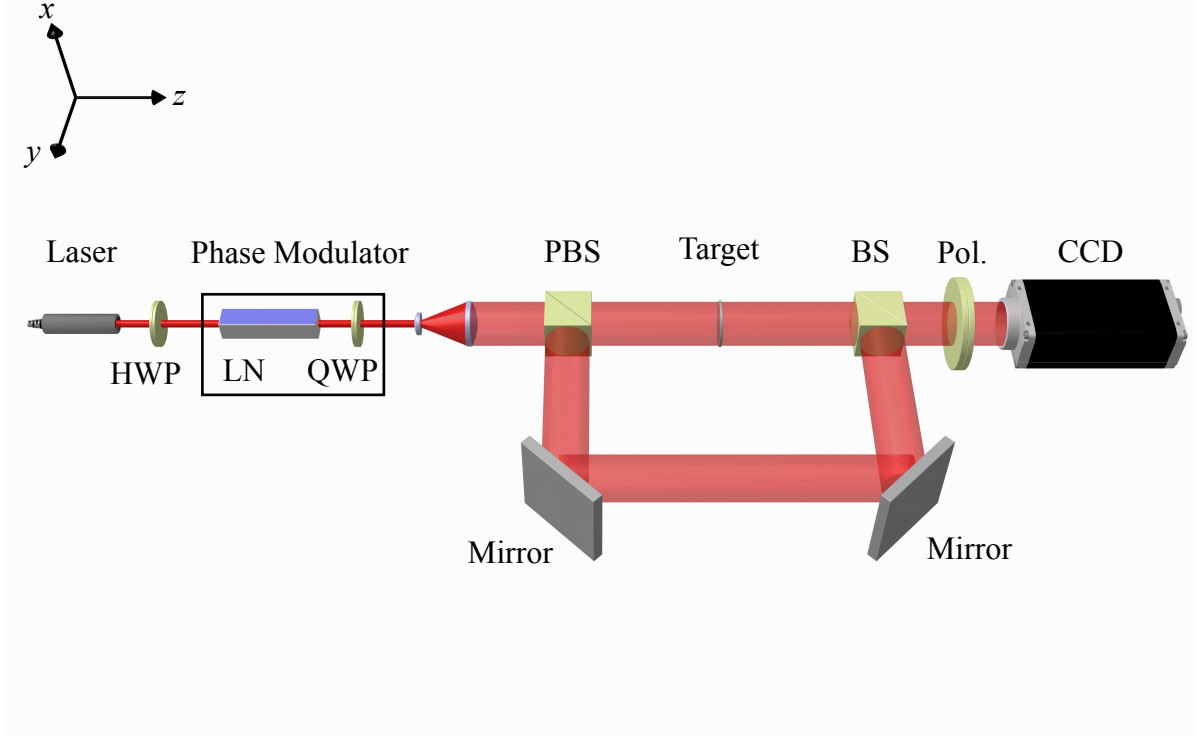
Figure 5.4: Optical configuration of the proposed phase-shifting digital holography.

then denoted by

$$V_0 = \begin{bmatrix} A_0 \\ 0 \end{bmatrix} \exp\left(-j\omega_0 t\right), \tag{5.24}$$

where ω_0 represents the optical frequency of the input laser and A_0 stands for the amplitude. The fast axis of the QWP in the phase modulator is oriented at 45° with respect to the x-axis. The phase modulation is mathematically denoted by

$$\begin{bmatrix} V_x \\ V_y \end{bmatrix} = T_{PM} \cdot V_0 = \frac{\sqrt{2}}{2} A_0 \cdot \begin{bmatrix} \exp\left[-j\left(\omega_0 t + \omega t\right)\right] \\ \exp\left[-j\left(\omega_0 t - \omega t - \frac{\pi}{2}\right)\right] \end{bmatrix}, \tag{5.25}$$

where T_{PM} stands for the function of the DTEO phase modulator [see Equation (3.43)]. The modulated laser beam is expanded and collimated by a set of lenses which form a Keplerian telescope. Inside the PBS, the laser beam is split according to the polarization. It is assumed that the x-polarized component transmits through the PBS, and the y-polarized component is reflected. The transmission wave illuminates the target. The diffraction field immediately behind the target is labeled by $V_{obj}\left.\right|_{OP}(\xi, \eta)$, where the subscript OP means object plane. This field is hereinafter named by object field for convenience. If the phase shifting in the illumination is considered, the object field is

then time-dependent, denoted by

$$V_{obj} \mid_{OP} (\xi,\eta,t) = V_{obj} \mid_{OP} (\xi,\eta) \cdot V_x (t) . \qquad (5.26)$$

The reflected wave serves as the reference wave, $V_{ref} = V_y$. Noted that, the axial distance is neglected when the wave is described, because the phase introduced by the axial distance presents as a constant phase. The only exception is the discussion of the reconstruction, in which the axial distance is crucial to the result. A non-polarizing beam splitter (BS) is used to recombine the diffracted object wave and the reference wave. The BS is aligned to a state that an in-line hologram is generated at the detector plane. A 45°-oriented polarizer is inserted between the BS and the detector plane to force the two orthogonally polarized waves superpose with each other coherently. A CCD camera is placed at the detector plane to capture the holograms.

Mathematically, the captured hologram is denoted by

$$I (x,y,t) = \left[V_{obj} \mid_{HP} \cdot \frac{\sqrt{2}}{2} V_x (t) + \frac{\sqrt{2}}{2} V_{ref} \right] \cdot \left[V_{obj} \mid_{HP} \cdot \frac{\sqrt{2}}{2} V_x (t) + \frac{\sqrt{2}}{2} V_{ref} \right]^* , \quad (5.27)$$

where $V_{obj} \mid_{HP}$ is the object wavefront at the hologram plane (HP), the constant factor $\frac{\sqrt{2}}{2}$ comes from the 45°-oriented polarizer. Physically, the object wavefront $V_{obj} \mid_{HP}$ is generated by the propagation of $V_{obj} \mid_{OP}$ from the object plane ($\xi\eta$, OP) to the holography plane (xy, HP). The numerical propagation is readily calculated by the Fresnel transform or the convolution introduced in the previous subsection. Hence, the task of the reconstruction becomes finding out the object wavefront distribution, $V_{obj} \mid_{HP}$, at the hologram plane.

The linearly time-varying phase shift between the object and the reference waves provides an approach to the calculation of the object wavefront distribution at the hologram plane. Rewriting Equation (5.27) yields

$$I (x,y,t) = \frac{A_0^2}{4} \left\{ |V_{obj} \mid_{HP} (x,y)|^2 + 1 \right\} + \frac{A_0^2}{4} \cos \left\{ 2\omega t + \arg \left[V_{obj} \mid_{HP} (x,y) \right] \right\} , \qquad (5.28)$$

where $\arg \left[V_{obj} \mid_{HP} (x,y) \right]$ stands for the phase of the object wavefront at the hologram plane. Equation (5.28) shows a typical description of the phase-shifting interference pattern. Considering the linearly time-varying phase shift, namely the temporal frequency carrier, a set of phase-shifting holograms is captured in time sequence and analyzed pixel-wise. A single individual pixel, indexed by (x_0,y_0), is selected for further demonstration. The Fourier transform is applied to the time-sequenced intensity of the selected pixel.

Rewriting Equation (5.28) in the form of exponential gives

$$I(x_0, y_0, t) = a(x_0, y_0) + c(x_0, y_0) \cdot \exp(j2\omega t) + c^*(x_0, y_0) \cdot \exp(-j2\omega t), \qquad (5.29)$$

where the time-dependent components, namely the introduced temporal phase modulation, are written separately from the stationary items. The substitutions of $a(x_0, y_0)$ and $c(x_0, y_0)$ are specified by

$$a(x_0, y_0) = \frac{A_0^2}{4} \left\{ |V_{obj}|_{HP}(x_0, y_0)|^2 + 1 \right\}, \qquad (5.30a)$$

$$c(x_0, y_0) = \frac{A_0^2}{8} \exp\left\{ j \cdot \arg[V_{obj}|_{HP}(x_0, y_0)] \right\}. \qquad (5.30b)$$

The Fourier spectrum of the time-sequenced intensity is described by

$$\mathscr{F}[I(x_0, y_0, t)](x_0, y_0, f_t) = A(x_0, y_0, f_t) + C(x_0, y_0, f_t - \omega/\pi) + C^*(x_0, y_0, f_t + \omega/\pi). \quad (5.31)$$

In a plot of such a spectrum, A appears as the DC component which is located at the origin, C and C^* are the +1 and -1 orders of the side lobe, respectively. A filter is used to isolate the +1 order side lobe which is then translated towards the origin by an amount of ω/π. Inverse Fourier transform is applied to the isolated and translated side lobe in order to obtain the complex function $c(x_0, y_0)$. The phase of the object wavefront at the hologram plane is then evaluated by

$$\phi_{obj}|_{HP}(x_0, y_0) = \arg[V_{obj}|_{HP}(x_0, y_0)] = \arctan\left\{ \frac{\text{Im}[c(x_0, y_0)]}{\text{Re}[c(x_0, y_0)]} \right\}. \qquad (5.32)$$

As for the amplitude $A_{obj}|_{HP}(x_0, y_0)$, it is obtained physically by blocking the reference wave. When the phase and the amplitude are both accessible, the object wavefront at the hologram plane is thus described by

$$V_{obj}|_{HP}(x_0, y_0) = A_{obj}|_{HP}(x_0, y_0) \cdot \exp[j\phi_{obj}|_{HP}(x_0, y_0)]. \qquad (5.33)$$

Equation (5.33) gives a single point of the wavefront. The object wavefront over the hologram plane is retrieved by applying the method introduced above to every single pixel. Finally, to numerically reconstruct the object wavefront at the object plane, the back propagation of $V_{obj}|_{HP}(x, y)$ is calculated by the convolution method, denoted by

$$V_{obj}|_{OP}(\xi, \eta) = \mathscr{F}^{-1}\left\{ \mathscr{F}[V_{obj}|_{HP}(x_0, y_0)(x, y)] \cdot G(f_x, f_y) \right\}, \qquad (5.34)$$

where $G(f_x, f_y)$ is the Fourier spectrum of the impulse response function [Equation (5.22)].

5.3 Experiments and Results

In this section, the proposed phase-shifting digital holography is shown experimentally with the proposed optical configuration. The testing object is a USAF resolution target, which is customarily regarded as a typical target to verify holography systems. The experimental setup is configured according to Figure 5.4. Basic parameters of the system regarding the DTEO phase modulator and the light source are shown in Subsection 3.2.2, not repeated here. The other crucial parameters are given in the list below:

- Testing object: 1951 USAF Resolution Test Targets, Thorlabs Inc.

    - Positive target with a chrome pattern plated onto a clear substrate;

    - Target index: Group 2, Elements 3-6;

    - Resolution: 5.04 lp/mm - 7.13 lp/mm;

- Diffraction distance:

    - about 11 cm from the target to the hologram plane;

- Lenses:

    - Focal Length: L1 = -6 mm; L2 = 75 mm;

- Array detector: CCD camera, Basler piA640-210gm

    - Frame rate: 136 fps;

    - Region of interest: 488 px × 275 px;

    - Pixel size: 7.4 μm × 7.4 μm;

    - Pixel bit depth: 8 bits;

    - Acquisition time: 2 seconds;

A set of phase-shifting holograms are captured. The number of frames is 272. The temporal sampling interval is constant between frames. Considering the frame rate of the camera and the linearly time-varying phase shift, four frames are captured in a full cycle (2π) of the phase shift. Figure 5.5 gives four successive frames to illustrate a full cycle of phase shift between holograms. The intensity variations between holograms indicate the linearly time-varying phase shift. The four images are blurry, because there is no imaging lens in the system. The captured images are the interference patterns, which are generated from the coherent superposition of the diffraction field and the reference plane wave. In each individual frame, the spatial intensity variation comes from the imperfect illumination. The spatial variation does not have a major influence on the hologram
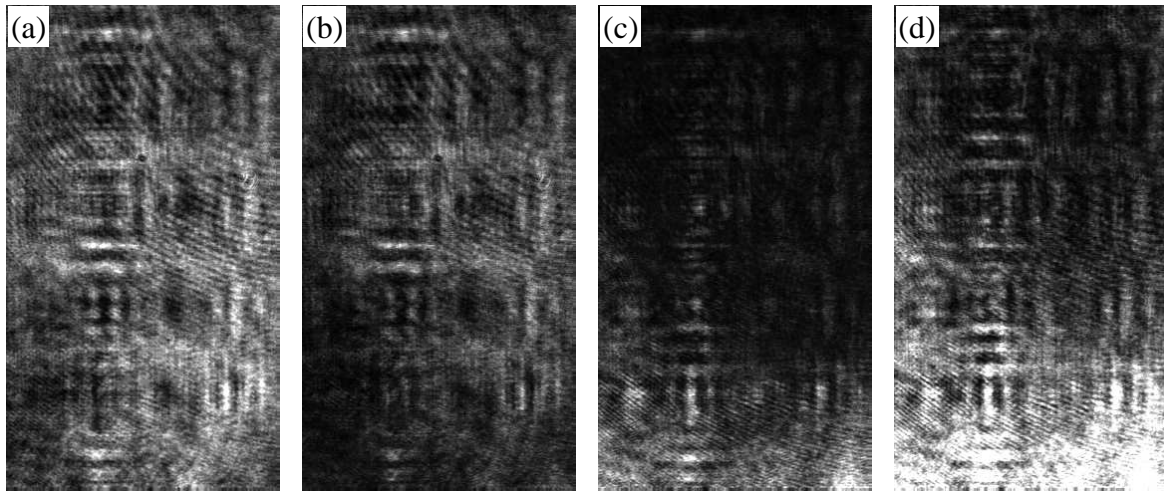
Figure 5.5: Phase-shifting holograms. The frames are in a single cycle of the phase shift and arranged successively in time sequence from (a) to (d).

reconstruction, because the phase-shifting holograms are analyzed pixel by pixel along the time axis.

From the captured set of holograms, the phase of the object wavefront at the hologram plane is calculated by using the time sequence method introduced in the last section. To obtain the amplitude of the wavefront, the optical path of the reference wave is blocked, so that, at the CCD camera plane, only the diffraction intensity of the testing object is collected. The amplitude of the wavefront is calculated by taking the square root of the diffraction intensity. Hence, the complex field of the object at the hologram plane is retrieved. The corresponding amplitude and phase are shown in Figure 5.6. The amplitude is normalized in this illustration.

In order to retrieve the wavefront at the object plane, back propagation is calculated by the convolution method. The distance of the back propagation, namely the distance from the hologram plane to the object plane, runs from 8.5 cm to 13.9 cm with an interval of 0.6 cm. Ten slices along the propagation are reconstructed and shown in Figure (5.7). The reconstructed slices show the refocusing ability of the digital holography. By the comparison between reconstructions, Figure (5.7)(e) appears as the sharpest. It means that at the distance of 10.9 cm from the hologram plane, the target is best reconstructed. The strips, as well as the element index, are clearly presented in Figure (5.7)(e).

As a post-note of the reconstruction, it is useful to indicate the digitalization which is used in the experiment. Referring to Equations (5.22) and (5.23), the Fourier spectrum of the impulse response function is first modeled digitally. In the theoretical part, the
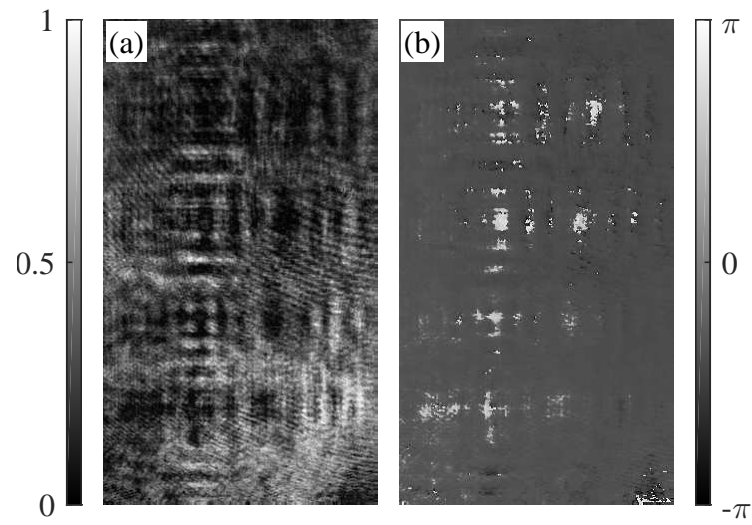
Figure 5.6: Object wavefront at the hologram plane. (a) and (b) are the normalized amplitude and the phase of the complex field, respectively.
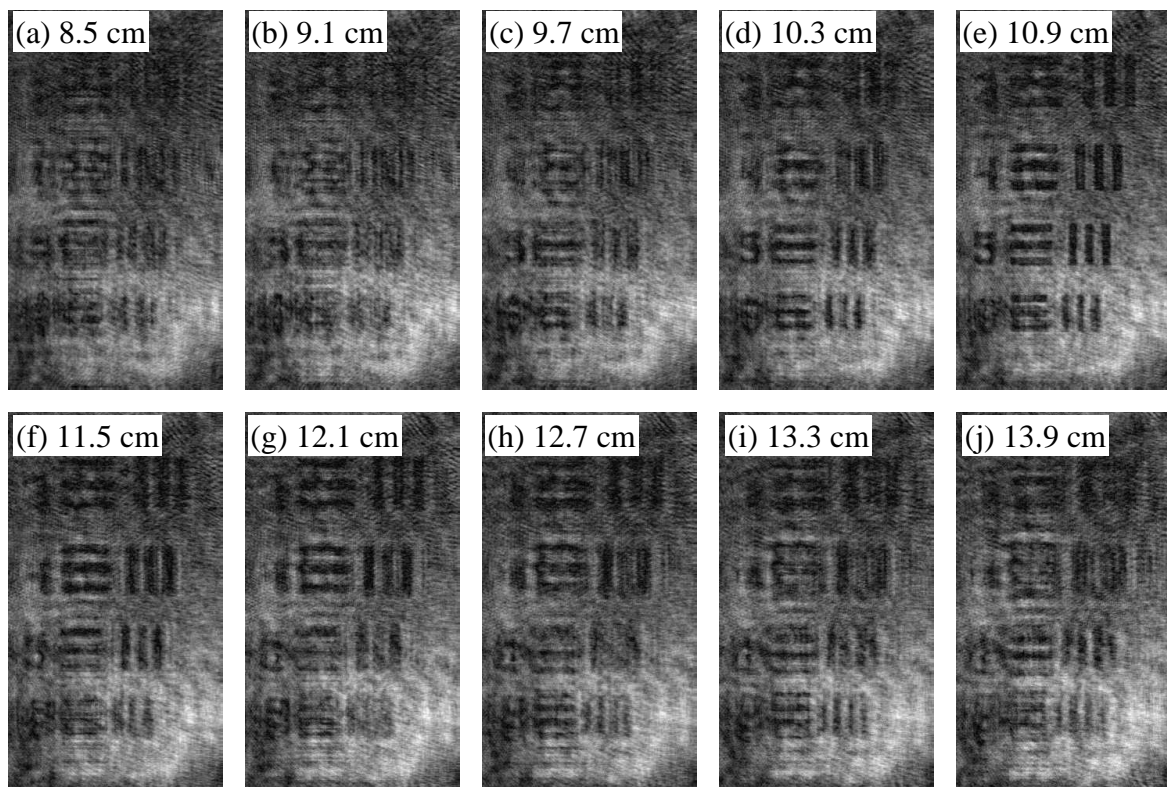

Figure 5.7: Reconstruction of the 1951 USAF Resolution Test Targets. The distance of the back propagation is shown at the top of each subfigure.

mathematics is discussed in the continuous form, whereas in the experimental part, the Fourier spectrum of the impulse response function is described pixel by pixel. Here, for a better demonstration of the reconstruction, the digitalized Fourier spectrum of the impulse response function is given:

$$G\left(m,n\right) = \exp\left[-jkd\sqrt{1 - \left(\lambda \cdot m\Delta x\right)^2 - \left(\lambda \cdot n\Delta y\right)^2}\right], \qquad (5.35)$$

where (m,n) is the pixel index, Δx and Δy are the side length of a pixel along horizontal and vertical directions, respectively. In the current demonstration, the values are specified as $\Delta x = \Delta y = 7.4$ μm.

5.4   Summary

This chapter demonstrates a phase-shifting digital holography system which is based on the DTEO phase modulator. A linearly time-varying phase shift is introduced between the object and the reference waves. The reconstruction of the digital holograms involves 1) the retrieval of the object wavefront at the hologram plane, and 2) the back propagation of the retrieved wavefront. The proposed system is configured in the in-line scheme which improves the usage efficiency of the resolution provided by the detector array.

Experiments are carried out to verify the proposed phase-shifting digital holography system. The capability of refocusing or post-focusing is illustrated, which renders the lensless imaging system. The time sequence method is used to retrieve the phase of the wavefront and the amplitude is captured directly by blocking the reference wave. The convolution method, which is also known as angular spectrum method (ASM), is adopted to calculate the back propagation of the retrieved wavefront. As a comparison to conventional holography, the proposed system provides the reconstruction which is free of the non-diffraction component and the twin image of the target. At the same time, the in-line configuration makes full use of the camera resolution.

Chapter 6

DTEO Modulator in Nomarski DIC Microscopy

Pure phase objects, such as certain transparent biological specimen, normally bring difficulties in its visualization, because it does not contribute to an intensity change when investigated under illumination. Two milestones are remarkable in the visualization of pure phase objects, namely the Zernike phase contrast imaging [126, 127] and the Nomarski differential interference contrast (DIC) microscopy. Both of the techniques are based on the coherent superposition of two waves. For Zernike phase contrast imaging, the object and the reference waves are longitudinally modified, whereas, for Nomarski DIC microscopy, no reference wave is required and the two object waves are laterally sheared. In this chapter, the focus is laid on the Nomarski DIC microscopy, in which it is possible to use the DTEO phase modulator.

The concept of differential interference contrast was first proposed and brought into microscopy by Georges Nomarski [128–130]. The two interfering object waves are identical, but laterally sheared at the observation plane. Through the coherent superposition of the laterally sheared waves, the phase gradient or differential phase distribution of the specimen is converted into the intensity variations, which gives the possibility of visualizing the pure phase object. However, for quantitative investigation and pure phase imaging, the conventional Nomarski DIC microscopy faces two major issues:

1. The intensity has a non-linear response to the phase gradient, because the intensity of the interference between the two object waves are determined by the cosine function of the differential phase distribution.

2. When the specimen is stained or light-absorbing, the intensity of the DIC image is a mixture of the absorption and the phase gradient distribution.

The two issues above hamper a more informative interpretation of the DIC image. To address the issues, the phase-shifting technique is introduced which renders the Nomarski DIC microscopy a quantitative tool for differential phase imaging.

The standard configuration of a Nomarski DIC microscope possesses a feature that the two interfering object waves propagate along essentially the same optical path, which is known as quasi-common-path configuration. The superiority of such a configuration includes the convenience of implementation and the enhancement of performance, because all the optics are collinear and the noises are canceled out. However, for phase-shifting differential interference contrast (PS-DIC) microscopy, the quasi-common-path configuration, on the other hand, restricts its access to most of the conventional phase-shift methods and devices. Qualified phase-shifting methods normally involve mechanical motion, e.g., rotating polarizing optics [131] (also see Subsection 2.2.2) and translating the differential prism [132]. In the last decade, another PS-DIC microscopy [133] emerges which is based on an off-axis configuration. The two interfering wavefronts are tilted to an extent that is sufficient to induce a detectable spatially distributed fringe. The quantitative phase gradient is then calculated from the spatial modulation. Though the spatial modulation in PS-DIC is promising, but it in return reduces the spatial resolution of the retrieved phase gradient image, because at least three pixels are required to determine a single point in the final phase gradient map [134].

In this chapter, a quantitative Nomarski DIC microscopy is described which is based on the joint spatio-temporal phase modulation. The DTEO modulator is applied to introduce the temporal phase shift, and the spatial phase shift is provided by the beam tilt. The phase gradient of the specimen is retrieved by the reference-frame-based 3-D Fourier analysis. The advantages include:

1. a joint spatio-temporal phase modulation without moving parts;

2. the flexibility of placing the specimen-related spectra in the 3-D Fourier domain;

3. a straightforward variation in the shear by an axial sliding differential prism;

4. a residual-free differential phase retrieval by reference frame.

The useful basics of the PS-DIC microscopy are first introduced in Section 6.1. The optical configuration is demonstrated in Section 6.2, in which the operation principle and the adjustable shear are described as well. The reference-frame-based 3-D Fourier analysis [135–137] is illustrated together with the experiments in Section 6.3, where a single-mode fiber and a bio-sample, i.e., the forewing of a honey bee, are imaged. Typical distributions of the phase gradient from the specimens are shown at different shears. Section 6.4 gives a summary to the current chapter.

6.1 Basics in PS-DIC Microscopy

Though there are several distinct models describing the DIC images, the PS-DIC adopts the geometric DIC imaging model to interpret the image formation [138]. The geometric DIC imaging model assumes that the specimen is coherently illuminated by a monochromatic plane wave. The optical configuration of a conventional DIC microscope is considered for the demonstration [139], as shown in Figure 6.1.
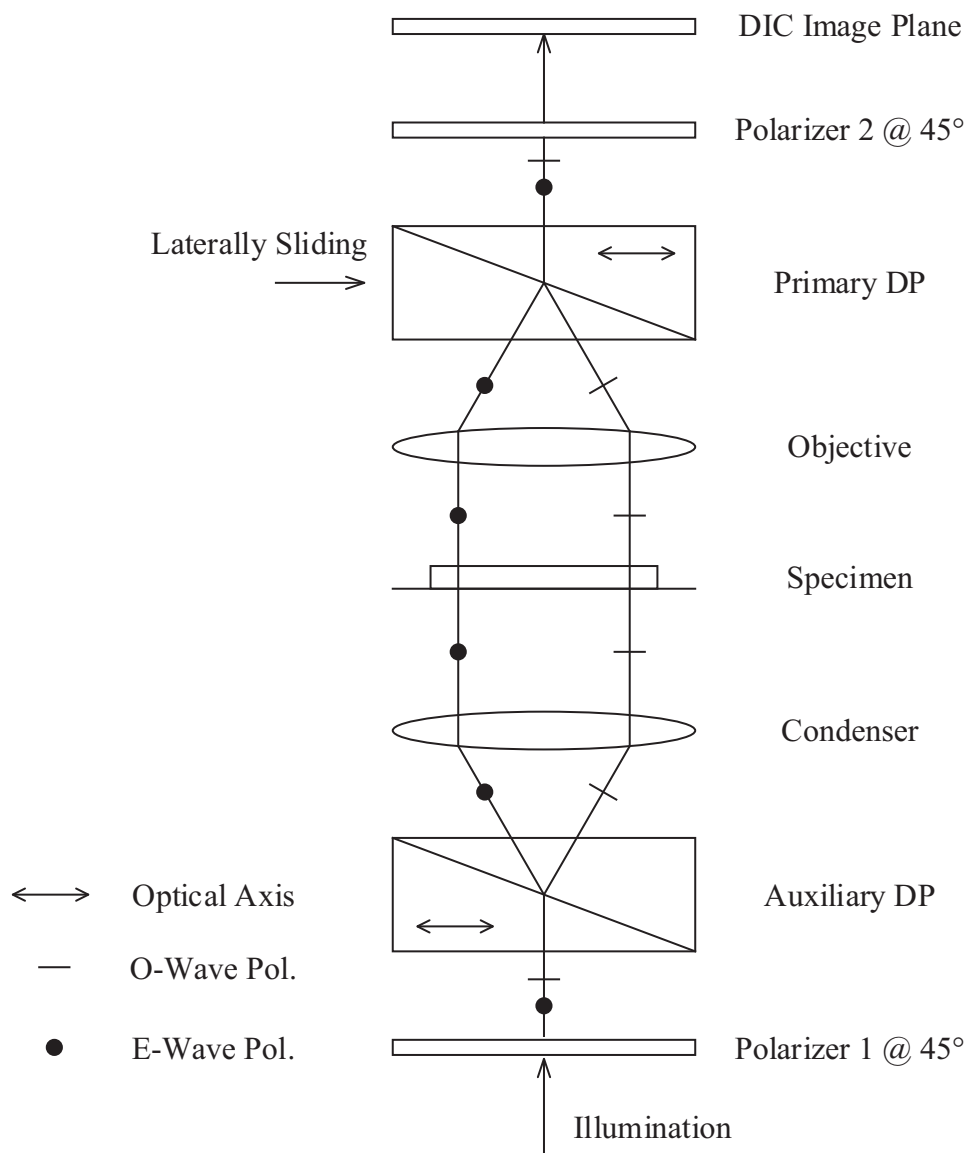
Figure 6.1: Optical configuration of a basic DIC microscope. DP: differential prism.

6.1.1   DIC Image Formation

Referring to Figure 6.1, the basic and key components of the DIC microscope are a microscope objective, an eyepiece, and a differential prism which is normally a Wollaston prism. Analogous to conventional microscopes, when the illumination is in a form of a divergent beam, a condenser is used to gather the light. In this case, an auxiliary differential prism is further required for the DIC microscope to make full use of the condenser aperture. As a result, the overall brightness of the DIC image is enhanced. For completeness, all the components are introduced in this section. In the following sections, only the basic components are considered, because the illumination in the present study is provided by a laser. No light gathering and brightness issues are involved. A polarizer is used to produce the necessary polarized illumination. The allowed polarization direction of the polarizer is aligned to 45° with respect to the optical axis of the auxiliary differential prism, so that the illumination wave is separated equally in intensity by the auxiliary differential prism. The condenser is placed behind the auxiliary differential prism at a distance of its focal length. The specimen is then illuminated with two laterally sheared plane waves. The primary differential prism is positioned at the rear focal point of the microscope objective to recombine the two sheared waves. A second polarizer is installed behind the objective to force the two orthogonal polarizations interfere with each other. The combined waves pass through the eyepiece and the DIC image is formed at the image plane. The interference between the waves from an object point and its neighborhood point gives rise to the contrast in the DIC image of a transparent phase object. The intensity is determined by the phase difference between the two interfering object waves.

6.1.2   Bias Retardation

The bias retardation is introduced in the DIC microscope by the primary differential prism [140]. A distinct bias retardation is implemented by laterally sliding the prism. In terms of the phase in the interference, the change in the bias retardation shifts the phase between the two interfering object waves. From the view of intensity, a change in the bias retardation moves the 0 order interference fringe. In this subsection, the bias retardation is demonstrated by taking a Wollaston prism as the primary differential prism.

The Wollston prism is composed of two quartz wedges (uniaxial birefringent crystal), the optical axes of which are perpendicular to each other, as shown in Figure 6.2. With respect to the optical axis of the Wollaston prism, a 45°-polarized incident wave that enters the prism is split into two orthogonal waves, which are known as the ordinary and the extraordinary waves, respectively. The two orthogonal waves propagate along different directions resulting in a beam separation in space. The split angle at the output
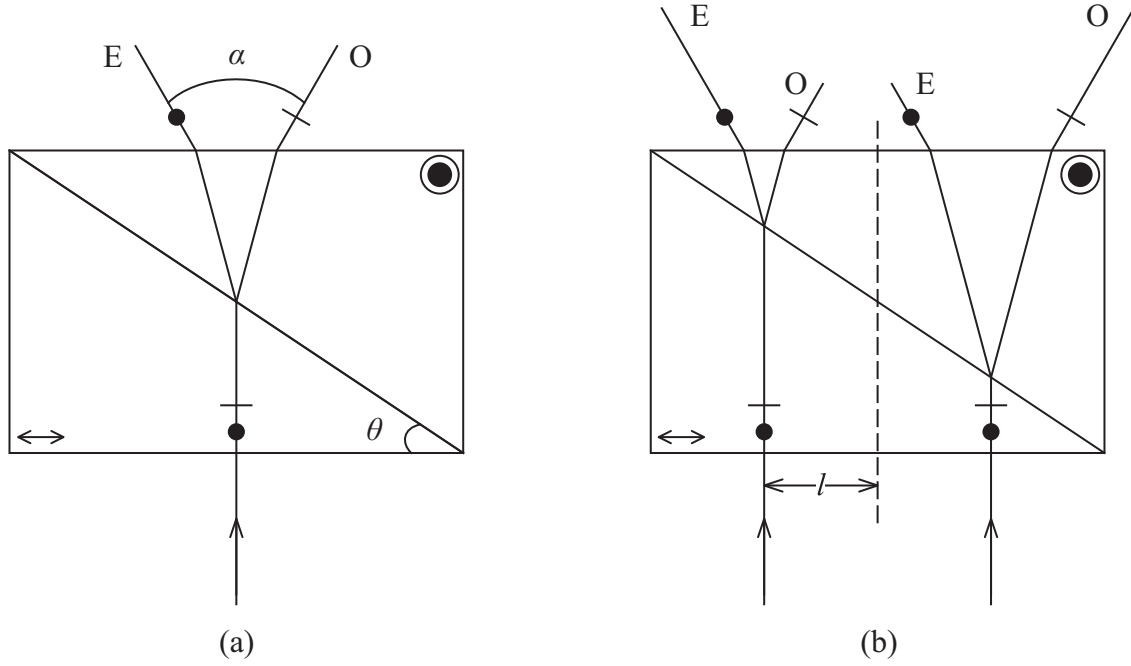
Figure 6.2: Physical principle of a Wollaston prism; (a) shows the wave split process and (b) shows the incidence-dependent OPD between the two separated waves.

end is calculated by [141]

$$\alpha = 2\left(n_e - n_o\right)\tan\theta, \tag{6.1}$$

where n_e and n_o are the refractive indices of the extraordinary and the ordinary waves, respectively, and θ represents the wedge angle. The OPD between the two separated waves is dependent on the incident point [26], denoted by

$$OPD = 2\left(n_e - n_o\right)l \cdot \tan\theta = \alpha \cdot l, \tag{6.2}$$

where l represents the geometric length from the incident point to the geometric median of the prism. It is noted that Equations (6.1) and (6.2) are concluded under normal incidence. The aforementioned bias retardation is a description of the OPD in terms of phase, denoted by

$$\varphi_{bias} = \frac{2\pi \cdot OPD}{\lambda} = \frac{2\pi\alpha l}{\lambda}. \tag{6.3}$$

When the incident wave enters the prism at the geometric median, namely $l = 0$, the thicknesses of the two wedges are identical. The OPD and the bias retardation are zero in this case. Particularly, it is possible to modify the bias retardation by sliding the prism laterally, which is equivalent to a change in the incident point. For the general description,

the object wavefronts at the image plane are denoted by

$$\widetilde{U}_{1,2}\left(\boldsymbol{\rho}\right) = A\left(\boldsymbol{\rho} \pm \Delta\boldsymbol{\rho}/2\right) \cdot \exp\left[\phi\left(\boldsymbol{\rho} \pm \Delta\boldsymbol{\rho}/2\right) \pm \varphi_{bias}/2\right], \tag{6.4}$$

where the plus and the minus signs apply for the subscripts 1 and 2, respectively, A represents the amplitude, ϕ stands for the object phase, and $\Delta\boldsymbol{\rho}$ is the shear. The DIC intensity distribution which results from the interference is described by

$$I\left(\boldsymbol{\rho}\right) = \left[\widetilde{U}_1 + \widetilde{U}_2\right] \cdot \left[\widetilde{U}_1 + \widetilde{U}_2\right]^* = I_0 + I_c \cdot \cos\left(\phi_1 - \phi_2 + \varphi_{bias}\right), \tag{6.5}$$

with

$$\phi_1\left(\boldsymbol{\rho}\right) = \phi\left(\boldsymbol{\rho} + \Delta\boldsymbol{\rho}/2\right), \tag{6.6a}$$
$$\phi_2\left(\boldsymbol{\rho}\right) = \phi\left(\boldsymbol{\rho} - \Delta\boldsymbol{\rho}/2\right). \tag{6.6b}$$

The intensity distribution given by Equation (6.5) provides only a qualitative observation of the specimen, which is a mix of the object amplitude, the object phase, and the bias retardation. By considering the geometric model described in Equation (6.5), it is concluded that a phase shift is readily introduced by laterally sliding the prism, namely changing the incident point. Thus, a PS-DIC microscope is configured and the pure phase gradient distribution is calculated by phase-shifting algorithms. As a result, a quantitative investigation to the specimen is accomplished.

6.2   Optical Configuration

In this section, the present quantitative PS-DIC microscopy is described, which is based on the joint spatio-temporal phase modulation. The optics is presented in a minimum configuration to lay the focus on the phase modulation. Specifically, the condenser and the auxiliary differential prism are dropped, because a collimated laser beam is used as the illumination. No light gathering and brightness issues are involved in this case. The optical configuration is shown in Figure 6.3.

The laser provides the linearly polarized illumination and a HWP is used to orient the input polarization conveniently. The laser beam travels through the DTEO phase modulator which is composed of the powered-up LN crystal and the QWP. The temporally modulated beam is collimated by two lenses L1 and L2 which are configured as a Kepler telescope. The collimated beam then illuminates the specimens. The light from the specimen is first imaged at the intermediate plane IP through the microscope objective MO. The lens L3, which serves as the eyepiece, further images the specimen from the inter-
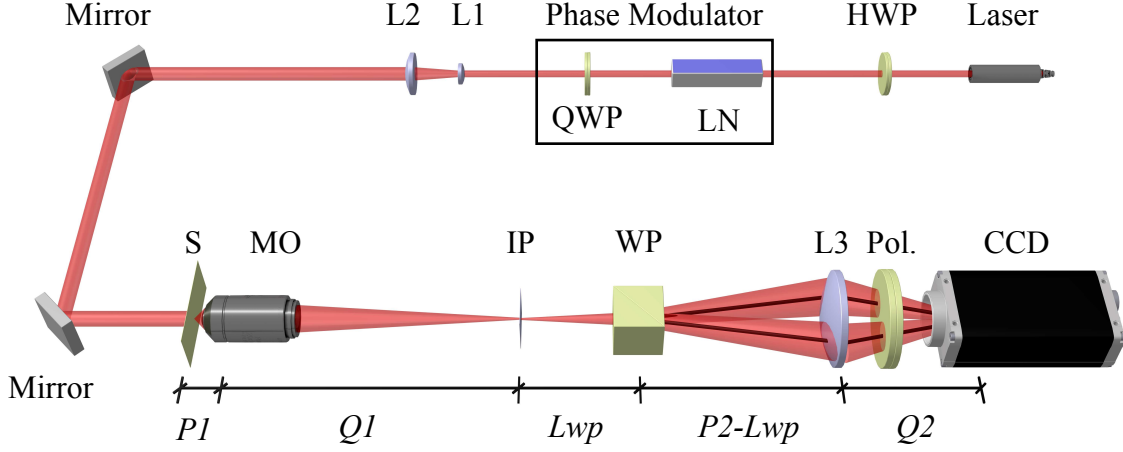
Figure 6.3: Optical configuration of the quantitative PS-DIC microscope.

mediate plane IP to the final image plane. The DIC intensity distribution is captured by a CCD camera which is placed at the final image plane. A Wollaston prism is inserted between the objective MO and the lens L3 to generate two laterally sheared object waves. In front of the CCD camera, a polarizer is placed to force the two orthogonal object waves interfere with each other. The labels at the bottom in italic represent the corresponding distances.

6.2.1 Joint Spatio-Temporal Phase Modulation

To demonstrate the joint spatio-temporal phase modulation, a Cartesian coordinate system is established with the left hand rule. Because there are two directing mirrors, the coordinate is built up with respect to the laser beam. Specifically, the positive z-axis points along the direction of the laser beam propagation and the x-axis along the direction of the beam split. Assuming that the laser beam at the entrance of the DTEO phase modulator is x-polarized. Under the function of the DTEO phase modulator, the temporally modulated wave is denoted by

$$\underbrace{\begin{bmatrix} V_x \\ V_y \end{bmatrix}}_{\text{Output}} = \underbrace{\begin{bmatrix} 1 & j \\ j & 1 \end{bmatrix}}_{\text{QWP}} \underbrace{\begin{bmatrix} j\cos\omega t & j\sin\omega t \\ j\sin\omega t & -j\cos\omega t \end{bmatrix}}_{\text{Powered-up LN}} \underbrace{\begin{bmatrix} \exp\left(-j\omega_0 t\right) \\ 0 \end{bmatrix}}_{\text{Input } V_{in}} = \begin{bmatrix} \exp\left[j\left(-\omega_0+\omega\right)t+\frac{\pi}{2}\right] \\ \exp\left[j\left(-\omega_0-\omega\right)t\right] \end{bmatrix}, \quad (6.7)$$

where j is the imaginary unit, ω represents the angular frequency of the crystal's driver, ω_0 stands for the optical frequency, and t is the time parameter. The optical axis of the Wollaston prism is aligned to the x-axis, so that the two output components, V_x and

V_y, act as the extraordinary and the ordinary waves inside the prism. Consequently, the separated waves possess distinct frequencies which are $\omega_0 + \omega$ and $\omega_0 - \omega$, respectively. Considering the bias retardation in Subsection 6.1.2, the time-dependent phase difference between the two separated components, V_x and V_y, are equivalent to a continuous shift in the bias retardation, but without any mechanical motion unit.

The spatial phase modulation is provided directly from the DIC microscope at the condition of a sufficient tilt between the two interfering object waves. For a clear illustration of the spatial phase modulation, the intermediate plane IP, the Wollaston prism WP, the lens L3, and the final image plane are considered separately from the whole setup, as shown in Figure 6.4. The paraxial condition and an identical polarization are assumed
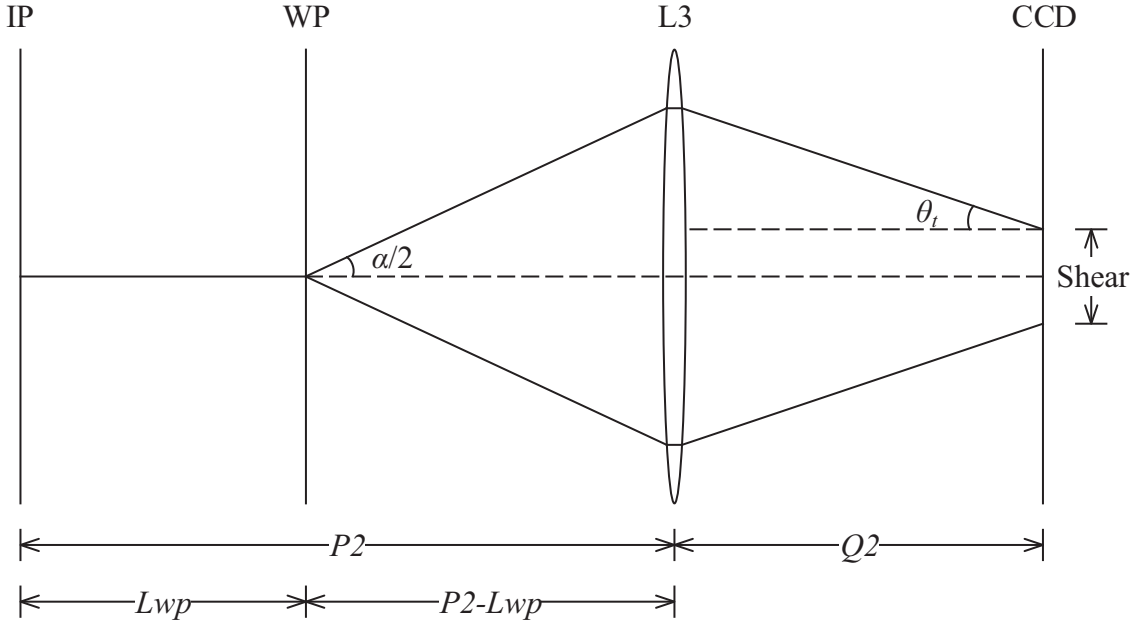
Figure 6.4: Formation of the spatial phase modulation and the adjustable shear.

for the following description. The object and the image distances, $P2$ and $Q2$, satisfy the thin lens formula, denoted by

$$\frac{1}{P2} + \frac{1}{Q2} = \frac{1}{f},$$
(6.8)

where f is the focal length of the lens L3. According to the geometry, the tilt angle of the object wave that impinges on the CCD plane is calculated by [142]

$$\tan \theta_t = \frac{P2 - Lwp - f}{f} \cdot \tan \frac{\alpha}{2},$$
(6.9)

where θ_t represents the tilt angle and α stands for the split angle provided by the Wollaston prism. Considering the paraxial condition [120], Equation (6.9) is simplified as

$$\theta_t = \frac{\alpha\,(P2 - Lwp - f)}{2f}. \tag{6.10}$$

Assuming that the operating wavelength is λ, the spatial phase modulation is expressed as a set of fringes. The spatial frequency of the spatial phase modulation is given by

$$f_{sp}\,(Lwp) = \frac{2\sin\theta_t}{\lambda} = \frac{\alpha\,(P2 - Lwp - f)}{\lambda f}. \tag{6.11}$$

Now, both the temporal and the spatial phase modulations are taken into account. The two laterally sheared wavefronts at the CCD plane are described by

$$\begin{aligned}
\widetilde{U}_1\,(\boldsymbol{\rho},t) &= A_1 V_x \exp\left\{j\left[\phi\left(\boldsymbol{\rho} + \tfrac{\Delta\boldsymbol{\rho}}{2}\right) + \pi f_{sp}x\right]\right\} \\
&= A_1 \exp\left\{j\left[\phi\left(\boldsymbol{\rho} + \tfrac{\Delta\boldsymbol{\rho}}{2}\right) + \pi f_{sp}x + \omega t\right]\right\},
\end{aligned} \tag{6.12a}$$

$$\begin{aligned}
\widetilde{U}_2\,(\boldsymbol{\rho},t) &= A_2 V_y \exp\left\{j\left[\phi\left(\boldsymbol{\rho} - \tfrac{\Delta\boldsymbol{\rho}}{2}\right) - \pi f_{sp}x\right]\right\} \\
&= A_2 \exp\left\{j\left[\phi\left(\boldsymbol{\rho} - \tfrac{\Delta\boldsymbol{\rho}}{2}\right) - \pi f_{sp}x - \omega t\right]\right\},
\end{aligned} \tag{6.12b}$$

where the constant phase difference $\pi/2$ between V_x and V_y is dropped and the Wollaston prism is assumed providing the beam split along the x-axis. It is shown in Equation (6.12) that the phase of each split wave is modulated, both spatially (f_{sp}) and temporally (ω).

6.2.2 Adjustable Shear

The shear in the DIC microscopy determines the sensitivity of the system. An adjustable shear provides the possibility of imaging the specimen at different sensitivities. In the present PS-DIC microscopy, the adjustable shear is introduced by axially sliding the Wollaston prism. Referring to Figure 6.4 once again, the shear is geometrically given by

$$\text{Shear } \Delta\boldsymbol{\rho} = \alpha\left[P2 - Lwp - \frac{Q2}{f}\,(P2 - Lwp - f)\right]. \tag{6.13}$$

When the Wollaston prism slides axially, the distance Lwp alters and further the shear is changed according to Equation (6.13). It is noted that Equation (6.13) is true, when the intermediate image exists. If the microscope objective MO and the lens L3 are configured as a $4f$ system, the axial position of the Wollaston prism does not control the shear any longer. The reason is that each lens acts as a Fourier transform engine in a $4f$ system. The wave tilt induced by the Wollaston prism is equivalent to a modification of the spatial Fourier spectrum from the specimen, which means a linear phase distribution is added to

the spatial Fourier spectrum. The additional phase distribution is proportional to the half angle of the wave split of the Wollaston prism, which is not influenced by the position of the prism. In terms of effect, the additional phase distribution shifts up/down the image at the final image plane. Though the two images are still mutually sheared, the amount of shear is constant.

6.3   Experiments and Results

In order to give a clear and detailed illustration to the feasibility and the adjustable shear of the present PS-DIC microscope, a single-mode fiber is first imaged, because of its simple phase distribution. The second experiment involves imaging a biological specimen which is the forewing of a honey bee. The present PS-DIC microscope is configured as illustrated in Figure 6.3. All the experiments are carried out with the same configuration except for the shear. Regarding the light source, the DTEO modulator, and the CCD camera, the basic information is shown in the list in Subsection 3.2.2. The specific settings of the PS-DIC are listed below:

- Microscope objective MO: Leica HI PLAN EPI

    - N.A.= 0.40;

    - Magnification: 20×;

- Wollaston prism:

    - Clear aperture: ∅ 10 mm;

    - Beam separation angle: 1° at 633 nm;

- Lenses:

    - Focal length: L1 = 5 mm; L2 = 40 mm; L3 = 60 mm;

- Array detector: CCD camera, Basler piA640-210gm

    - Frame rate: 136 fps;

    - Region of interest: 402 px × 536 px;

    - Pixel size: 7.4 μm × 7.4 μm;

    - Pixel bit depth: 8 bits;

The setup is calibrated by a positive 1951 USAF resolution test target. The acquisition time is two seconds and 272 frames of the phase-shifted DIC images are captured. The first experiment is conducted with a single-mode fiber. One of the captured frames is

shown in Figure 6.5(a). The inset gives a zoomed-in illustration of the fringe structure,
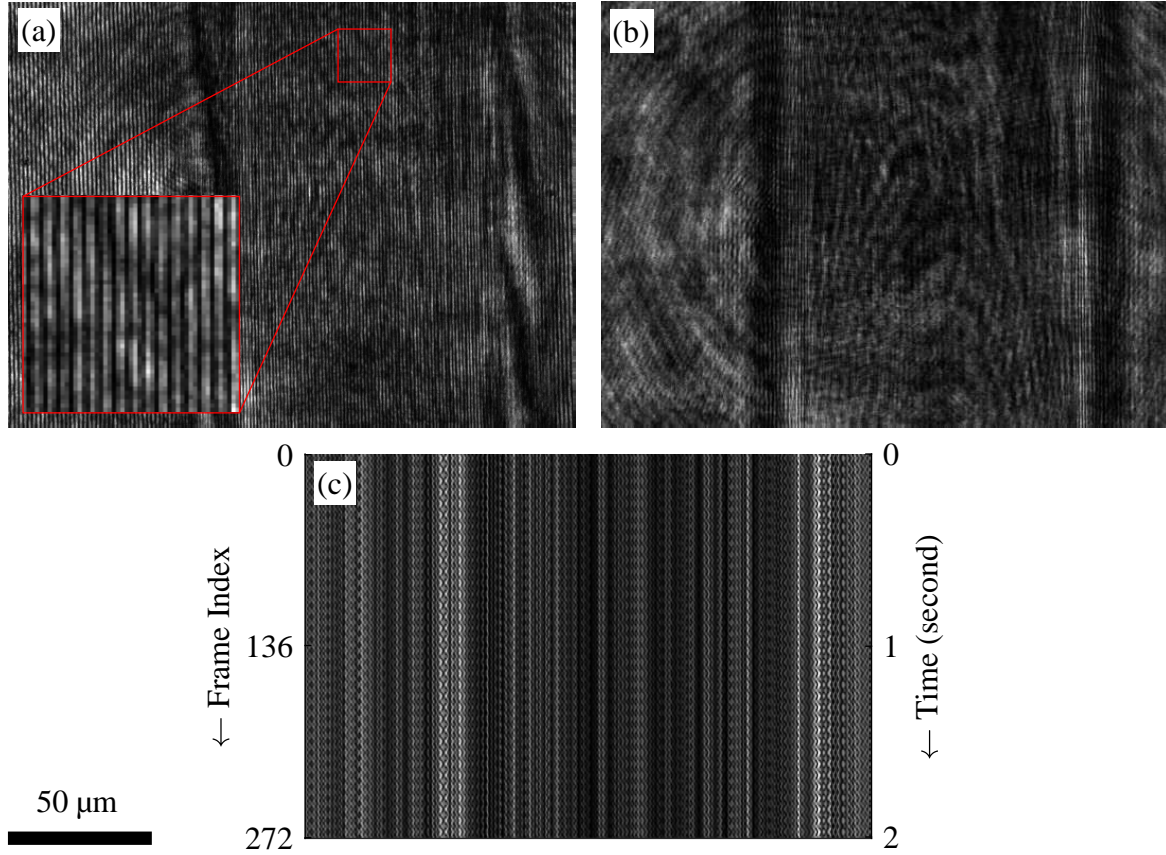
Figure 6.5: Captured frames. (a) An example of the PS-DIC image. The inset is a zoomed-in illustration of the fringe structure. (b) Bright field image. (c) Temporal intensity evolution history of the image cube.

which is the expression of the spatial phase modulation. As a comparison, the bright field image is also provided in Figure 6.5(b). The bright field image is captured by using the same microscope but without the Wollaston prism. To illustrate the temporal phase modulation, the temporal intensity evolution history of the 244th row of pixels from all the captured 272 frames is shown in Figure 6.5(c). The periodical variation indicates the temporal phase modulation. Recalling the wavefronts described by Equation (6.12), the collected image cube is denoted mathematically by

$$I\left(\boldsymbol{\rho},t\right)=\left[\widetilde{U}_1\left(\boldsymbol{\rho},t\right)+\widetilde{U}_2\left(\boldsymbol{\rho},t\right)\right]\left[\widetilde{U}_1\left(\boldsymbol{\rho},t\right)+\widetilde{U}_2\left(\boldsymbol{\rho},t\right)\right]^*=A_1^2+A_2^2+A_1A_2\cos\left[\Phi_O\left(\boldsymbol{\rho},t\right)\right], \quad (6.14)$$

with

$$\Phi_O\left(\boldsymbol{\rho},t\right)=\underbrace{\phi\left(\boldsymbol{\rho}+\tfrac{\Delta\boldsymbol{\rho}}{2}\right)-\phi\left(\boldsymbol{\rho}-\tfrac{\Delta\boldsymbol{\rho}}{2}\right)}_{\text{diff. phase distribution}}+\underbrace{2\pi f_{sp}x+2\omega t}_{\text{joint modulation}}+\underbrace{\varphi_1-\varphi_2}_{\text{residuals}}. \quad (6.15)$$

To show the residual free algorithm, in the present discussion, the residual of the measurement is considered. The origin of the residual phase is the aberrations and misalignments of the setup.

In order to retrieve the differential phase distribution of the specimen from the joint modulation, the 3-D Fourier fringe analysis method is adopted, which is an extension of the conventional 2-D Fourier transform. The 3-D image cube is first converted into the 3-D spatio-temporal frequency domain by applying the 3-D Fourier transform, as shown in Figure 6.6. For clarity, Figure 6.6(a) and (b) show the spatial and the temporal carrier
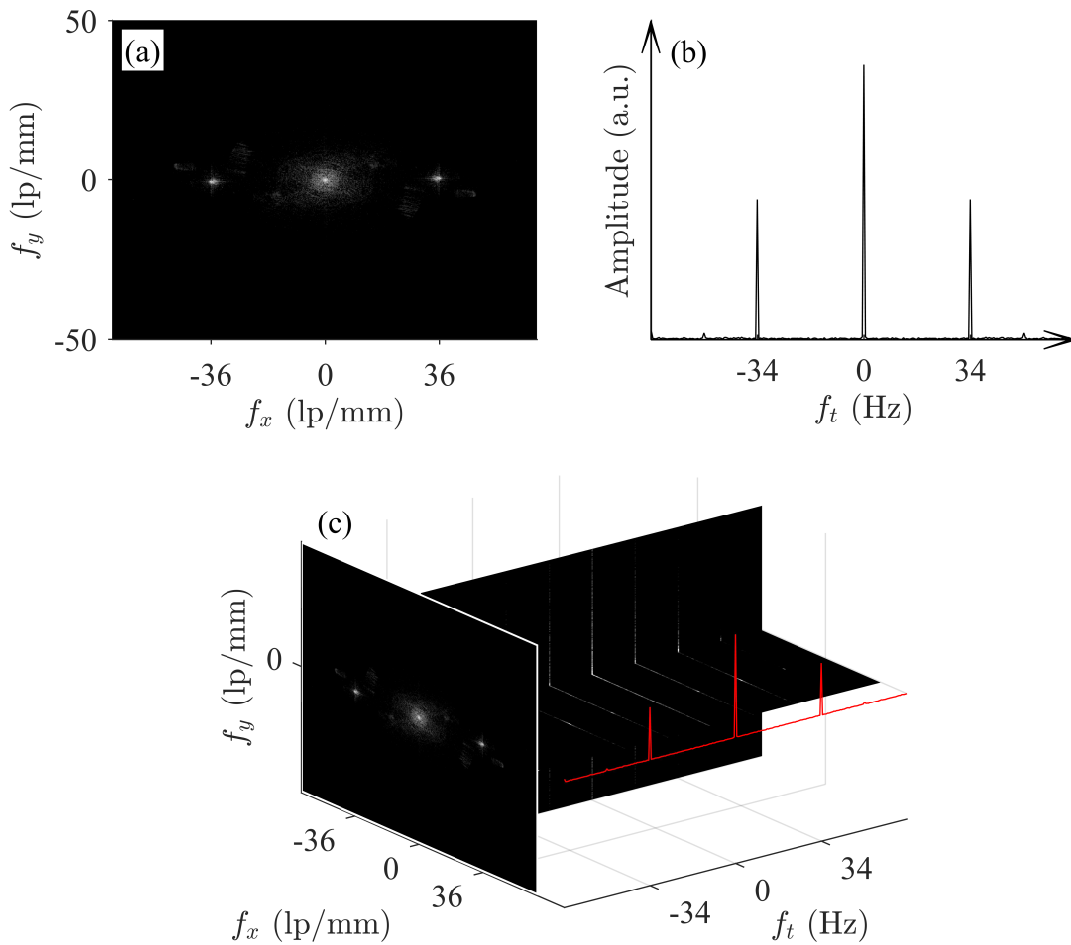
Figure 6.6: 3-D spatio-temporal Fourier frequency spectrum. (a) 2-D slice of the frequency cube (two spatial frequency axes). (b) 1-D line of the frequency cube (temporal frequency axis). (c) 3-D frequency cube.

frequencies, respectively, and the 3-D frequency cube is shown in Figure 6.6(c). It is found that the joint spatio-temporal phase modulation is expressed as a 3-D frequency carrier which is located around (36 lp/mm, 0, 34 Hz) in the frequency cube. Regarding

the temporal component of the carrier frequency, there is no shift nor broadening, which indicates that the specimen is a stationary target. For the spatial component, the shift and the broadening result from the spatial distribution of the specimen.

As is demonstrated previously in Subsection 2.1.2, the Fourier transform based phase retrieval algorithms involve an operation of translating the isolated +1 order spectrum towards the origin. In the proposed PS-DIC microscopy, rather than the spectrum translation, a set of reference frames is captured without the presence of the specimen. Thus, a reference-frame-based 3-D Fourier analysis is applied for a residual-free phase retrieval. The side lobe translation method has the best performance, when the spatio-temporal carrier frequency is an integer multiple of the sampling interval in both space and time domains. However, in practice, the carrier frequency is generally not an integer multiple of the discrete frequency interval and falls between neighboring discrete frequency points in the discrete spectrum domain. Therefore, a fractional carrier frequency component (called leakage) remains as a small tilt after the +1 order spectrum being shifted by an integer multiple of the frequency interval to the origin. By applying the reference-frame-based 3-D Fourier analysis, the frequency leakage effect mentioned above is essentially avoided.

To isolate the +1 order spectrum, the frequencies around (36 lp/mm, 0, 34 Hz) are first filtered out and then the inverse Fourier transform is directly applied to the isolated +1 order spectrum without the spectrum translation. The obtained complex function is denoted by

$$c_O\left(\boldsymbol{\rho},t\right) = A_1 A_2 \exp\left\{j\left[\varPhi_O\left(\boldsymbol{\rho},t\right)\right]\right\}. \tag{6.16}$$

Similarly, the complex function of the image cube of the reference frames is calculated by an identical procedure, which is given by

$$c_R\left(\boldsymbol{\rho},t\right) = A_1 A_2 \exp\left\{j\left[\varPhi_R\left(\boldsymbol{\rho},t\right)\right]\right\}, \tag{6.17}$$

with

$$\varPhi_R\left(\boldsymbol{\rho},t\right) = \underbrace{2\pi f_{sp}x + 2\omega t}_{\text{joint modulation}} \underbrace{+\varphi_1 - \varphi_2}_{\text{residuals}}. \tag{6.18}$$

The differential phase distribution of the specimen is retrieved by

$$\arctan\left\{\frac{\operatorname{Im}\left[c_O\left(\boldsymbol{\rho},t\right)c_R^*\left(\boldsymbol{\rho},t\right)\right]}{\operatorname{Re}\left[c_O\left(\boldsymbol{\rho},t\right)c_R^*\left(\boldsymbol{\rho},t\right)\right]}\right\} = \phi\left(\boldsymbol{\rho}+\tfrac{\Delta\boldsymbol{\rho}}{2}\right) - \phi\left(\boldsymbol{\rho}-\tfrac{\Delta\boldsymbol{\rho}}{2}\right) \approx \frac{\partial\phi\left(\boldsymbol{\rho}\right)}{\partial x}\cdot\Delta\boldsymbol{\rho}, \tag{6.19}$$

where the item right behind the equal sign is the differential phase distribution, and the partial derivative is the phase gradient of the specimen. The approximation holds when the shear is small compared to the highest spatial frequency of the specimen.

By applying the reference-frame-based 3-D Fourier analysis, the differential phase distribution of the single-mode fiber is retrieved, as shown in Figure 6.7. In Figure 6.7(a) and
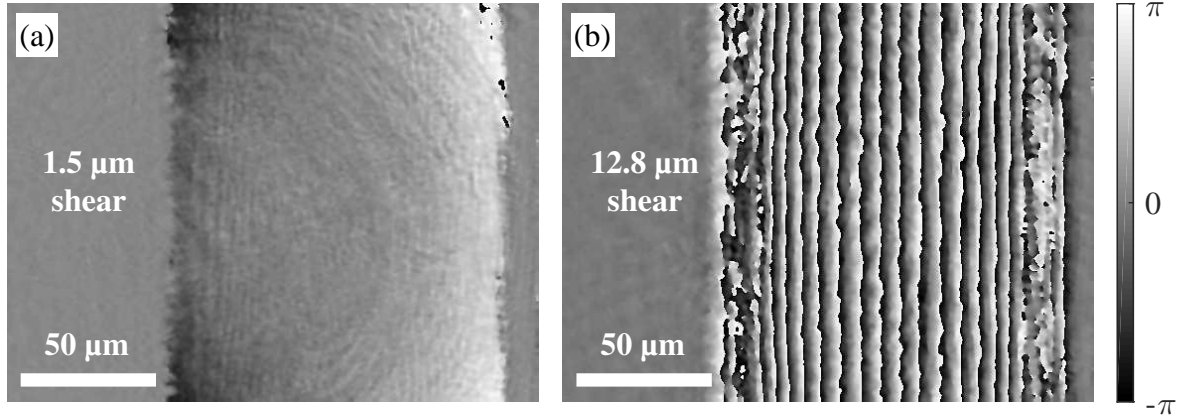

Figure 6.7: Retrieved differential phase map of a single-mode fiber. The shear in (a) and (b) are 1.5 μm and 12.8 μm, respectively.

(b), the experiments are carried out at 1.5 μm shear and 12.8 μm shear, respectively. As is illustrated previously, the shear determines the sensitivity of the system. Considering that the same fiber is imaged in Figure 6.7(a) and (b), the density of the fringe of the wrapped differential phase distribution increases when the shear is enlarged. At the edge of the fiber, the image becomes blurry. The reason is that in Figure 6.7(b) the sensitivity is too high for the current specimen. The maximum capacity of the wrapped phase density at the CCD plane is determined by the shear, denoted by

$$\left. \frac{\partial^2 \phi\left(\boldsymbol{\rho}\right)}{\partial x^2} \right|_{\text{max}} = \frac{\pi}{\Delta\boldsymbol{\rho} S_p}, \tag{6.20}$$

where S_p is the pixel size along the shear direction of the CCD camera. Equation (6.20) is deduced from the fact that, for a fully resolved phase retrieval, a spatial phase variation of 2π must cover at least two pixels. Otherwise, due to the phase is wrapped, two neighboring phase fringes are not able to be distinguished. Considering the current configuration, the maximum phase gradient variations that is supported by the two shears are

$$\left. \frac{\partial^2 \phi\left(\boldsymbol{\rho}\right)}{\partial x^2} \right|_{\text{max at } \Delta\boldsymbol{\rho} = 1.5 \ \mu m} = \frac{\pi}{1.5 \ \mu m \times 7.4 \ \mu m} \approx 0.0901\pi \ \mu m^{-2}, \tag{6.21a}$$

$$\left. \frac{\partial^2 \phi\left(\boldsymbol{\rho}\right)}{\partial x^2} \right|_{\text{max at } \Delta\boldsymbol{\rho} = 12.8 \ \mu m} = \frac{\pi}{12.8 \ \mu m \times 7.4 \ \mu m} \approx 0.0106\pi \ \mu m^{-2}. \tag{6.21b}$$

The second experiment is conducted with the forewing of a honey bee to demonstrate the imaging ability for irregular biological specimen. The imaging area at the specimen

plane is 180 μm × 240 μm. The shear is adjusted to 3.3 μm. Under such a configuration, the supported maximum phase gradient variation rate is $\sim 0.0410\pi$ μm^{-2}. The retrieved differential phase distribution is shown in Figure 6.8. It is noted that the magnification
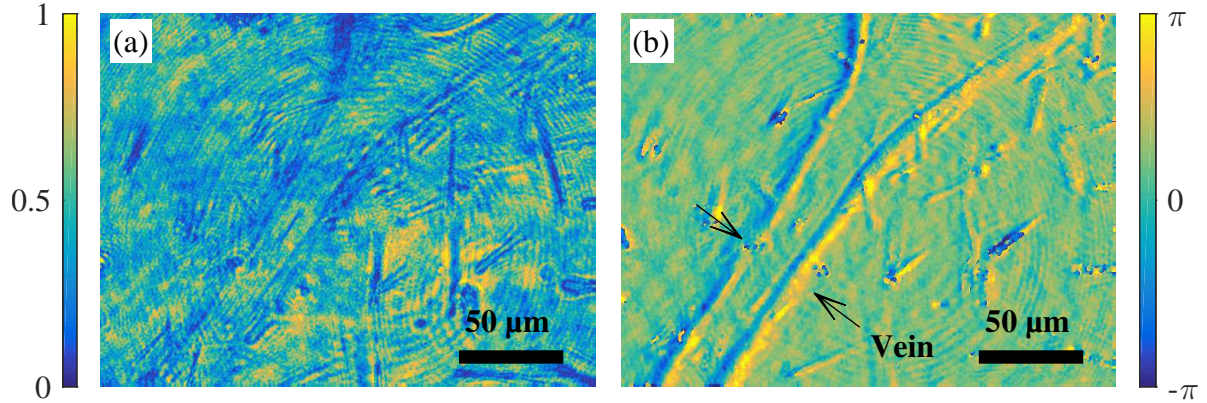

Figure 6.8: Images of the forewing of a honey bee. (a) Enhanced bright field image. (b) Quantitative differential phase image.

is different from the previous experiment, which is indicated by the scale bar. In Figure 6.8(a), the bright field image is first shown, which is enhanced in the contrast, to have a fair comparison with the quantitative DIC image shown in Figure 6.8(b). The singularity areas in the quantitative DIC image indicate where the phase is wrapped due to the arctangent function. The medial vein in the forewing is clearly visualized in the quantitative DIC image, whereas in the bright field image, the medial vein is presented in a low contrast. As for the wing hairs, it is not so hard to distinguish them among the others, even in the bright field image. The reason is that the wing hairs are actually not a pure phase object. They also contribute to an intensity change when illuminated.

6.4 Summary

In this chapter, a quantitative Nomarski PS-DIC microscopy is proposed. The phase shift is introduced by a joint spatio-temporal phase modulation. The spatial component of the carrier frequency is generated by the tilt between the two interfering waves, as long as the tilt is sufficient. The temporal component is provided by the present DTEO modulator. The introduced temporal component is equivalent to that is introduced by shifting the bias retardation of the DIC microscope, but without any mechanical moving parts.

Regarding the phase retrieval algorithm, the reference-frame-based 3-D Fourier fringe analysis is applied to the captured image cubes. Thus, the residual phase in the system is removed. More importantly, the frequency leakage effect is eliminated essentially. It

is straightforward to control the shear in the proposed DIC microscopy by setting the axial position of the Wollaston prism. The proposed optical configuration, as well as the associate phase retrieval algorithm, is experimentally verified. The experiments are carried out with a single-mode optical fiber and the forewing of a honey bee. Typical differential phase distributions are presented in the experimental verification.

Chapter 7

Conclusion and Outlook

The present study is mainly motivated by the demands in a versatile phase modulator for distinct interferometric systems. A novel dual transverse electro-optic (DTEO) phase modulator is proposed. As its name indicates, the physical principle of the modulator is based on the dual transverse electro-optic effect. The term, dual transverse, reveals the configuration, in which two orthogonal sinusoidal electric fields are applied to the electro-optic crystal. Here, the fields are orthogonal, which are expressed in terms of both time and space. Specifically, in the time domain, the two applied fields have a phase delay of $\pi/2$. Meanwhile, in the space domain, the electric field lines of them are mutually perpendicular. A revised electro-optic coefficient is adopted to run the phase modulator within the frame rate of most array detectors. As a subsequent benefit, the half-wave voltage is lowed down by the introduction of such a revised electro-optic coefficient. The related derivations in physics and mathematics are described in detail.

The features of the propose DTEO phase modulator include:

1. The phase modulator is installed in the main optical path prior to the beam splitter.

2. The two interfering waves are phase shifted simultaneously and locally.

3. The adjustable operating frequency satisfies the frame rates of most array detectors.

4. No mechanical motion unit is involved during the phase modulation.

In fact, the features above are nothing new to the existing phase modulators, which are used in the optical interferometric systems. However, there are barely any reported modulators that possess all the four features at a time. The proposed DTEO phase modulator, on the other hand, accomplishes such a demand. By covering the four features

in a single individual device, the proposed DTEO phase modulator has the capability of being applied in diverse interferometric systems.

As an opponent, the conventional electro-optic (EO) phase modulator, which is based on the single transverse EO effect, is well established. It has a broad range of applications, including the educational demonstrations, academic studies, and industrial solutions. A further advantage of the proposed DTEO phase modulator is rendered by a comparison with the conventional EO modulator, namely the input requirement and the output performance. It is a consensus that, in practical implementations, signals in the linear form or sinusoid are preferred, because they bring convenience to the signal generation or further uses of the signal. The conventional EO phase modulator has a linear response to its input, which means the output signal follows the input. The sinusoidal input gives a sinusoidal phase shift. The generated intensity change in the Bessel form brings difficulties in the data analysis. For conventional EO phase modulators, a linear input seems capable to induce a linear phase shift, but in practice it is not possible to run the driving linear signal to infinity. Interrupts and resets are necessary which smash the time domain continuity of the phase modulation, especially for time-dependent systems. In the case of the DTEO phase modulator, it is shown that the driving signal is sinusoidal, in the meantime, the output phase shift is linear. In other words, a linear phase shift is generated under a sinusoidal driving signal. Regarding the phase-shifting interference, the linear phase shift results in a sinusoidal variation in intensity. The analytical investigations of the sinusoidal-variation interference are straightforward.

The proposed DTEO phase modulator is first verified experimentally in a Michelson interferometer. The feasibility is confirmed by the periodical intensity evolution history of the temporal interference pattern. The linear time-varying phase shift is achieved. The resulting frequency of the interference intensity variation is 34 Hz, which satisfies the frame rate of most commercial cameras. In order to demonstrate the compatibility, the DTEO phase modulator is coupled in three typical representatives of the interferometric systems, namely the interferometer, the holography system, and the differential microscope. Specifically, the temporal electronic speckle pattern interferometry (ESPI) system shows the dynamic feature which is brought by the DTEO phase modulator. Real-time measurements of the in-plane rotation is accomplished. In the phase-shifting in-line holography system, the phase modulator plays a role for the retrieval of the optical field at the hologram plane. Lensless imaging is realized by the back propagation of the retrieved optical field. In the Nomarski phase-shifting differential interference contrast (PS-DIC) microscope, a novel scheme of phase shit is proposed, which is termed as joint spatio-temporal phase modulation. The joint modulation is provided by the DTEO phase modulator and the differential prism. Quantitative visualization of phase objects is

achieved without dyeing. Bio-samples, i.e., the forewing of a honey bee, is rendered with sufficient contrast by the proposed quantitative Nomarski PS-DIC microscope.

For further developments regarding the DTEO phase modulator, two aspects are being into shape in the near future. One aspect goes to high frequency applications, and the other involves multi-carrier systems. By a new design of the driver circuit, the DTEO phase modulator is with the potential of running in the high frequencies, which is preferred in the investigation of transient process. Under high frequencies, the electro-optic coefficient requires a reconsideration, because there is no secondary effect from the electric field to the refractive index. Subsequently, the scheme of detection needs to be altered for high speed applications. A promising approach is based on the lock-in amplifier. The readout of the amplifier directly gives the information about the measuring phase without post-treatment algorithms. In the meantime, the lock-in amplifier has a strong ability of weak signal detection in a noisy environment.

In the other aspect, the optical interferometric systems with multiple temporal carriers are in conception. Two or more DTEO phase modulators are used in cascade. The multiple temporal carriers are generated by a precision control of the polarizations. Different carriers are mutually distinguished by their polarizations. For example, in the cascade of two DTEO phase modulators, one of the two phase-shifted components, which are generated by the first modulator, is sent to the second. The second modulator further shifts the received polarization into two components with different phases. At the exit of the cascade, the phases of the three components are shifted to different frequencies. The combination of either two components generates an individual temporal carrier. When the non-phase-shifted original wave is considered, even more carriers are generated in this scenario. Each temporal frequency carries an individual information, and thus multi-quantity simultaneous measurements are brought into conception.

In conclusion, a novel phase modulator is investigated in the present study, which is based on the dual transverse electro-optic effect. Physical fundamentals, mathematical derivations, and experimental demonstrations are described in detail. The compatibility of the proposed phase modulator is illustrated by three novel optical configurations, which are based on the typical representatives of interferometric systems. Two of the further developments are described but the future is not limited to that. For dedicated applications, it is readily to couple the proposed DTEO phase modulator into existing systems. It is expected that the DTEO phase modulator sees a development in both academic research and industrial applications.

Appendix A

A.1 List of Symbols

The symbols listed below are applied throughout the entire thesis. The locally used symbols are explained and defined in respective content where they first appear.

A	modulus of complex amplitude
A_{obj}	magnitude of the object wave
A_{ref}	magnitude of the reference wave
c	speed of light
exp	exponential function
E	electric field
f_{sp}	spatial frequency
f_t	temporal frequency
I	intensity
j	imaginary unit
k	wave number
L	length
n	refractive index
n_e	extraordinary refractive index
n_o	ordinary refractive index
V	Jones matrix for wave
t	time
T	Jones matrix for optical element
u	voltage
$\widetilde{U}$	complex amplitude, phasor
$\widetilde{U}_{obj}$	wavefront of object wave
$\widetilde{U}_{ref}$	wavefront of reference wave

α	angle
γ	visibility of interference
γ_{ij}	electro-optic coefficient
Γ	transmission function
Δ	phase shift within an acquisition cycle
θ	angle
λ	wavelength
$\boldsymbol{\rho}$	position vector
ϕ	phase
ϕ_{obj}	object phase
ϕ_{ref}	reference phase
ϕ_{stf}	phase shift
ϕ_{tar}	target phase
ω	angular frequency
ω_0	optical frequency of the wave
Ω	rotation angle
$\mathscr{F}$	Fourier transform
$\mathscr{M}$	operation of obtaining median
$\mathcal{R}$	rotation matrix

A.2 List of Abbreviations

1-D one-dimensional

2-D two-dimensional

3-D three-dimensional

AOM acousto-optic modulator

ASM angular spectrum method

BS beam splitter

CCD charge-coupled device

CW continuous-wave

DC direct current

DIC differential interference contrast

DOP degree of polarization

DSPI digital speckle pattern interferometry

DTEO dual transverse electro-optic

EM electromagnetic

EO electro-optic

ESPI electronic speckle pattern interferometry

HiBi highly birefringent

HWP half-wave plate

LN lithium niobate

N.A. numerical aperture

OPD optical path difference

OPL optical path length

PBS polarizing beam splitter

PS-DIC phase-shifting differential interference contrast

PZT piezo-electric transducer

QWP quarter-wave plate

RF radio frequency

A.3 List of Figures

Acknowledgment

Most of the research and study described in this thesis was done at the Institute for Measurement Systems and Sensor Technology (MST) of the Technical University of Munich (TUM). At the same time, the joint research that I conducted at the Department of Photonics Engineering of the Technical University of Denmark (DTU FOTONIK) contributes a substantive part (Chapter 6) to this thesis. Moreover, the entire study benefits quite a lot in all aspects from the years-long cooperation between MST and the Technical University of Madrid (UPM). These activities provide more than the essential and necessary scientific parts in pursuing the doctoral degree, but also brings me a precious and indelible memory in my life. With the greatest gratitude and pleasure, I wish to thank all the people who are involved in this work.

First and foremost I would like to express my deepest appreciation to my doctoral advisor Prof. Dr.-Ing. habil. Dr. h.c. Alexander W. Koch for his always-best support of my doctoral study. I sincerely appreciate his profound belief in my work, which gives me the freedom to carry out the study that I am concentrated in. I am also extremely grateful to Prof. Koch for the unparalleled knowledge, invaluable insight, and constructive advices that he gave me throughout the entire phase of his supervision.

I cannot begin to express my thanks to Prof. Dr. Félix Salazar-Bloise (UPM) for his most helpful discussions on all scientific parts of my doctoral study at all times. The completion of this thesis, as well as the related publications, would not have been possible without the in-person guidance from him. I would also like to extend my deepest gratitude to Prof. Steen Grüner Hanson (DTU) and Dr. Michael Linde Jakobsen (DTU). During my joint research in DTU, we had the aggressive but cookie-surrounded talks, which brought the joint modulation DIC microscopy technique into its current form. When I was in Denmark, Prof. Hanson introduced me to Prof. Mitsuo Takeda of Utsunomiya University. Special thanks go to Prof. Takeda for his brilliant idea of the reference fringe method, which inspired me to develop the phase retrieval algorithm for the microscope.

I am deeply indebted to Dr.-Ing. Martin Jakobi for the efforts that he has apparently

dedicated in making all my scientific outcomes more solid and professional. I must also thank Ms. Rita von Grafenstein for her most helpful and perfect arrangement of my work at MST. I gratefully acknowledge all the members of the speckle group, Dr.-Ing Min Lu, Dr.-Ing Laura Bilgeri, Franziska Pöller, and Jie Dong, for their contributions and cooperations in the daily laboratory section. I had also great pleasure of working with all the other colleagues at MST. The MST-Team has been a power source, which drives me further on at all times. In regards to the scientific proof reading of the first draft of this thesis, I particularly thank Franziska Pöller and Kun Wang for their constructive suggestions and the substantial amount of time and effort that they obviously dedicated to the review.

Last but not the least, I want to thank my parents and family for their constant love, support, and encouragement over years. At the end the biggest thank you goes to my beloved wife Shuai Gao for her curiosity and interest in my research. She gives me the maximum patience and best organization of the family. All of those are done in the middle of the adventure to her own doctoral degree. No words can sufficiently describe my gratitude.

Bibliography

[1] A. Stevenson. *Oxford dictionary of English*. Oxford University Press, 2010.

[2] J. K. Fotheringham. "On the smallest visible phase of the Moon". In: *Monthly Notices of the Royal Astronomical Society* 70 (1910), pp. 527–531. DOI: `10.1093/mnras/70.7.527`.

[3] H. Georgi. *The physics of waves*. Prentice Hall, 1993.

[4] H. Stanley. *Introduction to phase transitions and critical phenomena*. Oxford University Press, 1987.

[5] E. Purcell and D. Morin. *Electricity and magnetism*. Cambridge University Press, 2013.

[6] J. C. Maxwell. "VIII. A dynamical theory of the electromagnetic field". In: *Philosophical Transactions of the Royal Society of London* 155 (1865), pp. 459–512. DOI: `10.1098/rstl.1865.0008`.

[7] C. G. Fraser. *Half-hours with great scientists: the story of physics*. University of Toronto Press, 1948.

[8] I. Newton. *Opticks, or, a treatise of the reflections, refractions, inflections and colours of light*. Courier Corporation, 1979.

[9] J. Funke and P. Oranje. *Gas discharge lamps: principles, characterisics, applications*. Philips' Gloellampenfabricken, Technical and Scientific Literature Dept., 1951.

[10] A. Siegman. *Lasers*. University Science Books, 1986.

[11] B. Argence, B. Chanteau, O. Lopez, D. Nicolodi, M. Abgrall, C. Chardonnet, C. Daussy, B. Darquié, Y. Le Coq, and A. Amy-Klein. "Quantum cascade laser frequency stabilization at the sub-Hz level". In: *Nature Photonics* 9.7 (2015), pp. 456–460. DOI: `10.1038/nphoton.2015.93`.

[12] T. Young. "II. The Bakerian Lecture. On the theory of light and colours". In: *Philosophical transactions of the Royal Society of London* 92 (1802), pp. 12–48. DOI: 10.1098/rstl.1802.0004.

[13] T. Young. *A course of lectures on natural philosophy and the mechanical arts: in two volumes*. Johnson, 1807.

[14] M. Downs and K. Raine. "An unmodulated bi-directional fringe-counting interferometer system for measuring displacement". In: *Precision Engineering* 1.2 (1979), pp. 85 –88. DOI: 10.1016/0141-6359(79)90138-7.

[15] D. W. Robinson. "Automatic fringe analysis with a computer image-processing system". In: *Applied Optics* 22.14 (1983), pp. 2169–2176. DOI: 10.1364/AO.22.002169.

[16] J. H. Bruning, D. R. Herriott, J. E. Gallagher, D. P. Rosenfeld, A. D. White, and D. J. Brangaccio. "Digital wavefront measuring interferometer for testing optical surfaces and lenses". In: *Applied Optics* 13.11 (1974), pp. 2693–2703. DOI: 10.1364/AO.13.002693.

[17] Y. Y. Cheng and J. C. Wyant. "Phase shifter calibration in phase-shifting interferometry". In: *Applied Optics* 24.18 (1985), pp. 3049–3052. DOI: 10.1364/AO.24.003049.

[18] K. Kinnstaetter, A. W. Lohmann, J. Schwider, and N. Streibl. "Accuracy of phase shifting interferometry". In: *Applied Optics* 27.24 (1988), pp. 5082–5089. DOI: 10.1364/AO.27.005082.

[19] G. Lai and T. Yatagai. "Generalized phase-shifting interferometry". In: *Journal of the Optical Society of America A* 8.5 (1991), pp. 822–827. DOI: 10.1364/JOSAA.8.000822.

[20] M. Sargent, W. E. Lamb, and R. L. Fork. "Theory of a Zeeman laser. I". In: *Physical Review* 164 (2 1967), pp. 436–449. DOI: 10.1103/PhysRev.164.436.

[21] M. Sargent, W. E. Lamb, and R. L. Fork. "Theory of a Zeeman laser. II". In: *Physical Review* 164 (2 1967), pp. 450–465. DOI: 10.1103/PhysRev.164.450.

[22] R. A. Gonsalves. "Phase retrieval and diversity in adaptive optics". In: *Optical Engineering* 21.5 (1982), pp. 829–832. DOI: 10.1117/12.7972989.

[23] J. R. Fienup. "Phase retrieval algorithms: a comparison". In: *Applied Optics* 21.15 (1982), pp. 2758–2769. DOI: 10.1364/AO.21.002758.

[24] S. Silver. "Microwave aperture antennas and diffraction theory". In: *Journal of the Optical Society of America* 52.2 (1962), pp. 131–139. DOI: 10.1364/JOSA.52.000131.

[25]   J. E. Harvey. "Fourier treatment of near-field scalar diffraction theory". In: *American Journal of Physics* 47.11 (1979), pp. 974–980. DOI: 10.1119/1.11600.

[26]   D. Malacara. *Optical shop testing.* John Wiley & Sons, 2007.

[27]   J. R. Fienup. "Phase retrieval algorithms: a personal tour". In: *Applied Optics* 52.1 (2013), pp. 45–56. DOI: 10.1364/AO.52.000045.

[28]   L. M. Frantz, A. A. Sawchuk, and W. von der Ohe. "Optical phase measurement in real time". In: *Applied Optics* 18.19 (1979), pp. 3301–3306. DOI: 10.1364/AO.18.003301.

[29]   K. Creath. "Phase-measurement interferometry techniques". In: Progress in Optics. Elsevier, 1988, pp. 349 –393. DOI: 10.1016/S0079-6638(08)70178-1.

[30]   Y. Surrel. "Design of algorithms for phase measurements by the use of phase stepping". In: *Applied Optics* 35.1 (1996), pp. 51–60. DOI: 10.1364/AO.35.000051.

[31]   O. Sasaki, H. Okazaki, and M. Sakai. "Sinusoidal phase modulating interferometer using the integrating-bucket method". In: *Applied Optics* 26.6 (1987), pp. 1089–1093. DOI: 10.1364/AO.26.001089.

[32]   A. Dubois. "Phase-map measurements by interferometry with sinusoidal phase modulation and four integrating buckets". In: *Journal of the Optical Society of America A* 18.8 (2001), pp. 1972–1979. DOI: 10.1364/JOSAA.18.001972.

[33]   J. E. Greivenkamp. "Generalized data reduction for heterodyne interferometry". In: *Optical Engineering* 23.4 (1984), pp. 350–352. DOI: 10.1117/12.7973298.

[34]   C. J. Morgan. "Least-squares estimation in phase-measurement interferometry". In: *Optics Letters* 7.8 (1982), pp. 368–370. DOI: 10.1364/OL.7.000368.

[35]   J. C. Wyant. "Interferometric optical metrology: basic principles and new systems". In: *Laser Focus* 18.5 (1982), pp. 65–71.

[36]   J. Burke and H. Helmers. "Performance of spatial vs. temporal phase shifting in ESPI". In: *Interferometry'99: Techniques and Technologies.* Vol. 3744. International Society for Optics and Photonics. 1999, pp. 188–200. DOI: 10.1117/12.357712.

[37]   P. Carré. "Installation et utilisation du comparateur photoélectrique et interférentiel du Bureau International des Poids et Mesures". In: *Metrologia* 2 (Jan. 1966), pp. 13–23. DOI: 10.1088/0026-1394/2/1/005.

[38]   J. Schwider, R. Burow, K.-E. Elssner, J. Grzanna, R. Spolaczyk, and K. Merkel. "Digital wave-front measuring interferometry: some systematic error sources". In: *Applied Optics* 22.21 (1983), pp. 3421–3432. DOI: 10.1364/AO.22.003421.

[39] J. C. Wyant and K. N. Prettyjohns. *Optical profiler using improved phase shifting interferometry*. US Patent 4,639,139. 1987.

[40] P Hariharan, B. Oreb, and T. Eiju. "Digital phase-shifting interferometry: a simple error-compensating phase calculation algorithm". In: *Applied Optics* 26.13 (1987), pp. 2504–2506. DOI: `10.1364/AO.26.002504`.

[41] J. Angel and P Wizinowich. "A method for phase shifting interferometry in the presence of vibration". In: *European southern observatory conference and workshop proceedings*. Vol. 30. 1988, p. 561.

[42] P. L. Wizinowich. "System for phase shifting interferometry in the presence of vibration". In: *Surface Characterization and Testing II*. Vol. 1164. International Society for Optics and Photonics. 1989, pp. 25–36. DOI: `10.1117/12.962804`.

[43] P. L. Wizinowich. "Phase shifting interferometry in the presence of vibration: a new algorithm and system". In: *Applied Optics* 29.22 (1990), pp. 3271–3279. DOI: `10.1364/AO.29.003271`.

[44] M. Takeda, H. Ina, and S. Kobayashi. "Fourier-transform method of fringe-pattern analysis for computer-based topography and interferometry". In: *Journal of the Optical Society of America A* 72.1 (1982), pp. 156–160. DOI: `10.1364/JOSA.72.000156`.

[45] C. Joenathan, P. Haible, and H. J. Tiziani. "Speckle interferometry with temporal phase evaluation: influence of decorrelation, speckle size, and nonlinearity of the camera". In: *Applied Optics* 38.7 (1999), pp. 1169–1178. DOI: `10.1364/AO.38.001169`.

[46] N. A. Massie, R. D. Nelson, and S. Holly. "High-performance real-time heterodyne interferometry". In: *Applied Optics* 18.11 (1979), pp. 1797–1803. DOI: `10.1364/AO.18.001797`.

[47] L. Zhu, Y. Wang, N. Xu, S. Wu, M. Dong, and L. Yang. "Real-time monitoring of phase maps of digital shearography". In: *Optical Engineering* 52.10 (2013), p. 101902. DOI: `10.1117/1.OE.52.10.101902`.

[48] J. Zhong and J. Weng. "Phase retrieval of optical fringe patterns from the ridge of a wavelet transform". In: *Optics Letters* 30.19 (2005), pp. 2560–2562. DOI: `10.1364/OL.30.002560`.

[49] N. Nakajima. "Phase retrieval using the logarithmic Hilbert transform and the Fourier-series expansion". In: *Journal of the Optical Society of America A* 5.2 (1988), pp. 257–262. DOI: `10.1364/JOSAA.5.000257`.

[50]   D. E. Duffy. "Moiré gauging of in-plane displacement using double aperture imaging". In: *Applied Optics* 11.8 (1972), pp. 1778–1781. DOI: 10.1364/AO.11.001778.

[51]   T. Bothe, J. Burke, and H. Helmers. "Spatial phase shifting in electronic speckle pattern interferometry: minimization of phase reconstruction errors". In: *Applied Optics* 36.22 (1997), pp. 5310–5316. DOI: 10.1364/AO.36.005310.

[52]   B. Bhaduri, N. K. Mohan, M. P. Kothiyal, and R. Sirohi. "Use of spatial phase shifting technique in digital speckle pattern interferometry (DSPI) and digital shearography (DS)". In: *Optics Express* 14.24 (2006), pp. 11598–11607. DOI: 10.1364/OE.14.011598.

[53]   M. Born, E. Wolf, and A. Bhatia. *Principles of optics: electromagnetic theory of propagation, interference and diffraction of light.* Cambridge University Press, 2000.

[54]   K. Creath. "Phase-shifting speckle interferometry". In: *Applied Optics* 24 (1985), pp. 3053–3058. DOI: 10.1364/AO.24.003053.

[55]   C. Ai and J. C. Wyant. "Effect of piezoelectric transducer nonlinearity on phase shift interferometry". In: *Applied Optics* 26.6 (1987), pp. 1112–1116. DOI: 10.1364/AO.26.001112.

[56]   H. Jaffe and D. A. Berlincourt. "Piezoelectric transducer materials". In: *Proceedings of the IEEE* 53.10 (1965), pp. 1372–1386. DOI: 10.1109/PROC.1965.4253.

[57]   J. Valera and J. Jones. "Phase stepping in fiber-based speckle shearing interferometry". In: *Optics letters* 19.15 (1994), pp. 1161–1163. DOI: 10.1364/OL.19.001161.

[58]   V. Murukeshan, O. L. Seng, and A Asundi. "Polarization phase shifting shearography for optical metrological applications". In: *Optics & Laser Technology* 30.8 (1998), pp. 527–531. DOI: 10.1016/S0030-3992(99)00005-5.

[59]   F. Zhang and J. W. Lit. "Temperature and strain sensitivity measurements of high-birefringent polarization-maintaining fibers". In: *Applied Optics* 32.13 (1993), pp. 2213–2218. DOI: 10.1364/AO.32.002213.

[60]   J. Wyant and R. Shagam. "Use of electronic phase measurement techniques in optical testing". In: *Proc ICO-11, Madrid* (1978), pp. 659–662.

[61]   T. Suzuki and R. Hioki. "Translation of light frequency by a moving grating". In: *Journal of the Optical Society of America* 57.12 (1967), pp. 1551–1551. DOI: 10.1364/JOSA.57.001551.

[62]   W. H. Stevenson. "Optical frequency shifting by means of a rotating diffraction grating". In: *Applied Optics* 9.3 (1970), pp. 649–652. DOI: 10.1364/AO.9.000649.

[63] R. Kristal and R. W. Peterson. "Bragg cell heterodyne interferometry of fast plasma events". In: *Review of Scientific Instruments* 47.11 (1976), pp. 1357–1359. DOI: `10.1063/1.1134545`.

[64] T. Schmitz and J. Beckwith. "Acousto-optic displacement-measuring interferometer: a new heterodyne interferometer with Ångstrom-level periodic errorr". In: *Journal of Modern Optics* 49.13 (2002), pp. 2105–2114. DOI: `10.1080/095003402-10123938`.

[65] E. Li, J. Yao, D. Yu, J. Xi, and J. Chicharo. "Optical phase shifting with acousto-optic devices". In: *Optics Letters* 30.2 (2005), pp. 189–191. DOI: `10.1364/OL.30.000189`.

[66] E. A. Donley, T. P. Heavner, F. Levi, M. O. Tataw, and S. R. Jefferts. "Double-pass acousto-optic modulator system". In: *Review of Scientific Instruments* 76.6 (2005), p. 063112. DOI: `10.1063/1.1930095`.

[67] M. P. Kothiyal and C. Delisle. "Optical frequency shifter for heterodyne interferometry using counterrotating wave plates". In: *Optics Letters* 9.8 (1984), pp. 319–321. DOI: `10.1364/OL.9.000319`.

[68] H. D. Polster, J. Pastor, R. M. Scott, R. Crane, P. H. Langenbeck, R. Pilston, and G. Steinberg. "New developments in interferometry". In: *Applied Optics* 8.3 (1969), pp. 521–556. DOI: `10.1364/AO.8.000521`.

[69] R. N. Shagam and J. C. Wyant. "Optical frequency shifter for heterodyne interferometers using multiple rotating polarization retarders". In: *Applied Optics* 17.19 (1978), pp. 3034–3035. DOI: `10.1364/AO.17.003034`.

[70] H. Z. Hu. "Polarization heterodyne interferometry using a simple rotating analyzer. 1: Theory and error analysis". In: *Applied Optics* 22.13 (1983), pp. 2052–2056. DOI: `10.1364/AO.22.002052`.

[71] M. P. Kothiyal and C. Delisle. "Rotating analyzer heterodyne interferometer: error analysis". In: *Applied Optics* 24.15 (1985), pp. 2288–2290. DOI: `10.1364/AO.24.002288`.

[72] J. A. Dahlquist, D. G. Peterson, and W. Culshaw. "Zeeman laser interferometer". In: *Applied Physics Letters* 9.5 (1966), pp. 181–183. DOI: `10.1063/1.1754700`.

[73] P. Zeeman. "The effect of magnetisation on the nature of light emitted by a substance". In: *Nature* 55.1424 (1897), pp. 347–347. DOI: `10.1038/055347a0`.

[74] F. Schwabl. "The Zeeman effect and the stark effect". In: Quantum Mechanics. Springer Berlin Heidelberg, 2007, pp. 259–269. DOI: `10.1007/978-3-540-71933-5_14`.

[75] O. Y. Kwon, D. M. Shough, and R. A. Williams. "Stroboscopic phase-shifting interferometry". In: *Optics Letters* 12.11 (1987), pp. 855–857. DOI: `10.1364/OL.12.000855`.

[76] C. Bradley and A. Cracknell. *The mathematical theory of symmetry in solids: representation theory for point groups and space groups*. Oxford Classic Texts in the Physical Sciences. Oxford University Press, 2009.

[77] B. Saleh and M. Teich. *Fundamentals of photonics, 2 volume set*. Wiley Series in Pure and Applied Optics. Wiley, 2019.

[78] J. Nye. *Physical properties of crystals: their representation by tensors and matrices*. Oxford science publications. Clarendon Press, 1985.

[79] C. Davis. *Lasers and electro-optics: fundamentals and engineering*. Cambridge University Press, 1996.

[80] S. Haussühl. *Physical properties of crystals: an introduction*. Wiley, 2008.

[81] I. P. Kaminow and E. H. Turner. "Electrooptic light modulators". In: *Applied Optics* 5.10 (1966), pp. 1612–1628. DOI: `10.1364/AO.5.001612`.

[82] B. Guenther. *Modern Optics*. Oxford University Press, 2015.

[83] S. Wang, M. Lu, L. M. Bilgeri, M. Jakobi, F. S. Bloise, and A. W. Koch. "Temporal electronic speckle pattern interferometry for real-time in-plane rotation analysis". In: *Optics Express* 26.7 (2018), pp. 8744–8755. DOI: `10.1364/OE.26.008744`.

[84] J. Poirson, T. Lanternier, J.-C. Cotteverte, A. L. Floch, and F. Bretenaker. "Jones matrices of a quarter-wave plate for Gaussian beams". In: *Applied Optics* 34.30 (1995), pp. 6806–6818. DOI: `10.1364/AO.34.006806`.

[85] J. A. Leendertz. "Interferometric displacement measurement on scattering surfaces utilizing speckle effect". In: *Journal of Physics E: Scientific Instruments* 3.3 (1970), pp. 214–218. DOI: `10.1088/0022-3735/3/3/312`.

[86] P. Jacquot. "Speckle interferometry: a review of the principal methods in use for experimental mechanics applications". In: *Strain* 44.1 (2008), pp. 57–69. DOI: `10.1111/j.1475-1305.2008.00372.x`.

[87] K. A. Stetson. "A review of speckle photography and interferometry". In: *Optical Engineering* 14.5 (1975), pp. 482 –489 –8. DOI: `10.1117/12.7971814`.

[88] L. Yang, X. Xie, L. Zhu, S. Wu, and Y. Wang. "Review of electronic speckle pattern interferometry (ESPI) for three dimensional displacement measurement". In: *Chinese Journal of Mechanical Engineering* 27.1 (2014), pp. 1–13. DOI: `10.3901/CJME.2014.01.001`.

[89] V. D. Madjarova, H. Kadono, and S. Toyooka. "Dynamic electronic speckle pattern interferometry (DESPI) phase analyses with temporal Hilbert transform". In: *Optics Express* 11.6 (2003), pp. 617–623. DOI: 10.1364/OE.11.000617.

[90] M. Lu, S. Wang, L. Aulbach, and A. W. Koch. "Simultaneous displacement and slope measurement in electronic speckle pattern interferometry using adjustable aperture multiplexing". In: *Applied Optics* 55.22 (2016), pp. 5868–5875. DOI: 10.1364/AO.55.005868.

[91] F. M. Santoyo, M. C. Shellabear, and J. R. Tyrer. "Whole field in-plane vibration analysis using pulsed phase-stepped ESPI". In: *Applied Optics* 30.7 (1991), pp. 717–721. DOI: 10.1364/AO.30.000717.

[92] L.-S. Wang and S. Krishnaswamy. "Shape measurement using additive–subtractive phase shifting speckle interferometry". In: *Measurement Science and Technology* 7.12 (1996), pp. 1748–1754. DOI: 10.1088/0957-0233/7/12/009.

[93] P. de Groot. "Interferometric laser profilometer for rough surfaces". In: *Optics Letters* 16.6 (1991), pp. 357–359. DOI: 10.1364/OL.16.000357.

[94] N. Werth, F. Salazar-Bloise, and A. Koch. "Influence of roughness in the phase-shifting speckle method: An experimental study with applications". In: *Review of Scientific Instruments* 85.1 (2014), p. 015114. DOI: 10.1063/1.4861909.

[95] H. J. Gerritsen, W. J. Hannan, and E. G. Ramberg. "Elimination of speckle noise in holograms with redundancy". In: *Applied Optics* 7.11 (1968), pp. 2301–2311. DOI: 10.1364/AO.7.002301.

[96] J. Dainty. *Laser speckle and related phenomena*. Topics in Applied Physics. Springer Berlin Heidelberg, 2013.

[97] J. N. Butters and J. A. Leendertz. "A double exposure technique for speckle pattern interferometry". In: *Journal of Physics E: Scientific Instruments* 4.4 (1971), pp. 277–279. DOI: 10.1088/0022-3735/4/4/004.

[98] N. A. Ochoa, F. M. Santoyo, A. J. Moore, and C. P. López. "Contrast enhancement of electronic speckle pattern interferometry addition fringes". In: *Applied Optics* 36.13 (1997), pp. 2783–2787. DOI: 10.1364/AO.36.002783.

[99] R. Spooren. "Double-pulse subtraction TV holography". In: *Optical Engineering* 31.5 (1992), pp. 1000 –1007 –8. DOI: 10.1117/12.56149.

[100] D. R. Schmitt and R. W. Hunt. "Optimization of fringe pattern calculation with direct correlations in speckle interferometry". In: *Applied Optics* 36.34 (1997), pp. 8848–8857. DOI: 10.1364/AO.36.008848.

[101]   Q. Yu, S. Fu, X. Yang, X. Sun, and X. Liu. "Extraction of phase field from a single contoured correlation fringe pattern of ESPI". In: *Optics Express* 12.1 (2004), pp. 75–83. DOI: `10.1364/OPEX.12.000075`.

[102]   J. E. Sollid. "Holographic interferometry applied to measurements of small static displacements of diffusely reflecting surfaces". In: *Applied Optics* 8 (1969), p. 1587. DOI: `10.1364/AO.8.001587`.

[103]   S. Wu, M. Dong, Y. Fang, and L. Yang. "Universal optical setup for phase-shifting and spatial-carrier digital speckle pattern interferometry". In: *Journal of the European Optical Society-Rapid Publications* 12.1 (2016), p. 14. DOI: `10.1186/s41476-016-0016-6`.

[104]   M. Lu, S. Wang, L. Bilgeri, X. Song, M. Jakobi, and A. W. Koch. "Online 3D displacement measurement using speckle interferometer with a single illumination-detection path". In: *Sensors* 18.6 (2018). DOI: `10.3390/s18061923`.

[105]   P. Jacquot and J. Fournier. *Interferometry in speckle light: theory and applications.* Springer Berlin Heidelberg, 2012.

[106]   H. A. Aebischer and S. Waldner. "A simple and effective method for filtering speckle-interferometric phase fringe patterns". In: *Optics Communications* 162.4 (1999), pp. 205 –210. DOI: `https://doi.org/10.1016/S0030-4018(99)00116-9`.

[107]   S. Fu, X. Long, H. Lin, and Q. Yu. "Fringe-contoured-window sine/cosine filter for saw-tooth phase maps in ESPI". In: *Frontiers of Optoelectronics in China* 1.3 (2009), p. 345. DOI: `10.1007/s12200-008-0044-y`.

[108]   K. Takada, I. Yokohama, K. Chida, and J. Noda. "New measurement system for fault location in optical waveguide devices based on an interferometric technique". In: *Applied Optics* 26.9 (1987), pp. 1603–1606. DOI: `10.1364/AO.26.001603`.

[109]   A. A. Freschi and J. Frejlich. "Adjustable phase control in stabilized interferometry". In: *Optics Letters* 20.6 (1995), pp. 635–637. DOI: `10.1364/OL.20.000635`.

[110]   C. Wu, J. Lawall, and R. D. Deslattes. "Heterodyne interferometer with subatomic periodic nonlinearity". In: *Applied Optics* 38.19 (1999), pp. 4089–4094. DOI: `10.1364/AO.38.004089`.

[111]   P. B. Dixon, D. J. Starling, A. N. Jordan, and J. C. Howell. "Ultrasensitive beam deflection measurement via interferometric weak value amplification". In: *Physical Review Letters* 102 (17 2009), p. 173601. DOI: `10.1103/PhysRevLett.102.173601`.

[112]   D. Gabor. "A new microscopic principle". In: *Nature* 161.4098 (1948), pp. 777 – 778. DOI: `10.1038/161777a0`.

[113] E. N. Leith and J. Upatnieks. "Reconstructed Wavefronts and Communication Theory". In: *Journal of the Optical Society of America* 52.10 (1962), pp. 1123–1130. DOI: 10.1364/JOSA.52.001123.

[114] E. N. Leith and J. Upatnieks. "Wavefront reconstruction with continuous–tone objects". In: *Journal of the Optical Society of America* 53.12 (1963), pp. 1377–1381. DOI: 10.1364/JOSA.53.001377.

[115] E. N. Leith and J. Upatnieks. "Wavefront reconstruction with diffused illumination and three-dimensional objects". In: *Journal of the Optical Society of America* 54.11 (1964), pp. 1295–1301. DOI: 10.1364/JOSA.54.001295.

[116] J. W. Goodman and R. W. Lawrence. "Digital image formation from electronically detected holograms". In: *Applied Physics Letters* 11.3 (1967), pp. 77–79. DOI: 10.1063/1.1755043.

[117] I. Yamaguchi and T. Zhang. "Phase-shifting digital holography". In: *Optics Letters* 22.16 (1997), pp. 1268–1270. DOI: 10.1364/OL.22.001268.

[118] E. Cuche, P. Marquet, and C. Depeursinge. "Spatial filtering for zero-order and twin-image elimination in digital off-axis holography". In: *Applied Optics* 39.23 (2000), pp. 4070–4075. DOI: 10.1364/AO.39.004070.

[119] J. Goodman. *Introduction to Fourier optics*. McGraw-Hill physical and quantum electronics series. W. H. Freeman, 2005.

[120] J. E. Greivenkamp. *Field guide to geometrical optics*. Vol. 1. SPIE press Bellingham, WA, 2004.

[121] U. Schnars, C. Falldorf, J. Watson, and W. Jüptner. "Digital holography". In: *Digital Holography and Wavefront Sensing: Principles, Techniques and Applications*. Berlin, Heidelberg: Springer Berlin Heidelberg, 2015, pp. 39–68. DOI: 10.1007/978-3-662-44693-5_3.

[122] J. A. Ratcliffe. "Some aspects of diffraction theory and their application to the ionosphere". In: *Reports on Progress in Physics* 19.1 (1956), pp. 188–267. DOI: 10.1088/0034-4885/19/1/306.

[123] U. Schnars and W. P. O. J. ptner. "Digital recording and numerical reconstruction of holograms". In: *Measurement Science and Technology* 13.9 (2002), R85–R101. DOI: 10.1088/0957-0233/13/9/201.

[124] N. Verrier and M. Atlan. "Off-axis digital hologram reconstruction: some practical considerations". In: *Applied Optics* 50.34 (2011), H136–H146. DOI: 10.1364/AO.50.00H136.

[125] T. Kreis. *Handbook of holographic interferometry: optical and digital methods*. 1st ed. John Wiley & Sons, Ltd, 2004. DOI: `10.1002/3527604154`.

[126] F. Zernike. "Phase contrast, a new method for the microscopic observation of transparent objects". In: *Physica* 9.7 (1942), pp. 686 –698. DOI: `10.1016/S0031-8914(42)80035-X`.

[127] F. Zernike. "Phase contrast, a new method for the microscopic observation of transparent objects part II". In: *Physica* 9.10 (1942), pp. 974 –986. DOI: `10.1016/S0031-8914(42)80079-8`.

[128] D. J. Stephens and V. J. Allan. "Light microscopy techniques for live cell imaging". In: *Science* 300.5616 (2003), pp. 82–86. DOI: `10.1126/science.1082160`.

[129] R. Allen and G. David. "The Zeiss-Nomarski differential interference equipment for transmitted-light microscopy". In: *Zeitschrift für wissenschaftliche Mikroskopie und mikroskopische Technik* 69.4 (1969), pp. 193–221.

[130] W. Lang. *Nomarski differential interference-contrast microscopy*. Carl Zeiss, 1982.

[131] C. J. Cogswell, N. I. Smith, K. G. Larkin, and P. Hariharan. "Quantitative DIC microscopy using a geometric phase shifter". In: *Three-Dimensional Microscopy: Image Acquisition and Processing IV*. Vol. 2984. International Society for Optics and Photonics. 1997, pp. 72–82. DOI: `10.1117/12.271252`.

[132] C. Preza, D. L. Snyder, and J.-A. Conchello. "Theoretical development and experimental evaluation of imaging models for differential-interference-contrast microscopy". In: *Journal of the Optical Society of America A* 16.9 (1999), pp. 2185–2199. DOI: `10.1364/JOSAA.16.002185`.

[133] D. Fu, S. Oh, W. Choi, T. Yamauchi, A. Dorn, Z. Yaqoob, R. R. Dasari, and M. S. Feld. "Quantitative DIC microscopy using an off-axis self-interference approach". In: *Optics Letters* 35.14 (2010), pp. 2370–2372. DOI: `10.1364/OL.35.002370`.

[134] P. Bon, G. Maucort, B. Wattellier, and S. Monneret. "Quadriwave lateral shearing interferometry for quantitative phase microscopy of living cells". In: *Optics Express* 17.15 (2009), pp. 13080–13094. DOI: `10.1364/OE.17.013080`.

[135] M. Takeda and M. Kitoh. "Spatiotemporal frequency multiplex heterodyne interferometry". In: *Journal of the Optical Society of America A* 9.9 (1992), pp. 1607–1614. DOI: `10.1364/JOSAA.9.001607`.

[136] K. Qian, Y. Fu, Q. Liu, H. S. Seah, and A. Asundi. "Generalized three-dimensional windowed Fourier transform for fringe analysis". In: *Optics Letters* 31.14 (2006), pp. 2121–2123. DOI: `10.1364/OL.31.002121`.

[137]   C Trillo, A. Doval, and J. López-Vázquez. "Three-dimensional Fourier transform
        evaluation of sequences of spatially and temporally modulated speckle interfero-
        grams". In: *Optics Express* 18.14 (2010), pp. 15017–15027. DOI: 10.1364/OE.18.
        015017.

[138]   S. V. King, A. R. Libertun, R. Piestun, C. J. Cogswell, and C. Preza. "Quanti-
        tative phase microscopy through differential interference imaging". In: *Journal of
        Biomedical Optics* 13.2 (2008), pp. 1 –10 –10. DOI: 10.1117/1.2907328.

[139]   C. J. Cogswell, N. I. Smith, K. G. Larkin, and P. Hariharan. "Quantitative DIC
        microscopy using a geometric phase shifter". In: *Three-Dimensional Microscopy:
        Image Acquisition and Processing IV*. Vol. 2984. International Society for Optics
        and Photonics. 1997, pp. 72–82. DOI: 10.1117/12.271252.

[140]   M. Pluta. "Nomarski's DIC microscopy: a review". In: *Phase Contrast and Dif-
        ferential Interference Contrast Imaging Techniques and Applications*. Vol. 1846.
        International Society for Optics and Photonics. 1994, pp. 10–26. DOI: 10.1117/
        12.171873.

[141]   C. C. Montarou and T. K. Gaylord. "Analysis and design of modified Wollaston
        prisms". In: *Applied Optics* 38.31 (1999), pp. 6604–6616. DOI: 10.1364/AO.38.
        006604.

[142]   S. Wang, J. Dong, F. Pöller, X. Dong, M. Lu, L. M. Bilgeri, M. Jakobi, F. Salazar-
        Bloise, and A. W. Koch. "Dual-directional shearography based on a modified
        common-path configuration using spatial phase shift". In: *Applied Optics* 58.3
        (2019), pp. 593–603. DOI: 10.1364/AO.58.000593.

Patents and Publications

[1] **Shengjia Wang**, J. Dong, F. Pöller, X. Dong, M. Lu, L. M. Bilgeri, M. Jakobi, F. Salazar-Bloise, and A. W. Koch. "Dual-directional shearography based on a modified common-path configuration using spatial phase shift". In: *Applied Optics* 58.3 (2019). **Selected as Editors' Pick**, pp. 593–603. DOI: `10.1364/AO.58.000593`.

[2] **Shengjia Wang**, M. Lu, L. M. Bilgeri, M. Jakobi, F. Salazar-Bloise, and A. W. Koch. "Temporal electronic speckle pattern interferometry for real-time in-plane rotation analysis". In: *Optics Express* 26.7 (2018), pp. 8744–8755. DOI: `10.1364/OE.26.008744`.

[3] **Shengjia Wang**, Z. Gao, G. Li, Z. Feng, and Q. Feng. "Continual mechanical vibration trajectory tracking based on electro-optical heterodyne interferometry". In: *Optics Express* 22.7 (2014), pp. 7799–7810. DOI: `10.1364/OE.22.007799`.

[4] **Shengjia Wang**, Z. Gao, G. Li, and Z. Feng. "Adaptive pulse oximeter with dual-wavelength based on wavelet transforms". In: *Optics Express* 21.20 (2013), pp. 23058–23067. DOI: `10.1364/OE.21.023058`.

[5] **Shengjia Wang**, Z. Gao, Z. Feng, X. Zhang, D. Yang, and H. Yuan. "Heterodyne imaging speckle interferometer". In: *Optics Communications* 338 (2015). **Published as Fast Track Communications**, pp. 253 –256. DOI: `10.1016/j.optcom.2014.09.078`.

[6] **Shengjia Wang**. "A method and device for obtaining a phase shifted shearogram for shearography". Pat. EP2018057750 & WO2018178064 (Europe & PCT). Oct. 2018.

[7] J. Dong, **Shengjia Wang**, A. Yetisen, X. Dong, F. Pöller, N. Ong, M. Jakobi, Z. Liu, F. Salazar-Bloise, and A. W. Koch. "Shear-unlimited common-path speckle interferometer". In: *Optics Letters* (2020). Accepted on 28 January 2020. DOI: `10.1364/OL.382893`.

[8] J. Dong, **Shengjia Wang**, M. Lu, M. Jakobi, Z. Liu, X. Dong, F. Pöller, L. M. Bilgeri, F. Salazar-Bloise, A. K. Yetisen, and A. W. Koch. "Real-time dual-sensitive shearography for simultaneous in-plane and out-of-plane strain measurements". In: *Optics Express* 27.3 (2019), pp. 3276–3283. DOI: 10.1364/OE.27.003276.

[9] M. Lu, **Shengjia Wang**, L. Bilgeri, X. Song, M. Jakobi, and A. W. Koch. "Online 3D displacement measurement using speckle interferometer with a single illumination-detection path". In: *Sensors* 18.6 (2018). DOI: 10.3390/s18061923.

[10] M. Lu, **Shengjia Wang**, L. Aulbach, M. Jakobi, and A. W. Koch. "Non-phase unwrapping interferometric approach for a real-time in-plane rotation measurement". In: *Optics Letters* 42.10 (2017), pp. 1986–1989. DOI: 10.1364/OL.42.001986.

[11] M. Lu, **Shengjia Wang**, L. Aulbach, and A. W. Koch. "Simultaneous displacement and slope measurement in electronic speckle pattern interferometry using adjustable aperture multiplexing". In: *Applied Optics* 55.22 (2016), pp. 5868–5875. DOI: 10.1364/AO.55.005868.

[12] X. Dong, M. Jakobi, **Shengjia Wang**, M. H. Köhler, X. Zhang, and A. W. Koch. "A review of hyperspectral imaging for nanoscale materials research". In: *Applied Spectroscopy Reviews* (2018), pp. 1–21. DOI: 10.1080/05704928.2018.1463235.

[13] A. Koch, M. Lu, **Shengjia Wang**, L. Aulbach, and M. Jakobi. "Optical rotation sensor based on speckle interferometry". In: *Advanced Photonics 2017 (IPR, NOMA, Sensors, Networks, SPPCom, PS)*. Optical Society of America, 2017, SeM3E.4. DOI: 10.1364/SENSORS.2017.SeM3E.4.

[14] Z. Gao, G. Li, **Shengjia Wang**, Z. Feng, and Q. Feng. "Novel laser interference length measuring method". Pat. CN103234461A (China). Aug. 2013.

[15] F. Pöller, L. M. Bilgeri, M. Jakobi, **Shengjia Wang**, J. Dong, A. W. Koch, and F. Salazar-Bloise. "Rauheitsauswertung mit hoher lateraler Auflösung mittels räumlicher Lichtmodulatoren/Roughness evaluation with high lateral resolution by spatial light modulators". In: *tm-Technisches Messen* 86.s1 (2019), pp. 22–26. DOI: 10.1515/teme-2019-0042.

[16] F. Pöller, F. Salazar-Bloise, M. Jakobi, **Shengjia Wang**, J. Dong, and A. W. Koch. "Non-contact roughness measurement in sub-micron range by considering depolarization effects". In: *Sensors* 19.10 (2019). DOI: 10.3390/s19102215.

[17] L. M. Bilgeri, F. Salazar-Bloise, M. Lu, **Shengjia Wang**, M. Jakobi, and A. W. Koch. "Intensity distortions due to phase-only spatial light modulation: characterization for applications in electronic speckle-pattern interferometry". In: *Review of Scientific Instruments* 89.8 (2018), p. 083701. DOI: 10.1063/1.5029914.

[18] Z. Feng, Z. Gao, X. Zhang, **Shengjia Wang**, D. Yang, H. Yuan, and J. Qin. "A polarized digital shearing speckle pattern interferometry system based on temporal wavelet transformation". In: *Review of Scientific Instruments* 86.9 (2015), p. 093102. DOI: 10.1063/1.4929533.

[19] L. Aulbach, F. Pöller, M. Lu, **Shengjia Wang**, and A. W. Koch. "Optical mapping of surface roughness by implementation of a spatial light modulator". In: *Applied Optical Metrology II*. Vol. 10373. International Society for Optics and Photonics. 2017. DOI: 10.1117/12.2270548.

[20] L. Aulbach, M. Oberhans, M. Lu, **Shengjia Wang**, and A. W. Koch. "Modellierung von Referenzwellen zur lokalen Desensibilisierung in der Speckle-Interferometrie mittels Qualitätskriterien des Phasenbildes". In: *Proc. 118. DGaO-Jahrestagung*. Deutsche Gesellschaft für angewandte Optik, 2017, P29.

[21] L. Aulbach, F. Salazar-Bloise, M. Lu, **Shengjia Wang**, and A. W. Koch. "Structural influence of a spatial light modulator on generated wavefronts for speckle-based shape measurement". In: *Automated Visual Inspection and Machine Vision II*. Vol. 10334. International Society for Optics and Photonics. 2017. DOI: 10.1117/12.2269453.

[22] Z. Feng, Z. Gao, X. Zhang, and **Shengjia Wang**. "Research on key factors in the digital shearing speckle pattern interferometry". In: *2015 International Conference on Optical Instruments and Technology: Advanced Lasers and Applications*. Vol. 9621. International Society for Optics and Photonics. 2015. DOI: 10.1117/12.2193121.

[23] Z. Gao, J. Qin, Q. Feng, **Shengjia Wang**, X. Wang, S. Yang, and C. Gao. "Method for full-field measurement using dynamic laser Doppler imaging". Pat. CN2016102567 & WO2018072143 (China & PCT). Apr. 2018.

[24] X. Dong, J. Dong, A. K. Yetisen, M. H. Köhler, **Shengjia Wang**, M. Jakobi, and A. W. Koch. "Characterization and layer thickness mapping of two-dimensional MoS$_2$ flakes via hyperspectral line-scanning microscopy". In: *Applied Physics Express* 12.10 (2019), p. 102004. DOI: 10.7567/1882-0786/ab3e51.

[25] X. Dong, A. K. Yetisen, M. H. Köhler, J. Dong, **Shengjia Wang**, M. Jakobi, X. Zhang, and A. W. Koch. "Microscale spectroscopic mapping of 2D optical materials". In: *Advanced Optical Materials* 0.0 (2019), p. 1900324. DOI: 10.1002/adom.201900324.

[26] C. Zhong, Z. Gao, X. Wang, C. Gao, S. Yang, X. Sun, X. Wen, Z. Feng, and
      Shengjia Wang. "The machine learning method of phase extraction in interfer-
      ometry". In: *Optics and Lasers in Engineering* 110 (2018), pp. 384 –391. DOI:
      `10.1016/j.optlaseng.2018.06.021`.

[27] X. Wang, Z. Gao, S. Yang, C. Gao, X. Sun, X. Wen, Z. Feng, **Shengjia Wang**, and
      Y. Fan. "Application of digital shearing speckle pattern interferometry for thermal
      stress". In: *Measurement* 125 (2018), pp. 11 –18. DOI: `10.1016/j.measurement.`
      `2018.04.073`.

[28] X. Zhang, Z. Gao, J. Qin, G. Li, Z. Feng, and **Shengjia Wang**. "Synchronous
      two-wavelength temporal interferometry". In: *8th International Symposium on Ad-
      vanced Optical Manufacturing and Testing Technologies: Optical Test, Measure-
      ment Technology, and Equipment*. Vol. 9684. International Society for Optics and
      Photonics. 2016. DOI: `10.1117/12.2239472`.

Supervised Student Theses

[1] Q. Wang. "Spatial phase-shifting in common-path shearography by using virtual apertures". Bachelor Thesis. Technical University of Munich, Apr. 2018.

[2] Q. Cao. "Phase retrieval based on temporal phase shifting techniques - devices and algorithms evaluation". Advanced Seminar. Technical University of Munich, Mar. 2016.